AN UNCOUPLED MULTIPHASE APPROACH TOWARDS MODELING ICE CRYSTALS IN JET ENGINES

MOHAMED SHEZAD NILAMDEEN

Computational Fluid Dynamics Laboratory, Department of Mechanical Engineering,

McGill University, Montreal, Quebec

A thesis submitted to McGill University in partial fulfillment of the requirements of the degree of Master of Engineering

Acknowledgements

I would like to extend my deepest gratitude to Dr. W.G. Habashi for taking me under his wing, and for providing me with tremendous support, guidance, confidence as well as funding during this period of time. The joy and enthusiasm he has for his research is contagious and has been motivational for me, even during tough times.

I would like to extend my sincere thanks to all my colleagues at the CFD Lab and Newmerical Technologies Inc. The group has been a source of friendships, good advice, and has helped promote my critical thought process. In this work, nothing would have been possible without the collaboration and understanding of the Vice President, Martin Aubé, Product Development Director, Guido Baruzzi, and all of the other members of the NTI group that helped me overcome the steep learning curve.

My time at McGill would not have been so enjoyable without the many friends that have become part of my life and kept me in good spirits. The paper may crumble; the ink may fade, but never do the memories of the friends I have made.

A source of inspiration in aircraft design and engineering comes from my uncle Zafar. Thank you for being so patient with me and making me a team player when it came to building and painting those model aircraft, even though you did most of the work.

To my reliable aunty Ghazala, who puts up with all my demands when I'm in Sri Lanka and manages to deliver each and every time.

I would like to thank my family for all their encouragement, unconditional love, and understanding. To my aunt Naan, and my uncle Fahamy, who funded my first university computer, which helped me immensely through my undergraduate years. Naan lives on in the loving memory of her family and friends. To my dad's brothers and sisters for showing me that you don't need to have a lot of money to have a good time and enjoy what life has to offer. To my grandfather for those interesting conversations on the front veranda, and to my grandmother for her tireless efforts in the kitchen to make every meal special when I'm around. To my sister Shumaila, with whom I shared childhood memories and grown-up dreams, and my brother Rashad, who never fails to surprise me with his talents, and helps me see the lighter, brighter side of an otherwise serious situation. And finally, but most importantly, to my mum who raised me and always allowed me to pursue my interests, and my dad who encouraged me to always "*do my best and leave the rest*".

Abstract

A recent series of high altitude turbofan engine malfunctions, characterized by flameout and sudden power losses have been reported in recent years. The source of these incidents has been hypothesized to be due to the presence of ice crystals at high altitudes. Ice crystals have been shown to have ballistic trajectories and consequently enter the core engine flow, without getting centrifuged out towards the engine bypass as droplets do. The crystals may melt as they move downstream to higher temperatures in successive stages, or hit a heated surface. The wetted surface may then act as an interface for further crystal impingement, which locally reduces the temperature and could lead to an ice accretion on the components. Ice can accrete to dangerously high levels, causing compressor surge due to blockage of the primary flowpath, vibrational instabilities due to load imbalances of ice on rotating components, mechanical damage of components downstream due to large shed ice fragments, or performance losses if ice enters the combustor, causing a decreased burner efficiency and an eventual flame-out.

In order to provide a numerical tool to analyze such situations, FENSAP-ICE has been extended to model mixed-phase flows that combine air, water and ice crystals, and the related ice accretion. DROP3D has been generalized to calculate particle impingement, concentration, and field velocities in an uncoupled approach that neglects any phase change by assuming both ice crystals and supercooled droplets are in thermodynamic equilibrium. ICE3D then accounts for the contribution of ice crystals that stick and melt on an existing water-film and promote ice accretion.

The extended ice crystal impingement and ice accretion model has been validated against test data from Cox and Co. and National Research Council icing tests conducted on a NACA0012 airfoil and unheated non-rotating cylinder respectively. The tests show a consistent agreement with respect to experimental profiles in terms of capturing the overall shape, although some of the ice profiles were conservative since they over-predicted the amount of ice accreted. The experimental observations suggest that ice crystals cause splashing of an existing film, and erosion effects when they impact an iced surface, and cause an overall loss in the amount of ice, as well as a general streamlining of the ice profile. This has not been taken into account in the present numerical model. The overall predictions in comparison with other numerical models, however, have improved and are a promising step towards simulating ice-shedding characteristics in a turbomachine.

Sommaire

De nombreux incidents liés à des problèmes de fonctionnement de moteurs d'avions ont été observés ces dernières années, tous caractérisés par l'extinction du moteur ou une perte soudaine de sa puissance. Ces incidents à haute altitude pourraient être causés par des cristaux de glace qui, de par leur trajectoire balistique, entrent directement dans le coeur du moteur sans être déviés par la force centrifuge vers le pontage, comme pour les gouttelettes d'eau. Les cristaux peuvent alors fondre lorsqu'ils rencontrent des températures plus élevées dans le moteur ou lorsqu'ils heurtent une surface chaude. Une telle surface humide pourrait devenir un noyau de cristallisation en réduisant localement la température, favorisant ainsi la formation de glace sur les composants internes du moteur. Cette accumulation présente un danger lorsqu'elle réduit l'espace libre pour l'écoulement d'air, engendrant un phénomène de pompage du compresseur. Elle peut aussi causer des instabilités vibrationnelles lorsqu'elle n'est pas uniforme sur les composantes rotatives, causant ainsi un débalancement de charge. De l'impact des tessons de glace qui se décollent de la surface peut endommager l'équipement mécanique en aval, et causer des pertes de performance liées à la présence de glace dans la chambre de combustion, engendrant une chute de l'efficacité du brûleur et éventuellement l'extinction de la flamme.

Afin de fournir un outil numérique pour l'analyse de telles situations, des modifications ont été apportées à FENSAP-ICE pour lui permettre de simuler l'écoulement de phases hétérogènes (air, eau, cristaux de glace) et l'accumulation de glace sur la surface. DROP3D a été généralisé afin de calculer la concentration et les champs de vitesses d'une particule de façon non couplée, en supposant que les cristaux de glace et les gouttelettes d'eau surgelées coexistent en équilibre thermodynamique. ICE3D à été modifié pour tenir compte des cristaux de glace qui se collent sur une couche d'eau existante et qui fondent, favorisant le phénomène d'accrétion de glace.

Les modifications au modèle de simulation d'accrétion de glace pour les cristaux de glace ont été validées à l'aide des données de Cox & Co., ainsi que des essais du Conseil National de Recherche du Canada, portant sur un profil NACA0012 et un cylindre sans rotation ni chauffage. Les résultats de ces essais démontrent que le modèle de simulation est généralement capable de prédire les formes de glace, sauf pour quelques profils qui ont donné des résultats conservateurs avec une plus importante accumulation de glace. Cet excès de glace peut être expliqué par des observations expérimentales qui suggèrent que l'impact des cristaux de glace incidents avec la surface cause des éclaboussures dans la couche d'eau existante, et que l'écoulement autour de la glace provoque l'érosion de celle-ci, produisant ainsi une surface plus lisse et plus réfractaire à l'accumulation. Ces effets n'ont pas été considérés dans ce modèle de simulation numérique. En général, les prédictions s'améliorent lorsqu'on les compare avec d'autres modèles et représentent un résultat prometteur pour la simulation des caractéristiques de délestage de glace dans un turboréacteur.

Table of Contents

List of Figures

List of Tables

List of Symbols

Latin Alphabet

$\vec{a}_p$ Particle acceleration vector

a Ice crystal semi major axis length $[m]$

a_i Particle acceleration component in 'i' coordinate direction $[m/s^2]$

b Ice crystal semi-minor axis length $[m]$

c_h Convective heat transfer coefficient

$c_{p,air}$ Specific heat capacity of air $[\mathrm{J}/(kgK)]$

$c_{p,ice}$ Specific heat capacity of ice $[\mathrm{J}/(kgK)]$

$c_{p,w}$ Specific heat capacity of water $[\mathrm{J}/(kgK)]$

d_{eq} Volumetric equivalent diameter of an ice crystal to a sphere $[m]$

d_p Particle diameter $[m]$

dV Control volume for water-film

dS Control Surface surrounding dV

$\vec{e}_n$ Unit vector in normal direction to a wall surface

$\vec{e}_t$ Unit vector in tangent direction to a wall surface

$\vec{e}_z$ Unit vector in spanwise direction of a wall surface

e_{dry} Normal coefficient of restitution for an dry surface

e_{wet} Normal coefficient of restitution for a wetted surface

g_i Gravitational component in 'i' coordinate direction

h_f Water film height $[m]$

m_p Particle mass $[kg]$

$\dot{m}_{evap}$ Time rate of evaporation/sublimation from the water-film surface $[kg/s]$

m''_{evap} Mass flux of evaporation $[kg/(m^2 s)]$

$\dot{m}_{ice}$ Time rate of ice accreted from the water-film surface $[kg/s]$

m''_{ice} Mass flux of ice accumulation $[kg/(m^2 s)]$

$\dot{m}_{ice,ic}$ Time rate of addition of ice crystals that stick but do not melt $[kg/s]$

$\dot{m}_F$ Time rate of change of flux transferred across dS $[kg/s]$

$\dot{m}_V$ Time rate of change of water inside dV $[kg/s]$

$\dot{m}_{\beta_1}$ Time rate of addition of droplets to the film by impingement $[kg/s]$

$\dot{m}_{\beta_2}$ Time rate of addition of ice to the film by sticking and melting $[kg/s]$

$\vec{n}$ Normal vector to aerodynamic surface (Chapt. 2); Normal to dS (Chapt. 3)

$q''_{a,conv}$ Heat flux calculated in FENSAP airflow solution $[kg/m^2 s]$

q''_{loss} Kinetic energy flux lost by ice crystals that bounce on a wetted surface $[kg/s^3]$

$\vec{v}_a$ Air velocity vector $[m/s]$

$\vec{v}_f$ Film velocity vector $[m/s]$

$\vec{v}_p$ Particle velocity vector $[m/s]$

$\vec{v}_{rel}$ Relative velocity between air and particles $[\vec{v}_a - \vec{v}_p]$

v_i Particle velocity component in 'i' coordinate direction

$v_{a,i}$ Air velocity component in 'i' coordinate direction

v_c Critical normal impact velocity component that defines bounds for crystal bounce

v_n Normal impact velocity component of an ice crystal

$v_{n,impact}$ Post-impact rebound normal velocity component of an ice crystal

x_o Initial separation of the particle with the surface $\left(2h_f / 3\right)$

A_{ij} Jacobian matrix evaluated at arithmetic average of values at nodes i and j

C_d Particle drag coefficient

C_f Skin friction coefficient

E Ice crystal aspect ratio (b/a)

Fr Froude number $\left(U_\infty / \sqrt{Lg}\right)$

$H_{r,\infty}$ Relative humidity

ICC_∞ Freestream ice crystal content $[g/m^3]$

K_p Particle inertia parameter

L Characteristic length scale of flow $[m]$

L_{evap} Latent heat of vaporization for water $[J/kg]$

L_{fus} Latent heat of fusion for ice $[J/kg]$

L_{sub} Latent heat of sublimation for ice $[J/kg]$

LWC_∞ Freestream liquid water content $[g/m^3]$

$P_{v,p}$ Saturation vapor pressure at the surface $[Pa]$

$P_{v,\infty}$ Saturation vapor pressure of water in ambient air $[Pa]$

P_{wall} Absolute pressure above the control volume outside the boundary layer $[Pa]$

$\dot{Q}_{conv}$ Rate of energy lost by convective heat transfer $[kg/s]$

$\dot{Q}_{evap}$ Rate of energy transferred by sublimation/evaporation of the water-film $[kg/s]$

$\dot{Q}_{fus}$ Rate of energy transferred through a change of state from water-film to ice $[kg/s]$

$\dot{Q}_{ice}$ Rate of energy removed by ice $[kg/s]$

$\dot{Q}_{loss}$ Rate of kinetic energy lost to the film by bouncing ice crystals $[kg/s]$

$\dot{Q}_{rad}$ Rate of energy lost by radiative heat transfer $[kg/s]$

$\dot{Q}_F$ Rate of energy transferred through dS $[kg/s]$

$\dot{Q}_V$ Time rate of change of energy inside dV $[kg/s]$

$\dot{Q}_{\beta_1}$ Rate of energy transferred by impinging droplets $[kg/s]$

$\dot{Q}_{\beta_2}$ Rate of energy transferred by ice crystals that stick and melt $[kg/s]$

Re_p Particle Reynolds number $\left(\dfrac{\rho_a \|\vec{v}_{rel}\| d_p}{\mu_a}\right)$

S_{ref} Area of a particle projected normal to $\vec{v}_{rel}$

St_c Critical Stokes number for a spherical particle that bounces on a wetted surface

St_p Particle Stokes number $\left(\dfrac{\tau_v}{\tau_f}\right)$

T Surface temperature (K)
$T_{adiabatic}$ Adiabatic recovery temperature
$T_{freeze,ref}$ Reference freezing temperature of water to ice (273.15K)
T_{∞} Free-stream air termperature (K)
$T_{\infty,p}$ Particle temperature at free-stream $(°C)$
$\tilde{T}$ Temperature of ice film interface $(°C)$
$\tilde{T}_{init}$ Initial surface temperature calculated from FENSAP airflow solution $(°C)$
U_{∞} Free-stream velocity magnitude $[m/s]$
V_p Volume of a single particle $[m^3]$
W Weight function
Z Mass loading ratio $\left(\bar{\rho}_p / \bar{\rho}_a \right)$

Greek Alphabet

α_m Fraction of sticking ice crystals that melt
α_p Particle volume fraction
α_{st} Fraction of impinging ice crystals that stick
β_d Collection efficiency for droplets
β_{ic} Collection efficiency for ice crystals
γ_p Poisson's ratio for a given particle type
γ_{surf} Poisson's ratio for the material of the surface impacted by particles
ε Solid emissivity
η Elasticity parameter
λ_{surf} Elastic modulus for a given surface material
λ_p Elastic modulus for a given solid particle type
μ_a Viscosity of air$[m^2/s]$
μ_f Viscosity of a fluid$[m^2/s]$
μ_w Viscosity of water$[m^2/s]$
μ_T Turbulent viscosity$[m^2/s]$
$\bar{\rho}_a$ Bulk density of air $[g/m^3]$
$\bar{\rho}_p$ Particle bulk density [or LWC for droplets; ICC for ice crystals] $\left[g/m^3\right]$
ρ_a Density of air $\left[kg/m^3\right]$
ρ_p Particle material density $\left[kg/m^3\right]$
ρ_w Density of water $\left[kg/m^3\right]$
σ Boltzman constant [5.670×10^{-8} W/(m^{2}K^4)]
τ_f Characteristic time of flowfield $[s^{-1}]$
τ_v Particle momentum response time $[s^{-1}]$
$\vec{\tau}_{wall}$ Wall shear stress$[N/m^2]$
χ Parameter that determines the sticking velocity range for a given ice crystal size

Subscripts

d	Droplet
f	Fluid
ic	Ice crystal
w	Water
∞	Free stream

1. Introduction

Aircraft manufacturers are constantly facing the challenge of minimizing production and operation costs while maintaining a high level of safety. One safety issue that needs to be addressed from the initial design phase up to the certification of the aircraft is its protection against in-flight icing. Ice that accretes on an aircraft can drastically affect its handling characteristics. Even though most aircraft offer an adequate level of protection through anti-/de-icing Ice Protection Systems (IPS), full protection of the complete aircraft can never be achieved due to the limited energy available onboard. As a result, ice accretion still remains a major cause of incidents and accidents.

Examples are numerous. In 1992 a twin turboprop aircraft seating 4 crew members and 44 passengers crashed due to ice build-up on the wings, killing all onboard [1]. All exposed surfaces, not only lifting ones, can be prone to icing. For example, ice blockage of the pitot tube is currently being investigated as one of the possible causes for the crash of a commercial airliner in June 2009 [2], killing all 216 passengers and 12 crew members. Engines can also be affected by ice. Recent incidents involved aircraft engines that suddenly lost power during flight. Even if those are incidents and not accidents, they have initiated growing concerns in the industry [3], as engines were previously considered to be generally well protected against most known icing hazards.

This chapter introduces aero-icing and the current requirements for certification into known icing conditions. A new icing hazard will also be presented: the ice crystal threat to engine safety. Once the problem is well posed, a cost effective solution can be developed. In this work a CFD-based approach to ice crystal simulations is proposed, to provide a numerical representation of ice crystals within complex turbomachinery environments, and to better understand the associated threat.

1.1 In-flight Icing

In-flight icing is a naturally occurring weather hazard that results from supercooled liquid water droplets freezing upon impact on an aircraft surface, such as wing, nacelle, windshield, etc. Such droplets are referred to as 'supercooled' due to their ability to remain liquid at temperatures well below the freezing point (0℃). The density of supercooled droplets in a cloud, or the 'Liquid Water Content (LWC)', is one of the main parameters affecting icing severity: the higher the LWC, the higher the rate of ice accretion and, thus, the mass of ice that needs to be removed. The temperature also affects the type and shape of ice. A study conducted by Schultz and Politovich [4] reviewed many icing incidents and concluded that most icing events occurred at temperatures between 0°C and -20°C. This study surveyed a database of PIREPS* from airplanes flying over the Continental United States between March 13th and 25th, 1990 (Figure 1-1). Below -40°C water droplets freeze and, consequently, do not pose a threat to airframes since they simply bounce off.

In a given icing environment, the icing potential depends on the aircraft, its flight altitude, airspeed, as well as the meteorological conditions. Commercial jets are the least vulnerable to icing due to their higher airspeeds, and since they have more energy available to power their IPS. Such aircraft also fly at higher altitudes (between 30,000 and 40,000 feet)† where temperatures are colder than -40ºC, as opposed to turboprops or some regional jets that are flying between 18,000 and 30,000 feet where the temperature ranges between -15ºC and -40ºC. Even at such low temperatures, however, ice crystals can present a potential icing hazard for the engines. This issue will be discussed in section 1.2.

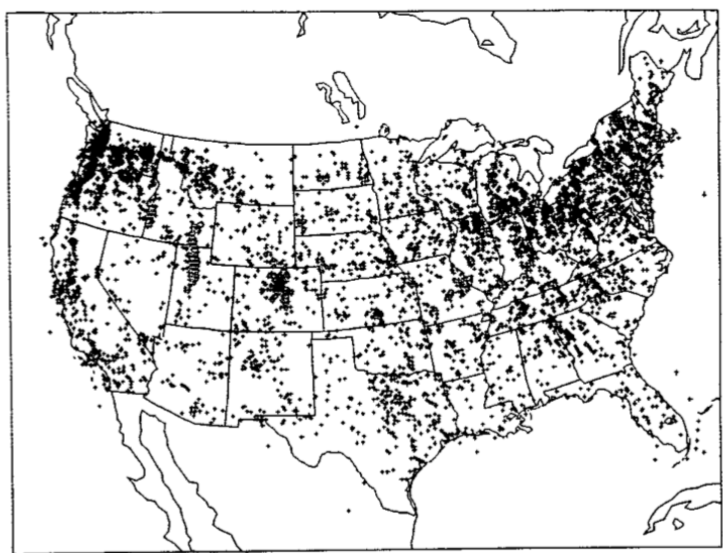

Figure 1-1 Aircraft icing PIREPS reporting an intensity greater than 'trace' in the United-States between March 13th and 25th, 1990 *[4]*

---

* PIREPS are pilot reports of actual weather conditions encountered during flight. They express icing intensity as: negative, trace, trace/light, light/moderate, moderate/severe, and severe.

† http://www.yarchive.net/air/airliners/cruise_altitude.html

Ice can be broadly defined as being rime, clear/glaze or of mixed type (Figure 1-2):

- Rime ice occurs when liquid water droplets freeze immediately on impact, generally at temperatures well below freezing point. Typical cloud droplet sizes of about 20-40 microns result in no droplet coalescence before freezing, and causes the ice form to be rough with an opaque milky appearance due to trapped air between freezing sections. Rime ice accretion occurs mainly between -10℃ and -20℃, but may also occur up to -40℃ in some cases. Rime ice is characterized by an aerodynamic shape, with most of the performance degradation arising from surface roughness [5].
- Glaze/Clear ice forms at temperatures just below 0℃, when supercooled droplets impact and only partially freeze, causing the remaining water to runback along the surface, coalesce with other droplets and, finally, freeze completely when all the latent heat of freezing is released. The result is an ice shape that is clear and smooth, with very little air enclosed. Glaze ice is characterized by horn formations that adversely affect the lift and drag characteristics of the surface.
- Mixed ice forms due to a combination of rime and clear ice that results from different droplet sizes. Larger droplets tend to runback and coalesce to form glaze ice, while smaller ones freeze on impact to form rime ice.

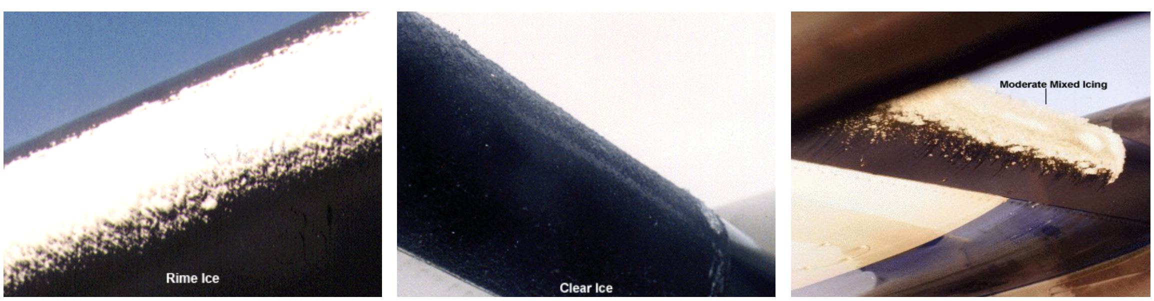

Figure 1-2 Photographs of rime (left), clear (center) and mixed (right) ice *[courtesy NASA Lewis Research Center]*

1.1.1 Airframe and Induction Icing

Aircraft icing accounts for about 12% of all weather-related airline incidents [6]. This study conducted between 1990 and 2000 showed that a majority of incidents occurred due to induction-type icing, which affects the aircraft engine (52%). Induction icing refers to ice build-up in the carburetor in the case of piston-driven engines, or air blockage of the intake due to ice build-up in fuel-injected engines.

Structural airframe icing is the second most dangerous icing hazard (40%). Ice that forms on a wing causes a loss in maximum lift, adversely affecting handling qualities of the aircraft, and significantly increasing drag. Ice can also accumulate on any exposed frontal surfaces of the airplane and, thus, is not necessarily restricted to only the wing, propeller or windshield. Engine intakes, antennas, and entry/exit vents, for example, may also be at risk.

Icing in engines has previously been limited to the analysis of frontal components such as the spinner, nacelle, fan blades and frontal stator vanes (Figure 1-3). Ice that accumulates on such surfaces can:

- Cause a blockage of the primary flow path;
- Generate vortices, leading to an unstable compressor operation that enhances stall and surge;
- Cause vibrations if ice accumulates on rotating components.

Figure 1-3 Icing on engines due to supercooled liquid droplets affect components such as the spinner, nacelle, fan or Inlet Guide Vanes (IGV) *[courtesy of aerospaceweb.org]*

Ice pieces can shed from the inlet structure and may create a risk of Foreign Object Damage (FOD) when they hit the fan or any downstream components. No special considerations are made to prevent ice accumulation on fan blades, since speeds above idle ensure a centrifugal load that sheds ice outwards towards the bypass passage [7]. Other components are equipped with an IPS that, in most cases, uses bleed-air from the compressor to melt any existing ice or prevent accretion. Components located in the core of the engine are not usually protected by any anti-icing systems since the operating temperatures are sufficiently high for ice not to accumulate. This statement has, however, been recently challenged [3, 8].

1.1.2 Icing Certification

The Federal Aviation Authority (FAA) has defined a set of regulations that require any aircraft that enters into service to demonstrate compliance of their ice protection systems (i.e. that the aircraft is able to operate safely under continuous and intermittent maximum icing conditions). These conditions are detailed in Part 25 Appendix C [9] for commercial aircraft, through icing envelopes linking the mean droplet diameter (up to 50μm for intermittent maximum; up to 40μm for continuous maximum) to cloud liquid water content (Figure 1-4), altitude and temperature (Figure 1-5).

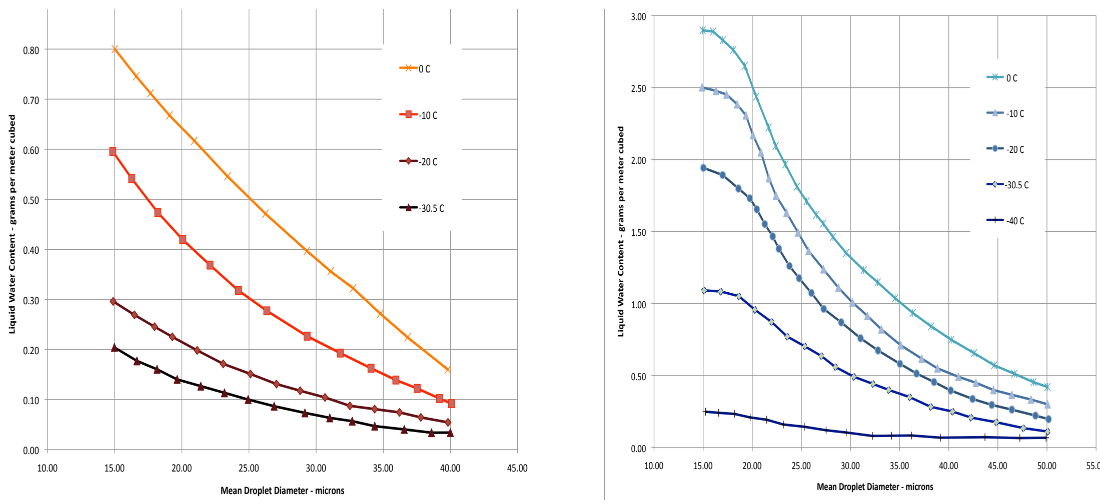

Figure 1-4 Constant temperature curves for continuous (left) and intermittent (right) envelopes, as a function of mean droplet diameter and liquid water content *[data from [10]]*

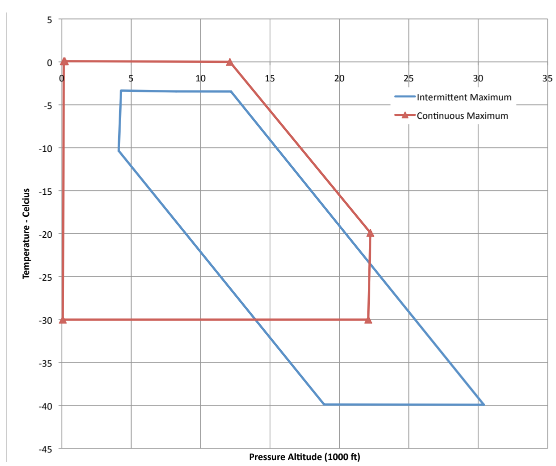

Figure 1-5 Continuous and intermittent maximum envelopes defined by altitude vs. ambient temperature *[data from [10]]*

It is important to note that while these certification standards provide sufficient protection for a majority of atmospheric conditions encountered during flight, they do not cover freezing rain/drizzle (i.e. conditions with much larger droplets, or a mixture of supercooled droplets and ice particles)[‡].

1.1.3 Supercooled Large Droplets and Ice Crystals

More recent aircraft incidents and accidents have revealed the existence of cloud characteristics beyond the certification envelope defined by Appendix C. Two major concerns are the presence of Supercooled Large Droplets (SLD) of diameters in the range of 40-400μm, and tiny ice crystals of about 50-200μm.

SLD conditions are typically produced by freezing rain/drizzle that develops when snow falls into a warm air front to produce rain drops, which then fall back into a sub-freezing layer of air to become supercooled (freezing) rain, or when droplets falling at different speeds collide with one another and coalesce to form larger drops. The physics that represent typical droplets within Appendix C cannot be applied directly to SLD, since their deformation, break-up and the drag associated with deformed droplets should also be accounted for [11]. Post-impact coalescence, splashing and associated runback affect also the ice shapes produced under SLD conditions [12]. SLD impacts tend to be more ballistic, and may result in only partial freezing because of their larger size, causing remaining residual droplets to coalesce, runback and freeze beyond the physical extents of the IPS (Figure 1-6) [13].

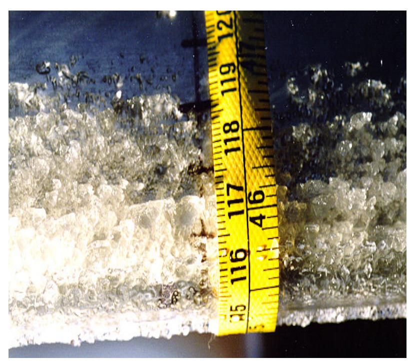

Figure 1-6 Ice formed by SLD on a NACA23012 airfoil [13] (left) and C95-3918 rotor (right)
[courtesy NASA Icing Research Center]

Abrupt losses of power and flameouts experienced by aircraft engines during flight generally in tropical regions and at high altitudes, have prompted researchers to believe that ice crystals could be a potential threat, even in the absence of water droplets. Tropical systems create clouds that span up to 50,000 feet high. Their convective currents drive large volumes of moisture upwards to create ice crystals

‡ http://www.skybrary.aero/index.php/Icing_Certification#Icing_Certification

that settle near the top (Figure 1-7). The solid nature of these crystals does not pose any significant threat to external airframe, since they simply bounce off at low temperatures, but can be a serious concern when a change of phase to liquid is made possible, such as in an engine core-flow. The radar reflectivity of ice crystals is about 5% of the average raindrop, which makes them undetectable by current airborne weather radars when water droplets are absent. Aircraft may then fly directly into a fully glaciated cloud without any warnings.

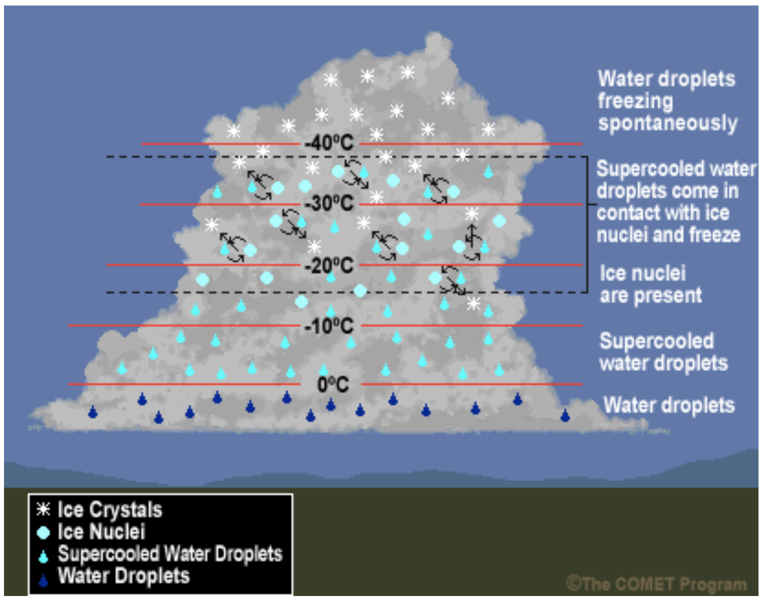

Figure 1-7 The process of convection that creates ice crystals at high altitudes *[courtesy of www.meted.ucar.edu]*

Joint efforts by research establishments, industry and national aviation regulatory agencies aim at defining a new set of regulations: extensions 'Appendix X' for SLD conditions [10] and 'Appendix D' for ice crystals [14]. Compliance to any of these conditions requires extensive flight tests to be carried out, with adequate instrumentation. Since ice crystal conditions cannot be found easily in nature, or reproduced accurately during experiments, there is an increased interest in using engineering simulation tools to complement these research and development efforts. In this regard, there has been a lot of recent advances in simulating SLD using computer codes such as FENSAP-ICE [15] and LEWICE [16]. Ice crystals, however, have not yet been extensively studied and their physics are not yet fully mastered. It is this motivation that drives the development of a numerical tool that can provide extended capabilities to model ice crystals and, by working hand-in-hand with the industry, complement any experimental investigations. In return, experiments will provide the necessary data to improve the numerical models. A better understanding of ice crystals will also guide the engine design phase and, consequently, decrease product development time and associated icing certification costs.

1.2 The Ice Crystal Threat to Aircraft Engines

Engines have become so reliable that pilots can go though an entire career without ever experiencing an engine shutdown. However, a series of turbofan malfunctions in tropical regions containing deep convective clouds have lately tarnished the image of engine total reliability [3]. Mason *et al.* [17] provided an in-depth case study into 46 engine shut-down events caused by ice contamination inside the engine core. The events occurred above 22,000 feet, the extreme upper limit where supercooled droplets exist, and usually happened in the idle-descent phase of flight.

Ice crystals should bounce off any cold, dry surfaces and, consequently, do not pose a threat for external airframes. However, the same cannot be said for internal engine components. Mason cites conclusive evidence of the presence of high concentrations of ice crystals during a series of engine shutdown events:

- The low reflectivity of ice crystals makes them difficult to detect on radar. Radar devices installed on commercial airplanes bias readings based on particle size. This means that while pilots may be able to accurately determine regions of hailstorms, large concentrations of tiny ice crystals may not be detected. All events analysed by Mason occurred in regions containing very little or no liquid water droplets. The pilots however incorrectly reported rain on the windshield which corresponded to ice crystals melting on the heated surface.
- Aircraft equipped with ice detectors (which initiate de-/anti-icing systems) did not switch on during the engine shutdown events, indicating the absence or inadequate concentrations of liquid water droplets.
- Close inspection of data from total air temperature probes showed that ice crystal contamination was felt as an uncharacteristic, erratic fluctuation in readings. The events were also highly unpredictable, with some aircraft flying before and after the event remaining unaffected (Figure 1-8).

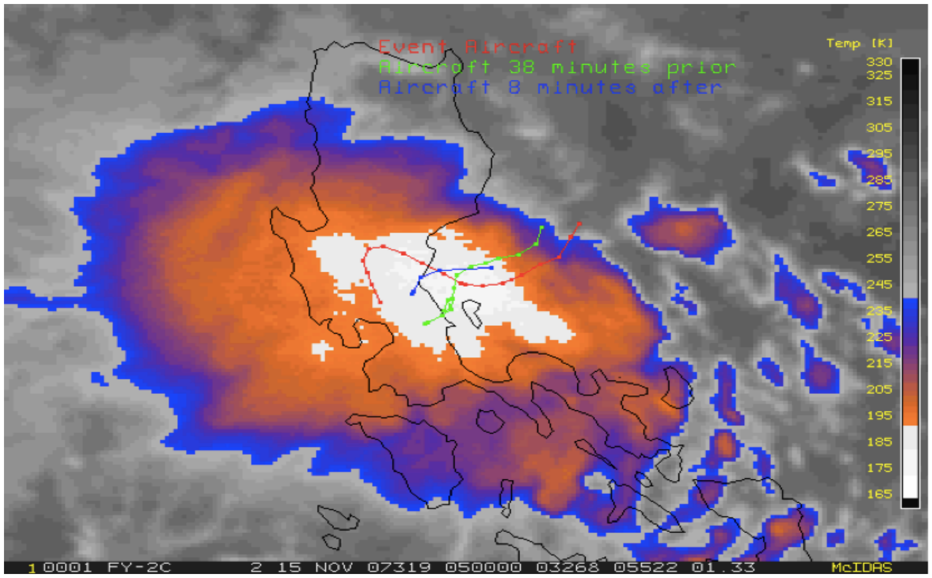

Figure 1-8 Satellite image of a convective cloud and superimposed flight-paths of aircraft experiencing engine rollback (green) and not being affected (red and blue) [8]

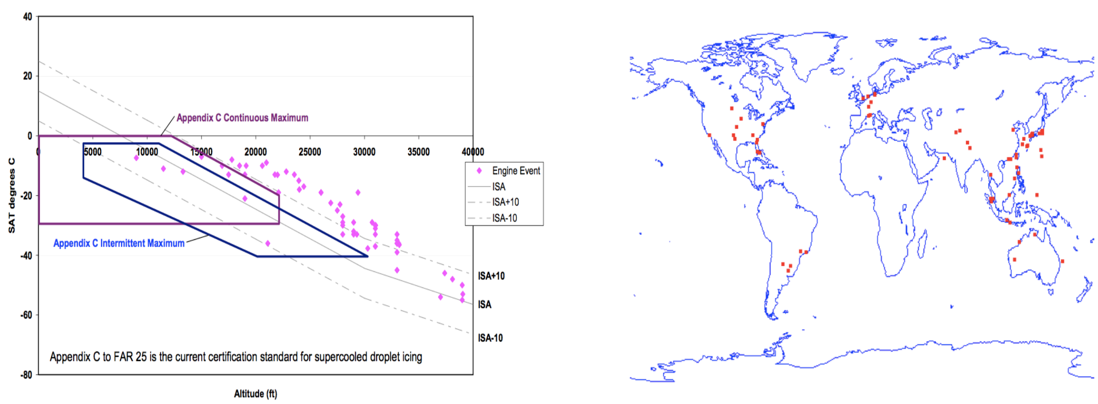

Figure 1-9 Event occurrences outside the current Appendix C envelope with global map showing that most events occur in tropical regions [8]

Based on the increasing frequency of events that have now occurred outside the Appendix C envelope (Figure 1-9), the following hypothesis on ice crystals as a cause of internal core icing has been made by Mason:

- Deep convective clouds found in tropical regions contain high concentrations of moisture that condense rapidly as they rise up to form tiny ice crystals.
- Limited radar capabilities of the aircraft result in high concentrations of crystals not being detected. Although convective cloud cover can be seen on radar, the regions above the cloud that contain these ice crystals can range up to 30 km away from the cloud center. The increasing amount of air traffic

and frequency with which storm fronts appear make circumnavigating around these potential hazard areas difficult.

- Engines that encounter high ice crystals concentrations ingest these particles into their core. Crystals having more inertia are then less affected by the airflow and, hence, tend to have nearly straight-line or ballistic trajectories. Smaller droplets on the other hand have a greater tendency to be expelled through the outer bypass passage, since they may slow down, break up and are then more susceptible to centrifugal forces applied by the rotating components.
- Ingested crystals with high axial momentum enter the initial stages of the low pressure compressor. As higher temperatures are experienced further downstream, the ice crystals melt and impact on rotating and static components. The water-film interface that forms onto the component enhances the sticking efficiency of impinging ice crystals.
- A local reduction of temperature below zero caused by ice crystals that stick to the film interface results in an ice formation on the surface. Further impingement of liquid on the ice surface may allow ice to rapidly grow.

Apart from FOD caused by ice shedding, ice accumulation in the compressor can result in serious operational hazards. Shed ice can enter the combustion chamber and decrease the burner efficiency, eventually causing an engine flameout and a sudden power-loss. Most engines, however, can withstand an acceptable level of water ingestion and maintain steady-state operation. If the water/air ratio is very high, more fuel is required to provide the same amount of thrust [18]. The operating requirements of the engine may begin to exceed the manufacturers design acceleration schedule, resulting in an engine ‘rollback’ or a lack of throttle response, and a sudden decrease in thrust. The compressor may surge as a result of the increasing operating requirements and then, eventually shutdown.

1.3 A CFD Methodology Towards the Understanding of Ice Crystals

Experimental analyses of engine icing are expensive and not reliable enough to provide an accurate characterization of the ice crystal environment. Icing test facilities have tried to accommodate ice crystal simulation by either freezing supercooled droplets or using ice shavers. Figure 1-10 shows the difference between a man-made crystal and a naturally occurring one. Such inadequate representations of ice crystals can lead to a misinterpretation of the icing dynamics, since the shape of the crystal affects its trajectory in a flow field and, consequentially, its impingement location on a surface. Mounting instrumentation inside the engine to record data and visualize crystal impacts remains a challenge, and is expensive because of the compact nature of a turbomachine. Furthermore, since engine operating conditions change with ambient conditions and airspeed, locations of ice accretion sites within the engine core can vary, making experimental setups and data acquisition difficult.

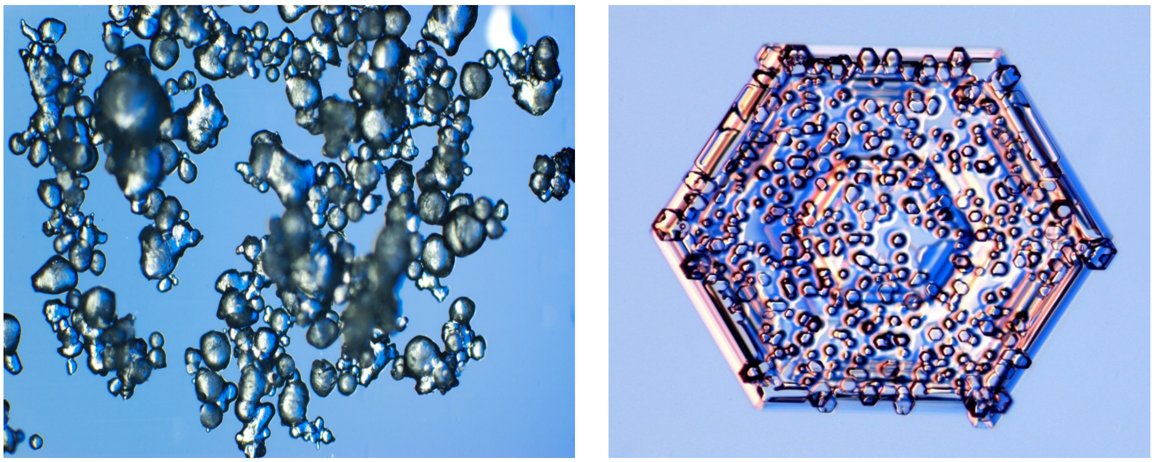

Figure 1-10 Difference between ice crystals produced by freezing liquid droplets (left) and naturally occurring ones (right) *[courtesy of http://www.its.caltech.edu/~atomic/snowcrystals/]*

Those limitations make numerical modeling a cost-effective complement to experimentation. Simulations can establish mathematical models that best represent the physics of ice crystals, help validate experimental correlations for bouncing, splashing and shedding, for example, and provide insights of ice accretion inside engine components. On the other hand, experimentation provides CFD with validation data and better understanding of ice crystal physics. Such a close interaction allows for improvements to be made in ice prediction codes and helps increasing confidence in the application of numerical codes to certification.

While studying the effects of helicopter blades in mixed-phase accretion, Lozowski *et al.* [19] developed a numerical model to compare with experimental ice results. The model, developed in cooperation with Cansdale and McNaughtan [20], is based on a classical quasi-steady heat balance equation, where the ice accretion process is in thermal equilibrium and, consequently, the sum of all heat sources and sinks is zero. The collection efficiency for droplets, defined as the mass flux of impinging droplets that hit the iced surface, is calculated using an empirical correlation derived from the work of Langmuir and Blodgett [21] and applied on a cylinder. The collection efficiency for ice crystals is approximated from observations of ice crystal trajectories and collisions on a wall. The crystal trajectories were found to be essentially straight-line, with little deviation as they approached the wall. The sticking efficiency is based on the assumption that all impinging ice crystals stick when the surface is 'fully wet', or at least an adequate fraction of crystals stick to provide a sufficient energy sink to freeze all the existing water. No crystals are assumed to stick when conditions are 'fully dry'.

A more recent attempt to model ice crystals in engines was carried out by TSIICE created by Trebor Systems[§]. TSIICE is an icing methodology dedicated towards analyzing ice accretion in aircraft engines. The method is two-dimensional, focuses on fan and compressor stages, and primarily on leading edge ice. Pseudo three-dimensional features are being captured using experimental correlations. TSIICE employs what is referred to as a 'zero net mass' algorithm to account for splashing of an existing film due to ice crystal impingement [22], where an impacting crystal causes an equivalent mass of water-film to be removed. This is a simplification of the actual process, since some crystals may partially melt, adding to the film height, whilst others may bounce off and cause water to splash. In addition to ice accretion, TSIICE is able to predict ice-shedding characteristics of an accreted mass of ice, based on adhesion characteristics of the ice-surface interface. TSIICE uses a threshold value of 5,860 N/m^2 [23] as criteria to shed glaze ice, which is based on the centrifugal loads experienced by ice.

FENSAP-ICE, a second-generation icing simulation code, consists of a suite of integrated modules designed to analyze and predict performance degradation within the in-flight icing envelope, as well as beyond it (e.g. SLD). FENSAP-ICE includes different modules for flow prediction (FENSAP), droplet impingement (DROP3D), ice accretion/water runback (ICE3D), and conjugate heat transfer (CHT3D). FENSAP-ICE has been extensively validated for, respectively, 2-D and 3-D external aerodynamics, water droplets impingement and ice accretion [24, 25]. Recent developments in the FENSAP-ICE software include FENSAP-TURBO, an extension of FENSAP that handles rotating turbomachinery components and is able to simulate flow and droplet trajectories throughout multiple stages [26, 27]. For steady-state analysis, the interaction between rotating and non-rotating components is simplified by using a mixing-plane approach [28].

[§] http://treborsys.com/TSIICE.aspx

The focus of this research is to extend FENSAP-ICE to ice crystals in multiphase flows. The advantages of using the existing tools to extend their range of application to ice crystals are numerous:

- A well integrated set of modules allows seamless integration of solutions between each module, without the need to write intermediate file converters.
- A robust framework implies that it has been extensively validated and, consequently, reduces the implementation time significantly.
- Since the existing turbomachinery framework is already able to simulate droplet impingement, its extension to ice crystals can be handled with ease.
- The generalized nature of FENSAP-ICE allows simulating a wide variety of problems.

1.4 Thesis Overview

Current experiments have not allowed a clear insight about ice crystals in engines. Experiments with natural ice crystal conditions remain difficult and expensive, since the morphology of ice crystals cannot be reproduced accurately using present icing tunnel techniques, and require new technologies to be developed. This is where numerical simulations can play a significant role. For example a numerical model can offer insights into the types of experiments and data required to improve model predictions.

The objective of this work is to extend DROP3D and ICE3D to simulate impingement and ice accretion due to ice crystals. Chapter 2 will address the modeling of ice crystals and water droplets in a steady, mixed-phase, uncoupled flow. A discretization procedure based on a finite element method is also outlined. Chapter 3 will explain the methodology used to include ice crystal impingement and bouncing characteristics required to extend the current finite volume formulation of the Messinger Model [29] in ICE3D. The icing model is then validated in Chapter 4 using available experiments from the National Research Council of Canada (NRC) tests on an unheated cylinder [19] and from Cox & Co Tunnel tests on a NACA0012 airfoil [30]. Chapter 5 will summarize the limitations of the model and will finally propose some future improvements.

2. Droplet and Ice Crystal Impingement

The numerical accuracy of the shape and mass of ice accreted on the aircraft surface is affected by the precision of the preceding particle impingement calculation. There are two major numerical approaches for assessing impingement: Lagrangian, based on particle-by-particle tracking, and Eulerian, where the particles form a separate phase governed by continuity and momentum equations.

The Lagrangian approach requires the integration of trajectories of incoming particles from predefined seed points upstream of a solid body. Each particle trajectory is defined by equations of motion derived from the forces acting on the particle. Each trajectory is integrated with an appropriate numerical integration scheme applied to this equation of motion with the given initial and boundary conditions. The level of detail in determining impact zones on solid walls is proportional to the number of trajectories launched from the upstream location, however the computational cost increases as the number of particle trajectories increases [31].

The Eulerian approach to tracking particles is based on the treatment of the dispersed particle cloud as a continuous medium and does not require the integration of individual particles. Since the supercooled droplets are usually small and the number of droplets contained in a suitably defined control volume is large, bulk properties such as liquid water content, particle velocity and particle drag can be defined. With this approach there is no need to integrate each particle path through the flow-field, hence the selection of suitable seed areas to capture the impingement zones with the required accuracy is avoided, thus reducing the number of degrees of freedom required for a solution, compared to the Lagrangian approach. This approach is the method implemented in DROP3D in the context of a finite element framework and is described in details in the sections to follow. Note that a full list of symbols used in this chapter is presented in the *List of Symbols* section at the beginning of this document. Subscripts 'p' maybe interchanged by 'ic' or 'd' to represent ice crystals or droplets properties respectively.

2.1 Modeling Assumptions

Although the justifications for the selection of the Eulerian approach, rather than the Lagrangian, for droplet impingement have already been outlined [32], the validity of these assumptions has to be re-evaluated for ice crystals impingement in order to assess the feasibility and limitations of extending the current solver, DROP3D, to model ice crystals dynamics.

2.1.1 ***Continuum Hypothesis***

The continuum hypothesis is an approximation that applies to both carrier and dispersed phases in a flow. This approximation allows the variation of properties such as temperature, pressure, velocity or density over a given space to be continuous from one point to another. For the dispersed phase, a sufficient number of particles (10^4) are required to maintain a stationary average of properties inside a given elemental volume, such that any deviation in the volume or number of particles would keep the average unchanged [33]. This hypothesis is at the foundation of the Navier Stokes equations and its validity has been verified for air in many fluid mechanics applications [34]. The following parameters taken from [17, 19, 35, 36] will be used to validate the continuum hypothesis for ice crystals in turbomachinery applications

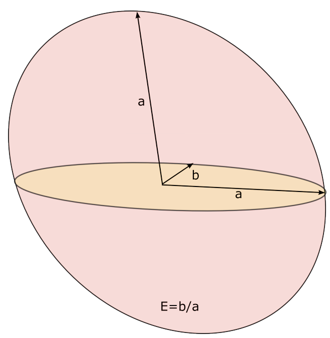

Figure 2-1 Ice crystal modeled as an oblate spheroid with semi major axis 'a' and semi minor axis 'b'

$\overline{\rho}_{ic}$	2.5-9 g/m^3
ρ_{ic}	917 kg/m^3
$2a$	100-1000 μm
E	0.05-0.5

Table 2-1 Parameters required to validate the simulation of crystals in the current DROP3D framework

where $\overline{\rho}_{ic}$ is the Ice Crystal Content (ICC) at free-stream, ρ_{ic} is the ice crystal material density, $2a$ is the crystal broadside length and E is the crystal aspect ratio. In order to simplify the mathematical complexity, an equivalent sphere model is used, where, d_{eq} is defined as the volumetric equivalent spherical diameter of a crystal modeled as an oblate spheroid (see section 2.2). The volume of an oblate spheroid with semi major axis 'a' and semi minor axis 'b' is

$$V_{ic} = \frac{4}{3}\pi a^2 b \qquad \textbf{Eq. 2-1}$$

Equating Eq. 2-1 with the volume of a sphere and substituting $E = b/a$ yields d_{eq}

$$d_{eq} = 2(a^2 b)^{1/3} = 2aE^{1/3} = [100\mu;1000\mu][0.05;0.5]^{1/3} \approx [40\mu;800\mu] \qquad \textbf{Eq. 2-2}$$

A cubic fluid element of side L, defined also as the distance between particle centers, enclosing a spherical particle with equivalent volume to that of an ice crystal is shown in Figure 2-2. The volume fraction for such a sphere enclosed within the cubic element, α_{ic} is

$$\alpha_{ic} = \frac{\pi d_{eq}^3}{6L^3} = \frac{\bar{\rho}_{ic}}{\rho_{ic}} \qquad \textbf{Eq. 2-3}$$

Typical values for $\bar{\rho}_{ic}$ and ρ_{ic} yield values of α_{ic} in the range from 10^{-6} to 10^{-5}. The ratio of inter-particle spacing L to the equivalent diameter d_{eq} can be defined by reformulating Eq. 2-3 as

$$\frac{L}{d_{eq}} = \left(\frac{\pi}{6\alpha_{ic}}\right)^{1/3} = \left(\frac{\pi}{6\left[10^{-5};10^{-6}\right]}\right)^{1/3} \approx [37;80]$$

The order of the inter-particle spacing between crystals is large and therefore, ice crystals may be treated as being isolated particles in the flow, and, therefore not subject to interacting forces or transfers of energy (such as wake-induced drag, or energy transfer due to collisions) with neighbouring particles.

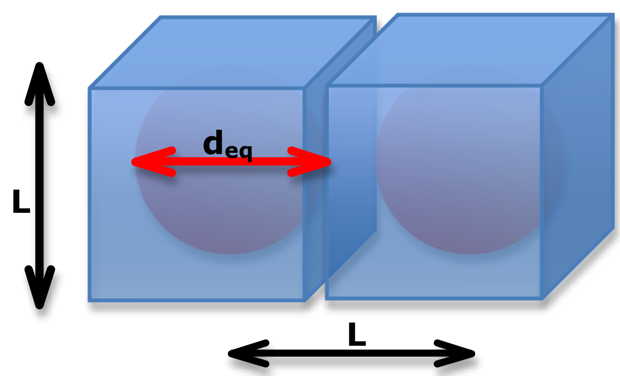

Figure 2-2 Cubic fluid element enclosing spherical particle

Given that 10^4 particles are required to maintain a stationary average, the limiting volume V_0 of a cube containing this amount of crystals is computed as follows

$$V_0 = 10^4 \left(\frac{L}{d_{eq}} \right)^3 d_{eq}^3 \quad \textbf{Eq. 2-4}$$

The length of such a cube L_0 is therefore

$$L_0 \sim 20 \left(\frac{L}{d_{eq}} \right) d_{eq} \quad \textbf{Eq. 2-5}$$

Using the values obtained for d_{eq} and the lower bound for L / d_{eq}, the limiting length L_0 required for the continuum hypothesis to be valid is 3-60cm. This dimension must be compared to the characteristic length scale of the system being analyzed, which in the case of ice crystal icing, is of the order of the mean chord length of a compressor blade in the engine core. This is about 6-10cm.

Given that the ice crystal problem in engines is primarily caused by crystals in the 100-200μm range, the continuum hypothesis holds for such sizes but is invalid when crystal sizes exceed about 600μm. The values used in the calculations, however, depict ideal conditions and thus, further investigation is required to verify the applicability of the continuum approximation for larger crystal sizes. For instance, successive compression through the initial stages of the compressor can locally increase the ice crystal volume fraction, thereby reducing the inter-particle spacing quite significantly. Crystals may also break-up due to aerodynamic forces or collisions with surfaces, downsizing as they pass through rotating components. Such factors lead to a smaller limiting length L_0 that is smaller than the mean blade chord, and therefore the continuum hypothesis may remain applicable even for larger crystal sizes.

2.1.2 __Dilute Gas Particle Flow Assumption__

A dilute flow is classified as one in which particles motion is primarily governed by the fluid forces. This assumption establishes the importance of momentum coupling effects between the continuous fluid and dispersed phases, and allows for simplifications in the governing equations of the dispersed phases. Di Giacinto *et al*. [37] stated that the viscous shear and pressure gradient terms that account for the interaction between particles in a field is inversely proportional to the ratio between particle distance and diameter. The L / d_{eq} ratio has already been shown to be large and therefore the viscous and pressure terms may be safely ignored when constructing the equations of the dispersed phase. The particle Stokes number, St_p can be expressed as

$$St_p = \frac{\tau_v}{\tau_f} \qquad \textbf{Eq. 2-6}$$

Where τ_v represents the momentum response time for the particle in the flow, and τ_f is a representative time characteristic of the flow. For ice crystals, the inertia parameter, K_{ic}, defined in Eq. 2-28 (excluding the non-dimensional terms U_∞ and L) can be used to define τ_v, while the characteristic length scale L of a compressor blade, and an approximate order of magnitude for the free-stream flow velocity are used to define τ_f

$$\tau_V = \frac{\rho_{ic} d_{eq}^2 E^{2/3}}{3\mu_a} \approx \frac{917[10^{-5};10^{-3}]^2[0.05;0.5]^{2/3}}{3[1\times 10^{-5}]} \approx [10^{-5};10^{0}]s^{-1}$$

$$\tau_f = \frac{L}{U_\infty} \approx \frac{[10^{-1};10^{0}]}{[10^{1};10^{2}]} = [10^{-3};10^{-1}]s^{-1}$$

$$St_p = \frac{[10^{-5};10^{0}]}{[10^{-3};10^{-1}]} = [10^{-4};10^{3}]$$

The lower limit of $St_p << 1$ implies that smaller crystals have adequate time to respond to local changes in the flow-field. Therefore their motion is primarily governed by fluid forces that act individually on each particle. The main driving force in the governing equations for these small crystals is the induced drag caused by the relative velocity between the fluid and each particle. A mass loading ratio Z, which is the ratio of ice crystal content, $\overline{\rho}_{ic}$, to the bulk density of air, $\overline{\rho}_a$, can be defined

$$Z = \frac{\overline{\rho}_{ic}}{\overline{\rho}_a} \qquad \textbf{Eq. 2-7}$$

The St_p and $Z \approx 10^{-2} < 0.1$ establish a one-way momentum coupling between smaller ice crystals and the airflow, in which the effect of drag on the fluid is negligibly small because of the low volume fraction of the dispersed phase. A higher St_p of 10^3 implies particle trajectories that remain essentially unchanged in the flow, and their motion is primarily governed by inter-particle collisions. The necessity to stay within the limits of dilute gas particle flows, to be consistent with the current droplet module in FENSAP-ICE, therefore limits the applicability of ice crystals to simulations involving small crystal sizes. Additionally, any energy transfer between dispersed phases (droplet and ice crystal) or between the dispersed phases and the fluid (air) is ignored and the equilibrium temperature of each dispersed phase is considered to be the temperature of the fluid phase. Each set of dispersed phase equations can then be solved in an uncoupled manner by ignoring inter-particle phase change (solid-liquid or vice versa). The one-way coupling between the dispersed and continuous phases also permits the independent solution of a given flow field problem before solving the dispersed phase equations to determine the impingement locations of the particles.

2.2 Ice Crystal Drag

The driving force for ice crystal motion in a flow regime is the induced drag, caused by the difference in relative velocity between the air and the particle cloud at any given point in space. The common practice in evaluating the drag force is to assume that the particles are spherical and rigid [38-40]. This is indeed a valid approach for water droplets, but may not necessarily suffice in the case of ice crystals. Magono and Lee [41] have previously classified ice crystals based on geometry. A summary of some crystal types is presented Figure 2-4. The discussion that follows will be based on the most basic crystal type that will be considered for modeling purposes: the hexagonal prism, shown in Figure 2-3.

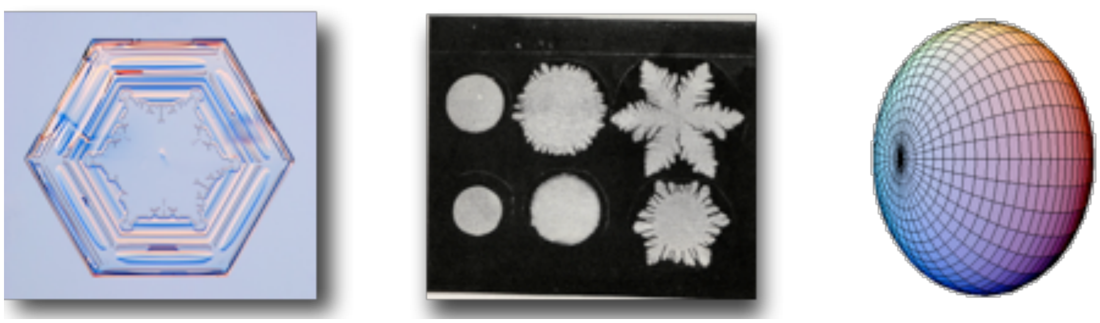

Figure 2-3 Basic ice crystal forms as the hexagonal prism (left) can be modeled as thin oblate spheroids (right).

Previous studies [42, 43] have shown that the hydrodynamic behavior of a hexagonal plate-like prism can be sufficiently approximated by that of a circular disk. Pitter *et al* [35] further proceeded to show that a disk of a finite aspect ratio has properties similar to a thin oblate spheroid at low to intermediate Reynolds numbers. The Reynolds number for any particle in the dispersed phase is given by

$$\mathrm{Re}_p = \frac{\rho_a \left| \vec{v}_a - \vec{v}_p \right| d_p}{\mu_a}$$ **Eq. 2-8**

where ρ_a is the air density, $\vec{v}_a$ is the air velocity vector, $\vec{v}_p$ is the particles velocity vector, d_p is the particle diameter, and μ_a is the viscosity of air. The drag coefficient C_d is calculated from the following correlations determined by Pitter [35], for crystals with E of 0.05 but works reasonably well for values up to 0.5.

Figure 2-4 Magono and Lee summary of ice crystal shapes [41]

$\underline{\mathrm{Re}_{ic} \leq 0.01}$

$$C_d = \frac{8m}{3\mathrm{Re}_{ic}}\left[1+\frac{m\mathrm{Re}_{ic}}{48}+\frac{m^2}{1440}\mathrm{Re}_{ic}^2\ln\left(\frac{\mathrm{Re}_{ic}}{2}\right)\right]$$
$$m = 12e^3\left\{e\left(1-e^2\right)^{1/2}+\left(2e^2-1\right)\tan^{-1}\left(\frac{e}{\left(1-e^2\right)^{1/2}}\right)\right\}^{-1} \quad \textbf{Eq. 2-9}$$
$$e = \left(1-E^2\right)^{1/2}$$

$\underline{0.01 < \mathrm{Re}_{ic} \leq 1.5}$

$$C_d = C_{d,OB}\left[1+10^x\right]$$
$$x = \beta_0 + \beta_1\omega + \beta_2\omega^2$$
$$\omega = \log\left(\mathrm{Re}_{ic}\right) \quad \textbf{Eq. 2-10}$$
$$\beta_0 = -0.883$$
$$\beta_1 = 0.906$$
$$\beta_2 = -0.025$$

$\underline{1.5 < \mathrm{Re}_{ic} \leq 100}$

$$C_d = C_{d,OB}\left[1+0.138\,\mathrm{Re}_{ic}^{0.792}\right] \quad \textbf{Eq. 2-11}$$

$\underline{100 < \mathrm{Re}_{ic} \leq 300}$

$$C_d = C_{d,OB}\left[1+0.00871\mathrm{Re}_{ic}^{1.393}\right] \quad \textbf{Eq. 2-12}$$

where $C_{d,OB}$ is the oblate spheroid drag for very low Reynolds numbers, formulated by Happel and Brenner [44]

$$C_{d,OB} = \frac{A}{\mathrm{Re}_{ic}}$$
$$A = \frac{32h}{a\left[\lambda-\left(\lambda^2-1\right)\cot^{-1}\left(\lambda\right)\right]} \quad h = \left(a^2-b^2\right)^{1/2} \quad \lambda = b/h \quad \textbf{Eq. 2-13}$$

For the present study, the ice crystal broadside orientation is considered perpendicular to the flow vectors direction at all times. This implies that the drag experienced by all crystals in a given flow-field is always a maximum value. A more comprehensive drag model would require the determination of tumbling characteristics for ice crystals in time and space. Such a model however would require a more in-depth analysis, that establishes crystal orientations as a function of the properties of a given flow, and would have to be carried out through experimental methods. This is beyond the scope of this work. The drag force acting on an individual ice crystal is

$$\vec{F}_D = \frac{1}{2}\rho_a C_d \left|\vec{v}_{rel}\right| S_{ref} \vec{v}_{rel} \quad \textbf{Eq. 2-14}$$

$\vec{F}_D$ may alternatively be represented using the ice crystals acceleration $\vec{a}_{ic}$ and mass $\rho_{ic} V_{ic}$

$$\vec{F}_D = \rho_{ic} V_{ic} \vec{a}_{ic} \quad \textbf{Eq. 2-15}$$

Combining Eq. 2-14 and Eq. 2-15 and formulating $\left|\vec{v}_{rel}\right|$ in terms of Re_{ic}, the acceleration for a single ice crystal can be determined.

$$\vec{a}_{ic} = \frac{1}{2} C_d \frac{\mathrm{Re}_{ic}\,\mu_a}{\rho_{ic} d_{eq}} \left(\frac{S_{ref}}{V_{ic}}\right) \vec{v}_{rel} \quad \textbf{Eq. 2-16}$$

Since the crystals broadside dimension is always assumed perpendicular to the flow velocity vector, the projected area seen by the velocity vector is a circle of radius 'a'. Using the ice crystal volume defined in Eq. 2-1, the ratio S_{ref} / V_{ic} is

$$\left(\frac{S_{ref}}{V_{ic}}\right) = \frac{3}{4b} = \frac{3}{4Ea} \quad \textbf{Eq. 2-17}$$

Substituting Eq. 2-17 into Eq. 2-16, and replacing a in terms of E and d_{eq} in Eq. 2-2, the final expression for the acceleration of an ice crystal is given by

$$\vec{a}_{ic} = \frac{3}{4} \frac{\mu_a}{\rho_{ic} d_{eq}^2 E^{2/3}} C_d \,\mathrm{Re}_{ic}\, \vec{v}_{rel} \quad \textbf{Eq. 2-18}$$

2.3 Governing Equations for Multiphase Flow

The Eulerian approach is consistent with the dilute gas-particle flow and continuum hypothesis and can be used to formulate the governing equations for the dispersed phase. As stated in the preceding sections, the assumption that the flow is dilute allows for viscous shear and pressure gradients in the dispersed phase flow to be ignored and therefore they can be safely omitted from the momentum equations. When both particle types (i.e. droplets and crystals) are present, the inter-phase coupling that associates mass, momentum and energy transfer due to melting or freezing is ignored (i.e. all phases are considered to be in thermodynamic equilibrium with each other). Both sets of dispersed phase equations are therefore treated in an uncoupled manner in the present study. An airflow solution that establishes a velocity field around a given geometry as well as heat fluxes and shear stresses on the surfaces of the geometry, is computed with the Reynolds-Averaged Navier Stokes (RANS) equations that are complemented by a one-equation turbulence model (Spalart-Allmaras). The air velocity field is a necessary precursor required for the accurate prediction of velocity, liquid water/ice crystal content and collection efficiency of the dispersed phases, while the shear stresses and heat fluxes are necessary for the ice accretion calculation. The mass and momentum equations for any given particle type *'p'* can be represented as [37, 45]

Mass Conservation

$$\frac{\partial\left(\alpha_p\right)}{\partial t}+\frac{\partial\left(\alpha_p v_j\right)}{\partial x_j}=0 \qquad \textbf{Eq. 2-19}$$

Momentum Conservation

$$\frac{\partial\left(\alpha_p v_i\right)}{\partial t}+\frac{\partial\left(\alpha_p v_j v_i\right)}{\partial x_j}=\alpha_p\left[\left(1-\frac{\rho_a}{\rho_p}\right)g_i+a_i\right] \qquad \textbf{Eq. 2-20}$$

The first term on the right side of the momentum equation arises from gravitational and buoyancy forces. The second term is the induced drag, which is different for droplets and ice crystals. The acceleration term for ice crystals has already been defined in Eq. 2-18. The acceleration term for a droplet, which is modeled as an incompressible spherical particle, is defined as follows

$$\vec{a}_d=\frac{3}{4}\frac{\mu_a}{\rho_d d_d^2}C_d\,\mathrm{Re}_d\,\vec{v}_{rel} \qquad \textbf{Eq. 2-21}$$

The drag coefficient C_d for droplets is based on empirical correlations defined as

$$C_d = \frac{24\left(1+0.15\,\mathrm{Re}_d^{0.687}\right)}{\mathrm{Re}_d} \; \mathit{for} \; \mathrm{Re}_d \le 1300 \quad C_d = 0.4 \; \mathit{for} \; \mathrm{Re}_d > 1300 \qquad \textbf{Eq. 2-22}$$

The equations of mass and momentum are non-dimensionalized using the following parameters

$$\bar{x}_k = \frac{x_k}{L} \quad \bar{v}_k = \frac{v_k}{U_\infty} \quad \bar{t} = \frac{tU_\infty}{L}$$
$$\bar{\alpha}_k = \frac{\alpha_k}{\alpha_{k,\infty}} \quad \bar{g}_i = \frac{g_i}{g_\infty} \quad \bar{a}_k = \frac{a_k L}{U_\infty^2} \qquad \textbf{Eq. 2-23}$$

The over-bars $\left(^{-}\right)$ will be omitted from now on, and all parameters will be considered to be non-dimensional unless otherwise specified. The non-dimensional forms of the mass and momentum equations are

Mass Conservation

$$\frac{\partial\left(\alpha_p\right)}{\partial t} + \frac{\partial\left(\alpha_p v_j\right)}{\partial x_j} = 0 \qquad \textbf{Eq. 2-24}$$

Momentum Conservation

$$\frac{\partial\left(\alpha_p v_i\right)}{\partial t} + \frac{\partial\left(\alpha_p v_j v_i\right)}{\partial x_j} = \alpha_p\left[\frac{1}{Fr^2}\left(1-\frac{\rho_a}{\rho_p}\right)g_i + \frac{C_d\,\mathrm{Re}_p}{4K_p}\left(v_{a,i}-v_i\right)\right] \qquad \textbf{Eq. 2-25}$$

Where the Froude number, Fr, is defined as

$$Fr = \frac{U_\infty}{\sqrt{Lg}} \qquad \textbf{Eq. 2-26}$$

When the equations are expressed in their non-dimensional form, the inertia parameter, K_p, can be defined for droplets, K_d, and crystals, K_{ic}, as

$$K_d = \frac{U_\infty \rho_d d_d^2}{3\mu_a L} \qquad \textbf{Eq. 2-27}$$

$$K_{ic} = \frac{U_\infty \rho_{ic} d_{eq}^2 E^{2/3}}{3\mu_a L} \qquad \textbf{Eq. 2-28}$$

2.4 Discretization of the Particle Governing Equations

The continuous spatial domain that defines the solution space is split up into a set of non-overlapping finite elements. Each node of the element has 4 degrees of freedom corresponding to the solution variables $\left[\alpha_p, v_1, v_2, v_3\right]$. The set of governing equations described in Eq. 2-24 and Eq. 2-25 is applied to each element in the spatial domain to yield an algebraic set of equations. The Galerkin Finite Element method is used to discretize the equations. A brief outline of the discretization procedure is provided below. The governing equations are integrated in an elemental subspace V enclosed by a boundary ζ defined as

Weighted integral of mass conservation

$$\int_V W_1 \left(\frac{\partial(\alpha_p)}{\partial t} + \frac{\partial(\alpha_p v_j)}{\partial x_j} \right) dV = 0 \qquad \textbf{Eq. 2-29}$$

Weighted integral of momentum conservation

$$\int_V W_{2i} \left(\frac{\partial(\alpha_p v_i)}{\partial t} + \frac{\partial(\alpha_p v_j v_i)}{\partial x_j} \right) dV = \int_V W_{2i} rhs^* dV \qquad \textbf{Eq. 2-30}$$

where the rhs^* refers to the right-hand side of Eq. 2-25. Integrating the convection terms $\left(i.e.\ \frac{\partial}{\partial x_j} \right)$ in Eq. 2-29 and Eq. 2-30 by parts yields the so-called 'weak' form, allowing the recovery of Neumann-type boundary conditions at the boundaries of the solution domain.

Weak form of mass conservation

$$\int_V W_1 \left(\frac{\partial(\alpha_p)}{\partial t} - \alpha_p v_j \frac{\partial W_1}{\partial x_j} \right) dV + \oint_\zeta W_1 \alpha_p v_j n_j dS = 0 \qquad \textbf{Eq. 2-31}$$

Weak form of momentum conservation

$$\int_V W_{2i} \left(\frac{\partial(\alpha_p v_i)}{\partial t} - \alpha_p v_j v_i \frac{\partial(W_{2,i})}{\partial x_j} \right) dV + \oint_\zeta W_{2i} \alpha_p v_i v_j n_j \, dS = \int_V W_{2i} rhs^* dV \qquad \textbf{Eq. 2-32}$$

All variables of interest are represented using shape functions that are defined based on the element type. For any given variable ϕ

$$\phi(x,y,z)=\sum_{k=1}^{ndperl} N_k(x_1,x_2,x_3)\phi_k \qquad \textbf{Eq. 2-33}$$

where N_k is the shape function corresponding to the local node number 'k', $ndperl$ is the number of nodes per element, and ϕ_k is the scalar value of ϕ defined at node 'k'. The time dependent equations are integrated in time increments that will be denoted by a superscript 'm'. The current time level will be denoted by a superscript 'm' and a backward Euler scheme will be used to represent the discretization for any function f in time t

$$\frac{\partial f}{\partial t}=\frac{f^m - f^{m-1}}{\Delta t} \qquad \textbf{Eq. 2-34}$$
$$\Delta t = t^m - t^{m-1}$$

In the steady state calculation, the time step term is still included, acting as a pseudo time term that helps stabilize the solution during the iterative process. To help improve convergence, the equations are linearized via a Newton method. The linearization procedure helps accelerate convergence by considering the solution of a perturbed system of the unknown variables in space. Each iteration, for a given time step, progressively drives these perturbed values to a minimum, and creates a starting point for the next solution time step. The Newton linearization of ϕ for a given spatial iteration level, defined using subscript 'n', can be expressed as

$$\phi_n^m = \phi_{n-1}^m + \Delta\phi_n^m \qquad \textbf{Eq. 2-35}$$

The discretization of the particle equations yields a linear system of equations that can be represented by a local stiffness matrix A, a set of unknowns $\Delta\phi$ and a residual R for each element in the spatial domain

$$A\Delta\phi = R$$

$$A=\begin{bmatrix} A_{1,1} & A_{1,2} & A_{1,3} & A_{1,4} \\ A_{2,1} & A_{2,2} & A_{2,3} & A_{2,4} \\ A_{3,1} & A_{3,2} & A_{3,3} & A_{3,4} \\ A_{4,1} & A_{4,2} & A_{4,3} & A_{4,4} \end{bmatrix} \quad \Delta\phi=\begin{bmatrix} \Delta\alpha_p \\ \Delta v_1 \\ \Delta v_2 \\ \Delta v_3 \end{bmatrix} \quad R=\begin{bmatrix} R_1 \\ R_2 \\ R_3 \\ R_4 \end{bmatrix}$$

Each entry $A_{i,j}$ is in-turn a sub-matrix, which is a function of the number of nodes present in each element and is of the size $[ndperl \times ndperl]$. The full set of descretized equations for mass and momentum, as well as the entries for matrix A, are provided in Appendix I. The system of equations is solved iteratively using a Generalized Minimum Residual (GMRES) iterative solver [46].

2.5 Collection Efficiency

The collection efficiency, β, is an important parameter that defines the impingement regions of the water droplets, or ice crystals, that hit a surface. The collection efficiency establishes the potential icing zone and is used to calculate the particle mass flux that accumulates as ice. The definition of β in an Eulerian approach was proposed by Bourgault *et al.* [32], and computes the normal velocity component to the surface to determine "impact". If the scalar product of the particles velocity vector, $\vec{v}_p$, and the outward pointing normal to the surface, $\vec{n}$, is negative, then by definition the particles are impacting the wall and β is calculated as follows

$$\beta = -\alpha_p \vec{v}_p \bullet \vec{n} \qquad \textbf{Eq. 2-36}$$

A negative value of β implies that water is exiting from the surface, which is not possible, and hence it is reset to zero on the surface. The advantage of using an Eulerian approach to model the collection efficiency is that it is computationally cost-effective compared to Lagrangian approaches [47], which require a large number of particles to be tracked individually. The approach can therefore be used for complex geometries, such as multi-element airfoils, with limited computational resources.

3. Ice Accretion by Ice Crystals and Water Droplets

The physics that governs ice accretion due to supercooled liquid droplets has been extensively investigated, and has a sound foundation with respect to the development of mathematical models used to closely approximate the ice shape. Little work has been done, however, to explore the contribution of ice crystals to the characteristics of ice accretion. Recent progress has been made in identifying, visually, the key factors that occur when ice crystals contribute to ice accumulation. The experimental measurements required to quantify and correlate such effects have yet to be established.

Ice crystals tend to bounce off dry unheated surfaces, or surfaces covered by rime ice. In doing so, they may erode some of the ice surface, or alternatively, splash away any existing film of water if they stick to a wetted surface [19, 30]. Such effects cause an overall reduction in the amount of ice accreted as compared to the amount of ice accreted purely due to liquid droplets. The presence of ice crystals in a mixed phase cloud is seen as being less hazardous in terms of the performance degradation caused by external airframe icing. The primary focus in investigating ice crystals dynamics, however, lies in the complex phenomena that may occur inside a jet engine.

Engine core surfaces hit by ice crystals are more likely to be above freezing point, since inlet guide vanes and splitters are often heated and the temperatures rise, as the pressure increases from one compressor stage to the next. As ice crystals pass through rotating and non-rotating components, they may collide and bounce off, breakup, or stick to heated surfaces and melt. Impacts with solid surfaces or aerodynamic loads that may cause the ice crystals to break-up into smaller particles, as well as the loss of inertia as they pass through subsequent stages of a turbomachine, coupled to the increasing probability of hitting a surface, are the dominant factors that reduce the susceptibility for further bouncing, or splashing of film, thereby increasing the chances of ice crystals contributing to ice growth inside the compressor.

3.1 Extension of the Shallow Water Icing Model

A modification of the standard icing model to account for ice accumulation due to crystals is presented here. It is based on a differential form of the Messinger model [29] of mass and energy conservation. The underlying assumptions that govern ice crystal accretion have already been mentioned in the previous chapter, however it should be noted that these assumptions have only been qualitative and have not been quantified to represent the behavior of ice crystals under various icing conditions.

The Shallow-Water-Icing model (SWIM) implemented in ICE3D has been extensively validated [24]. Three regions are defined, based on the temperature $\tilde{T}$ of the ice-water interface on the surface. These regions need to be characterized with respect to ice crystals. The following assumptions will be used to model the ice crystals behavior when in contact with the liquid film or the iced surface.

- In the rime region $\left(\tilde{T} < 0\right)$, it will be assumed that all crystals bounce off the surface. This may certainly not be the case in a creeping flow condition where crystals may settle on the iced surface, or when the crystal size is small and the impact energy is insufficient to cause a bouncing and re-injection into the flow field. The justification of not considering any contribution of ice crystals to the ice mass in this region is because, in the presence of crystals, the observed rime ice shapes obtained using experiment [30] did not vary significantly from those obtained in the absence of ice crystals. It can then be concluded that the addition or reduction in ice mass due to ice crystals, if any, is negligibly small and maybe ignored.
- In glaze $\left(\tilde{T} = 0\right)$ and water-film $\left(\tilde{T} > 0\right)$ regions, a fraction of the ice crystals that impact the surface at a given time will be assumed to stick to the surface.
- Crystals that stick to a wet surface may melt completely if the water-film contains a sufficient amount of energy, or may melt partially in the case where only a limited amount of energy is available. In the case of partial melting, considerations have to be made to address the behaviour of the un-melted crystal mass as time progresses. One possibility would be to consider the un-melted crystal mass as a separate contribution to the ice mass in the SWIM equations. Another would be to consider melting as a function of time, causing a time-dependent addition of mass to the film. These considerations however increase the mathematical complexity of the model. As a first attempt at modeling these effects, the ice crystals will be assumed to melt instantaneously when they hit a surface covered with glaze ice or a water-film.

- Crystals that bounce transfer energy to the film or ice surface through their kinetic energy change. Since ice crystal sizes are often orders of magnitude larger than the water-film thickness, a precise way to take into account a bouncing impact would be to introduce a force which displaces the film and causes it to spread. In this work however, a simplified model will be presented, in which the kinetic energy loss is taken into account as a source term in the energy equation.
- Crystals that stick can cause a fraction of the existing water-film to splash. The splashing dynamics of droplets [48], and of solid spheres [49] on a liquid surface have been already addressed in the literature. Modeling the splashing based on criteria such as size and impact velocity of a single particle, however, cannot be directly applied to the Eulerian reference frame, where bulk properties, not individual particles, are computed at grid nodes. A statistical distribution of particles for a given grid node must then be assumed, to separate particles that affect splashing from those that do not. Furthermore, the irregularity associated with ice crystal shapes complicates the splashing process, since the orientation of the impacting particles influences the direction of splashed mass around the particle. To avoid such uncertainties, splashing will be ignored in the current model.
- Secondary effects such as crystal shattering, abrasion due to bouncing, spreading of the film due to ice crystal impact will not be considered in this work.

3.1.1 <u>Conservation of Mass</u>

A mass balance equation can be written by considering the water-film control volume lying on the solid wall in Figure 3-1, where each term is represented and detailed in Table 3-1

$$\dot{m}_V + \dot{m}_F = \dot{m}_{\beta_1} + \dot{m}_{\beta_2} + \dot{m}_{evap} + \dot{m}_{ice} \qquad \textbf{Eq. 3-1}$$

The crystals that stick but do not melt, $\dot{m}_{ice,ic}$, do not contribute to the conservation of mass in the control volume around the film, however they do affect the ice shape, and therefore must be considered when generating the displaced ice shape.

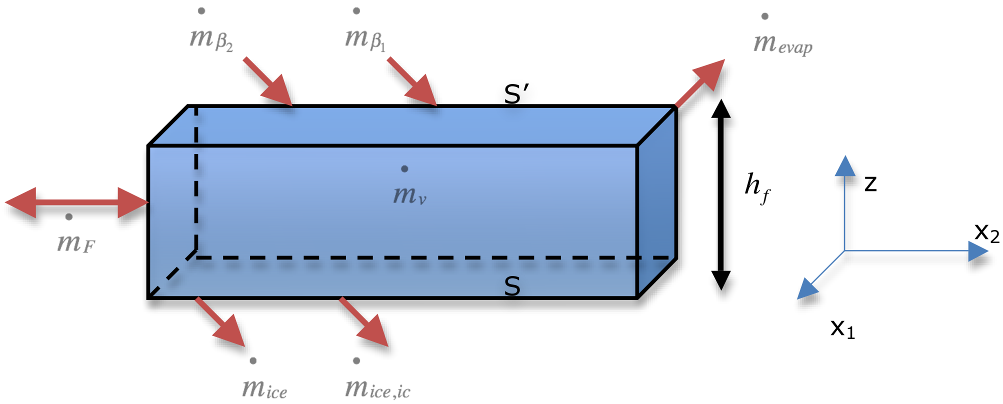

Figure 3-1 Mass conservation terms transferred across water-film interface

Description	Symbol	Formulation
Time rate of change of fluid inside *dV*	$\dot{m}_V$	$\frac{\partial}{\partial t}\int_S \int_0^{h_f} \rho_w \, dz d\vec{x}$
Net rate of flux through the control surface *dS*	$\dot{m}_F$	$\int_{\partial S} \int_0^{h_f} \rho_w \vec{v}_f \bullet \vec{n} \, dz \, dS$
Impinging water droplets	$\dot{m}_{\beta_1}$	$U_\infty LWC_\infty \int_{S'} \beta_1(\vec{x},t) d\vec{x}$
Fraction of impinging ice crystals that stick and melt	$\dot{m}_{\beta_2}$	$\alpha_{st}\alpha_m U_\infty ICC_\infty \int_{S'} \beta_2(\vec{x},t) d\vec{x}$
Evaporation/sublimation of water-film	$\dot{m}_{evap}$	$-\int_{S'} m''_{evap}(\vec{x},t) d\vec{x}$
Ice accreted from the water-film	$\dot{m}_{ice}$	$-\int_{S'} m''_{ice}(\vec{x},t) d\vec{x}$
Ice accreted due to crystals which stick but do not melt	$\dot{m}_{ice,ic}$	$\alpha_{st}(1-\alpha_m) U_\infty ICC_\infty \int_{S'} \beta_2(\vec{x},t) d\vec{x}$

Table 3-1 Terms contributing to the conservation of mass

Eq. 3-1 is an integro-differential equation that represents the instantaneous mass of the film inside the finite control volume dV

$$\frac{\partial}{\partial t}\int_{S'}\int_{0}^{h_f}\rho_w\,dz d\vec{x}+\int_{\partial S}\int_{0}^{h_f}\rho_w\vec{v}_f\bullet\vec{n}\,dz\,dS=U_\infty LWC_\infty\int_{S'}\beta_1(\vec{x},t)d\vec{x}+ \alpha_{st}\alpha_m U_\infty ICC_\infty\int_{S'}\beta_2(\vec{x},t)d\vec{x}-\int_{S'}m''_{evap}(\vec{x},t)d\vec{x}-\int_{S'}m''_{ice}(\vec{x},t)d\vec{x} \qquad \textbf{Eq. 3-2}$$

The surface S refers to the ice-film interface, and S' refers to the film-gas interface and is the normal projection of S once ice has been accreted. The distance between S' and S is indicated by h_f, the height of the film. We will assume that the integration over the upper surface S' is approximately equal to the integration over the lower surface S, since the height of the film is typically small [50]. The superscript symbol over any scalar ϕ'' is used here to indicate rates calculated per unit area. α_{st} is the fraction of impinging ice crystal mass that sticks, and α_m is the fraction that melts, contributing to the film height. Since crystals that stick are assumed to melt instantaneously, α_m is assumed to be 1 in glaze and water-film regions.

Integrating first term on the left hand side of Eq. 3-2 and applying divergence theorem to the second term yields

$$\frac{\partial}{\partial t}\int_{S'}\rho_w h_f d\vec{x}+\int_{\partial S}\int_{0}^{h_f}\nabla\bullet\left(\rho_w\vec{v}_f\right)dz d\vec{x}=U_\infty LWC_\infty\int_{S'}\beta_1(\vec{x},t)d\vec{x}+\ldots \ldots\alpha_{st}\alpha_m U_\infty ICC_\infty\int_{S'}\beta_2(\vec{x},t)d\vec{x}-\int_{S'}m''_{evap}(\vec{x},t)d\vec{x}-\int_{S'}m''_{ice}(\vec{x},t)d\vec{x} \qquad \textbf{Eq. 3-3}$$

The shear stress of the airflow, $\vec{\tau}_{wall}$, defined on S and spanning the surface coordinates $\left(x_1,x_2\right)$, is the main driving force of the film. A linear velocity profile $\vec{v}_f$ across the film is justified by considering that the film thickness h_f is less than 10 microns for typical icing simulations. It can be expressed in terms of $\vec{\tau}_{wall}$ as

$$\vec{v}_f(\vec{x},y)=\frac{y}{\mu_w}\vec{\tau}_{wall}(\vec{x}) \qquad \textbf{Eq. 3-4}$$

A linear velocity profile can be imposed across h_f, and since $\vec{\tau}_{wall}$ is supplied as an input from the airflow solution

$$\bar{\vec{v}}_f(\vec{x},y)=\frac{1}{h_f}\int_0^{h_f}\vec{v}_f(\vec{x},y)\,dz=\frac{h_f}{2\mu_w}\vec{\tau}_{wall}(\vec{x}) \qquad \textbf{Eq. 3-5}$$

Eq. 3-5 is then substituted into Eq. 3-3, and all terms are brought inside the integral signs to give

$$\int_{S'} \frac{\partial}{\partial t}\left(\rho_w h_f\right) + \nabla \bullet \left(\rho_w h_f \bar{\vec{v}}_f\right) d\vec{x} = \int_{S'} U_\infty LWC_\infty \beta_1(\vec{x},t) + \alpha_{st}\alpha_m U_\infty ICC_\infty \beta_2(\vec{x},t) - m''_{evap}(\vec{x},t) - m''_{ice}(\vec{x},t) d\vec{x} \quad \textbf{Eq. 3-6}$$

The final form of the mass conservation equation can be expressed as follows

$$\rho_w\left[\frac{\partial h_f}{\partial t} + \vec{\nabla}\cdot\left(h_f \bar{\vec{v}}_f\right)\right] = S_M \quad \textbf{Eq. 3-7}$$

$$S_M = U_\infty LWC_\infty \beta_1(\vec{x},t) + \alpha_{st}\alpha_m U_\infty ICC_\infty \beta_2(\vec{x},t) - m''_{evap}(\vec{x},t) - m''_{ice}(\vec{x},t)$$

3.1.2 Conservation of Energy

An energy balance using the terms from Table 3-2 can be formulated by considering the transfer processes seen in Figure 3-2

$$\dot{Q}_V + \dot{Q}_F = \dot{Q}_{\beta_1} + \dot{Q}_{\beta_2} + \dot{Q}_{evap} + \dot{Q}_{ice} + \dot{Q}_{fus} + \dot{Q}_{conv} + \dot{Q}_{rad} + \dot{Q}_{loss} \quad \textbf{Eq. 3-8}$$

Temperature variations along the z axis are negligible, and therefore $\tilde{T}$ is constant when integrating in this coordinate direction.

Ice usually isn't perfectly smooth, and it is sometimes possible to observe ice beads separated by liquid water. In such cases a fraction of ice may sublimate and another fraction of liquid water may evaporate. Following Hedde [51], half of the water is considered liquid and the other half solid when evaporation/sublimation occurs; the split is taken into account in the term $\dot{Q}_{evap}$. The evaporative mass flux can be determined using an empirical relation determined by MacArthur [52]

$$m''_{evap} = \frac{0.7c_h}{c_{p,air}}\left[\frac{P_{v,p}(T) - H_{r,\infty}P_{v,\infty}}{P_{wall}}\right] \quad \textbf{Eq. 3-9}$$

$$T = \tilde{T} + T_{freez,ref}[K]$$

The saturation vapor pressure at the wall surface, $P_{v,p}$, is calculated from an approximation of the steam table values given as a function of temperature

$$P_{v,p} = 3386\left[0.0039 + 6.8096.10^{-6}\hat{T}^2 + 3.5579.10^{-7}\hat{T}^3\right] \quad \textbf{Eq. 3-10}$$

$$\hat{T} = 72 + 1.8T$$

The convective heat transfer is determined by using values of convective heat flux $q''_{a,conv}$ from a given airflow solution. Given an initial temperature, $\tilde{T}_{init}$ on the wall (which is a function of the boundary layer thickness and above the adiabatic temperature $T_{adiabatic}$), the convective heat transfer coefficient, c_h, can be determined.

$$c_h = \frac{q''_{a,conv}}{(\tilde{T}_{init} - T_{adiabatic})} \quad \textbf{Eq. 3-11}$$

where $T_{adiabatic}$ is the adiabatic recovery temperature [53]. By using fixed values of the c_h, the convective heat flux, q''_{conv}, that is then lost from the surface is calculated by considering the film/ice temperature, $\tilde{T}$ that is calculated in ICE3D and evolves at every time step

$$q''_{conv} = c_h(\tilde{T} - T_{adiabatic}) \quad \textbf{Eq. 3-12}$$

$\dot{Q}_F$ in Eq. 3-8, can be simplified by virtue of the divergence theorem and Eq. 3-5, to give the following integral form of the energy balance

$$\begin{aligned}
&\frac{\partial}{\partial t}\int_{S'} \rho_w c_{p,w} \tilde{T}(\vec{x},t) h_f d\vec{x} + \int_{S} \nabla \bullet \left(\rho_w c_{p,w} \tilde{T}(\vec{x},t) h_f \bar{\vec{v}}_f\right) d\vec{x} = \\
&U_\infty LWC_\infty \int_{S'} \beta_1(\vec{x},t) \left[c_{p,w}(T_{\infty,d} - \tilde{T}(\vec{x},t)) + \frac{\left\|\vec{v}_d\right\|^2}{2} \right] d\vec{x} + \int_{S'} \frac{1}{2} m''_{evap}(\vec{x},t)\left[L_{evap} + L_{sub}\right] d\vec{x} \\
&\int_{S'} m''_{ice}(\vec{x},t)\left(L_{fus} - c_{p,ice}\tilde{T}(\vec{x},t)\right) d\vec{x} + \sigma\varepsilon \int_{S} \left(T_\infty^4 - \left(\tilde{T}(\vec{x},t) + T_{freeze,ref}\right)^4\right) d\vec{x} + \\
&\alpha_{st}\alpha_m U_\infty ICC_\infty \int_{S'} \beta_2(\vec{x},t) \left[c_{p,w} T_{\infty,ic} + \frac{\left\|\vec{v}_{ic}\right\|^2}{2} - L_{fus} \right] d\vec{x} - \int_{S'} c_h(\tilde{T} - T_{adiabatic}) d\vec{x} + \int_{S'} q''_{loss} d\vec{x}
\end{aligned} \quad \textbf{Eq. 3-13}$$

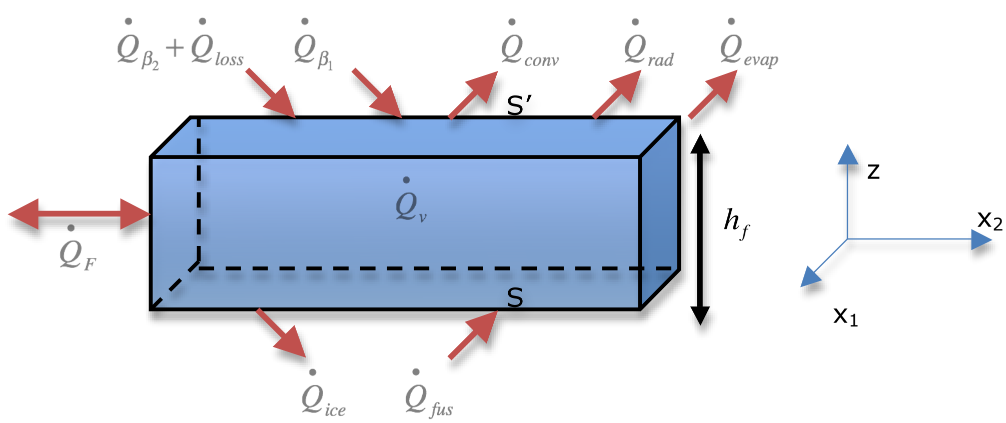

Figure 3-2 Energy conservation terms across the water-film interface

Description	Symbol	Formulation
Time rate of energy inside the *dV*	$\dot{Q}_V$	$\frac{\partial}{\partial t}\int_{S'}\int_0^{h_f}\rho_w c_{p,w}\tilde{T}(\vec{x},t)\,dz\,d\vec{x}$
Net Rate of energy transferred through the control surface *dS*	$\dot{Q}_F$	$\int_{\partial S}\int_0^{h_f}\rho_w c_{p,w}\tilde{T}(\vec{x},t)\vec{v}_f \bullet \vec{n}\,dz\,dS$
Energy transferred by droplet impingement to the *dV*	$\dot{Q}_{\beta_1}$	$U_\infty LWC_\infty\int_{S'}\beta_1(\vec{x},t)\left[c_{p,w}(T_{\infty,d}-\tilde{T}(\vec{x},t))+\frac{\lVert\vec{v}_d\rVert^2}{2}\right]d\vec{x}$
Energy transferred by a fraction of ice crystals that stick and melt to the *dV*	$\dot{Q}_{\beta_2}$	$\alpha_{st}\alpha_m U_\infty ICC_\infty\int_{S'}\beta_2(\vec{x},t)\left[c_{p,w}T_{\infty,ic}+\frac{\lVert\vec{v}_{ic}\rVert^2}{2}-L_{fus}\right]d\vec{x}$
Energy removed by evaporation/sublimation from the *dV*	$\dot{Q}_{evap}$	$-\int_{S'}\frac{1}{2}m''_{evap}(\vec{x},t)\left[L_{evap}+L_{sub}\right]d\vec{x}$
Energy transferred due to change of state into *dV*	$\dot{Q}_{fus}$	$\int_{S'}m''_{ice}(\vec{x},t)L_{fus}\,d\vec{x}$
Energy removed by ice from *dV*	$\dot{Q}_{ice}$	$-\int_{S'}m''_{ice}(\vec{x},t)c_{p,ice}\tilde{T}(\vec{x},t)\,d\vec{x}$
Energy lost due to advection (convection)	$\dot{Q}_{conv}$	$\int_{S'}q''_{conv}\,d\vec{x}$
Energy lost by radiative transfer from the *dV*	$\dot{Q}_{rad}$	$\sigma\varepsilon\int_S\left(T_\infty^4-\left(\tilde{T}(\vec{x},t)+T_{freeze,ref}\right)\right)d\vec{x}$
Energy transferred by bouncing crystals due to kinetic energy losses	$\dot{Q}_{loss}$	$\int_{S'}q''_{loss}\,d\vec{x}$

Table 3-2 Terms contributing to the energy equation

The differential form of the energy equation then reads

$$\rho_w \left[\frac{\partial h_f c_{p,w} \tilde{T}}{\partial t} + \vec{\nabla} \cdot \left(\bar{\vec{v}}_f h_f c_{p,w} \tilde{T} \right) \right] = S_E$$

$$\begin{aligned} S_E = U_\infty LWC_\infty \beta_1 & \left[c_{p,w} \left(T_{\infty,d} - \tilde{T} \right) + \frac{\left\| \vec{v}_d \right\|^2}{2} \right] - 0.5 m''_{evap} \left(L_{evap} + L_{sub} \right) + \\ \alpha_{st} \alpha_m U_\infty ICC_\infty \beta_2 & \left[c_{p,w} T_{\infty,ic} + \frac{\left\| \vec{v}_{ic} \right\|^2}{2} - L_{fus} \right] + m''_{ice} \left(L_{fus} - c_{p,ice} \tilde{T} \right) + \\ & \sigma \varepsilon \left(T_\infty^4 - T^4 \right) - c_h (\tilde{T} - T_{adiabatic}) + q''_{loss} \end{aligned}$$

Eq. 3-14

The collection efficiencies for droplets β_1 and ice crystals β_2 and their respective velocities $\left(\vec{v}_d, \vec{v}_{ic} \right)$ are obtained from the extended particle impingement module in DROP3D. The terms that need to be determined are α_{st} , and the q''_{loss} contribution to the film by ice crystals that bounce.

3.2 Ice Crystal Bouncing

Ice crystals, as mentioned earlier, have been assumed to bounce off both hard rime ice surfaces as well as surfaces containing water-film. The bouncing dynamics is complex since ice crystals are irregular in shape and as a result, their post-impact behavior is an intrinsic function of the local surface properties of the particle and the impacting surface, incidence at the contact point as well as rotational velocities prior to impact. To the author’s best knowledge, no experimental data exist that quantify bouncing properties of ice crystals on wetted surfaces. In an attempt to represent such phenomena in the present icing model, a study of available literature on the collision properties of spherical particles was pursued to establish a criterion for bounce. Assuming that the bouncing criterion is satisfied, the loss in kinetic energy transferred to the impacting surface by the bouncing particle must also be determined as an energy contribution to the film.

The contact between two dry solid bodies has been studied extensively and is often described by the Hertzian contact law [54], which assumes that the collisions are perfectly elastic with zero energy losses. In that case, the coefficient of dry restitution, defining the rebound to initial impact velocity is equal to one. However, the coefficient of dry restitution is typically found to be less than one, owing to plastic deformation in the solids, vibrations or adhesive forces at the contact interface. In typical glaze icing regions on the blade surface, or when the temperature of the impacted surface is high, the existence of a water-film is assumed to act as a collection zone for ice crystals. Not all ice crystals stick to the water-film and so a collision theory, which establishes a bouncing criterion based on impact on wetted surfaces, has to be explored.

The bouncing of particles on wetted surfaces can be described in terms of a viscous dissipation in the fluid during impact [55]. As the particle hits a wetted surface, kinetic energy is converted to internal strain energy and viscous losses in the fluid. If the internal energy is high enough it is restored to kinetic energy causing the particle to bounce. As a first approximation, the elasto-hydrodynamic theory of Davis, Serayssol and Hinch [56] is proposed. The theory states that bouncing is mainly due to the normal component of velocity, which decreases substantially compared to the changes in tangential and rotational components. The film on the surface acts as a lubricant and reduces the tangential frictional forces compared to a rough, dry surface. The relevant parameter that quantifies bouncing is identified by Davis *et al.* [57] as the Stokes number St_p, which characterizes spherical particles inertia with respect to the viscous forces

$$St_p = \frac{2 m_p v_n}{3\pi\mu_f d_p^2} \qquad \textbf{Eq. 3-15}$$

Where v_n is the normal impact velocity component of the particle with the surface and $m_p = \pi\rho_p d_p^3 / 6$ is the particle mass. For ice crystals, the equivalent volumetric diameter, d_{eq} in Eq. 2-2 is used.

A critical Stokes number, St_p, that determines a lower threshold for bounce is defined based on an elasticity parameter η that quantifies the ratio of viscous forces that cause deformation to the stiffness of the impacting solids to resist deformation

$$\eta = \frac{4\theta\mu_f v_n \left(\frac{d_p}{2}\right)^2}{x_0^{5/2}} \qquad \theta = \frac{1-\gamma_{surf}^2}{\lambda_{surf}} + \frac{1-\gamma_p^2}{\lambda_p} \qquad \textbf{Eq. 3-16}$$

θ is a coefficient that depends on the material properties of the particle and impacting surface. It is defined in terms of Poisson's ratios, γ, and moduli of elasticity, λ, defined for the surface and particle respectively. The initial separation of the particle from the opposing surface is estimated as $x_0 = 2h_f/3$ to account for sufficient penetration of the particle into the film, such that lubrication forces become important enough when considering a wetted collision [58].

$$St_c = 0.4\ln\left(\frac{1}{\eta}\right) - 0.2 \qquad \textbf{Eq. 3-17}$$

The coefficient of normal wet restitution, which can be used to quantify the losses to the lubricated surface, can be expressed as

$$\begin{aligned} e_{wet} &= e_{dry}\left(1 - \frac{St_c}{St_p}\right) & St_p > St_c \\ e_{wet} &= 0 & St_p \le St_c \end{aligned} \qquad \textbf{Eq. 3-18}$$

However, contact of the tips of roughness elements on the surface of the particle could cause bouncing to take place more easily, resulting in a reduced lubrication loss. The applicability of this formulation will now be discussed. For the application of in-flight icing, the bouncing criterion is always satisfied due to high impact velocities and the low viscosity of the water-film. Furthermore, it is only applicable to a single particle. The current implementation in ICE3D attributes an average velocity and ice crystal concentration to each node on the solid surface, and represents a set of particles and not a single particle. Such a representation leads to the conclusion that while the average velocity, which is representative of all particles within the given control volume, may satisfy the bouncing criterion, it may not be valid to assume that the entire concentration of particles bounce from the surface, since the distribution of individual particle velocities about the average velocity is not known and can only be assumed using statistical methods.

Based on this discussion, and recognizing that high velocity impacts, thin films and large particle sizes help promote bouncing, a proof-of-concept model was developed to represent the fraction of crystals that stick at a given node in the glaze regions

$$\alpha_{st} = \frac{h_f}{\max(h_f)} \frac{1}{\exp\left(\chi \left\|\vec{v}_n\right\|^2\right)} \qquad \textbf{Eq. 3-19}$$

α_{st} is assumed to be linearly proportional to the ratio of h_f and maximum film height calculated, and inversely proportional to the normal impact velocity, v_n. This corresponds to a normalized amplitude, which varies between 0 and 1. The parameter χ controls the horizontal extent of the curve, as shown in Figure 3-3, and defines an extreme limit, v_c, beyond which no crystals stick.

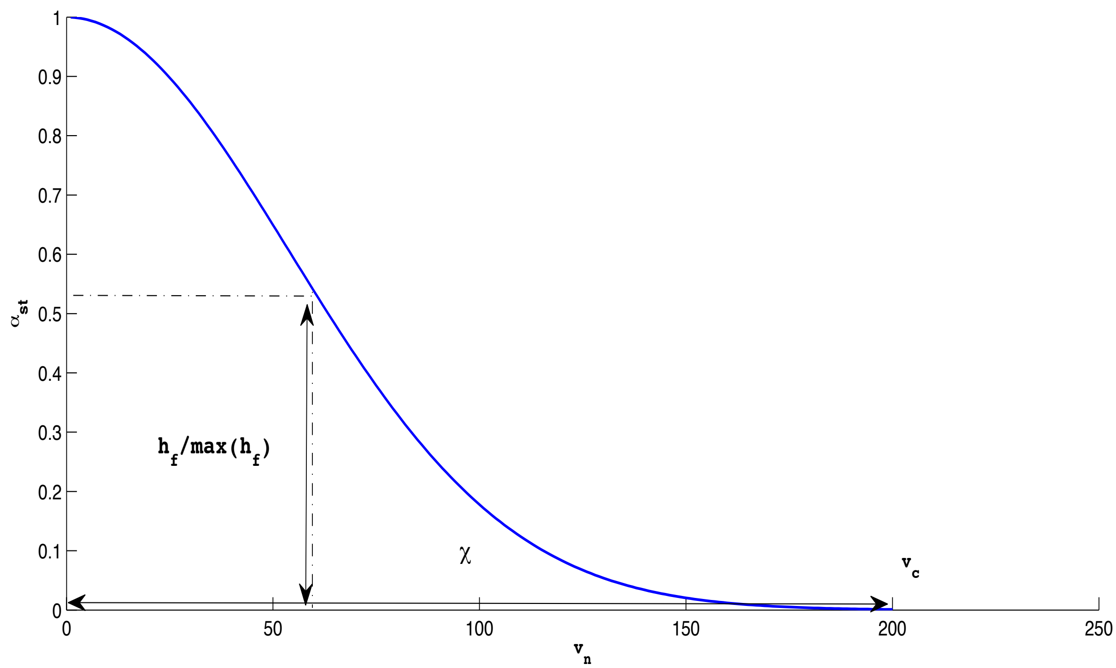

Figure 3-3 Relationship between ice crystal sticking fraction and impact velocity component v_n

Owing to the lack of experimental data to quantify a suitable threshold for v_c, the shattering of hail-like particles was considered [18]. It is therefore assumed that for any given normal velocity, v_n below v_c, some particles may bounce while others stick. All particles that exceed v_c are assumed to bounce without sticking, and is defined as

$$v_c = \sqrt{\frac{2}{d_p}} \qquad \textbf{Eq. 3-20}$$

Given that $\alpha_{st} = \psi$, where ψ is a very small number, and $h_f = \max(h_f)$, Eq. 3-19 can be rearranged to define a value for χ which determines the x-axis range of the graph in Figure 3-3

$$\chi = \frac{1}{v_c^2} \ln\left(\frac{1}{\psi}\right) \qquad \textbf{Eq. 3-21}$$

In water-film regions all crystals are assumed to stick $(\alpha_{st} = 1)$, and in the rime regions, all crystals are assumed to bounce $(\alpha_{st} = 0)$. The kinetic energy lost to the film, q''_{loss}, is calculated by first expressing the ice crystal impact velocity, $\vec{v}_{ic}$, in terms of normal $\left(\vec{e}_n\right)$ and tangential $\left(\vec{e}_t\right)$ coordinates to the surface. The coefficient of restitution, e_{wet}, calculated in Eq. 3-18, is used to determine the post-impact velocity $\vec{v}_{ic,impact}$, from which q''_{loss} is determined

$$\begin{aligned} &\vec{v}_{ic} = v_n\vec{e}_n + v_t\vec{e}_t + v_z\vec{e}_z \\ &v_{n,impact} = e_{wet}v_n \\ &\vec{v}_{ic,impact} = v_{n,impact}\vec{e}_n + v_t\vec{e}_t + v_z\vec{e}_z \\ &q''_{loss} = 0.5U_\infty ICC_\infty\beta_2\left(1-\alpha_{st}\right)\left[\left\|\vec{v}_{ic}\right\|^2 - \left\|\vec{v}_{ic,impact}\right\|^2\right] \end{aligned}$$

Eq. 3-22

3.3 Numerical Discretization of SWIM Equations

The mass and energy equations can be recast in the classical conservation form, as expressed in Eq. 3-24. The equations in ICE3D are discretized using a control volume method. The values of the parameters required from FENSAP and DROP3D are transferred to a finite volume formulation using the notion of a dual mesh, constructed on the initial wall surface. This is done by connecting the centroids of the finite volume cells on the surface to their mid-edges, such that the nodal centroids of the resulting finite volume cell correspond to those of the finite element nodes, as shown Figure 3-4:

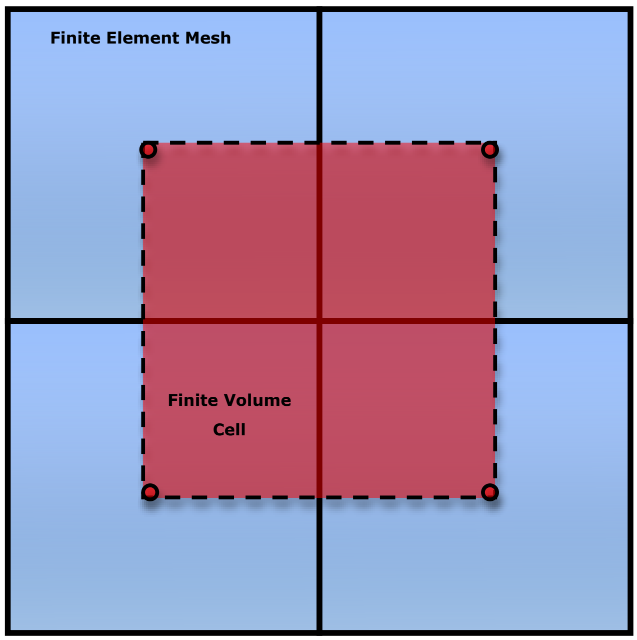

Figure 3-4 Dual mesh generated inside ICE3D from existing finite element mesh

The interface fluxes between control surfaces are computed using a Roe scheme [59], based on Godunov's method [60], which is first order accurate in both time and space. Using Eq. 3-5, the mass and energy equations in Eq. 3-7 and Eq. 3-14 can be represented as

$$\begin{aligned}
&\rho_w \left[\frac{\partial h_f}{\partial t} + \vec{\nabla} \cdot \left(\frac{h_f^2}{2\mu_f} \vec{\tau}_{wall}(\vec{x}) \right) \right] = S_M \\
&\rho_w c_{p,w} \left[\frac{\partial h_f \tilde{T}}{\partial t} + \vec{\nabla} \cdot \left(\frac{h_f}{2\mu_f} \vec{\tau}_{wall}(\vec{x}) \left\{ h_f \tilde{T} \right\} \right) \right] = S_E
\end{aligned} \qquad \textbf{Eq. 3-23}$$

The equations can be generalized by introducing a vector of unknowns, U, and a vector flux, F, as

$$\frac{\partial U}{\partial t} + \frac{\partial F}{\partial \vec{x}} = S \qquad \textbf{Eq. 3-24}$$

Where U and F are defined as

$$U = \begin{bmatrix} h_f \\ h_f \widetilde{T} \end{bmatrix} = \begin{bmatrix} \phi_1 \\ \phi_2 \end{bmatrix}$$

$$F(U) = \begin{bmatrix} \dfrac{h_f^2}{2\mu_f} \vec{\tau}_{wall} \\ \dfrac{h_f^2 \widetilde{T}}{2\mu_f} \vec{\tau}_{wall} \end{bmatrix} = \begin{bmatrix} \dfrac{\phi_1^2}{2\mu_f} \vec{\tau}_{wall} \\ \dfrac{\phi_1 \phi_2}{2\mu_f} \vec{\tau}_{wall} \end{bmatrix} \qquad \textbf{Eq. 3-25}$$

$$S = \begin{bmatrix} S_m / \rho_w \\ S_E / \rho_w c_{p,w} \end{bmatrix}$$

Average quantities for the temperature and the film height are assumed to prevail for a given control volume node 'i' within a given control volume dV. The integration over the control volume yields the conservative form of the hyperbolic set of equations

$$\int_V \left(\frac{\partial U_i}{\partial t} - S_i \right) dV + \int_V \frac{\partial F}{\partial \vec{x}} dV = 0 \qquad \textbf{Eq. 3-26}$$

The application of the divergence theorem to the gradient of the flux facilitates and restricts the computation of flux terms within the boundary of the control volume

$$\int_V \left(\frac{\partial U_i}{\partial t} - S_i \right) dV + \oint F(U) \bullet \vec{n} dS = 0 \qquad \textbf{Eq. 3-27}$$

The first term in Eq. 3-27 requires only the computation of the volume of a given cell, since the quantities are assumed to be constant within dV.

The second term requires the definition of a Roe averaged flux to compute the flux normal to the control surface of the respective control volume. Given an adjacent control volume 'j' and an edge 'K' as shown in Figure 3-5, the flux contribution from the left side (-) and right (+) sides can be expressed using a Taylor series expansion about edge 'K'

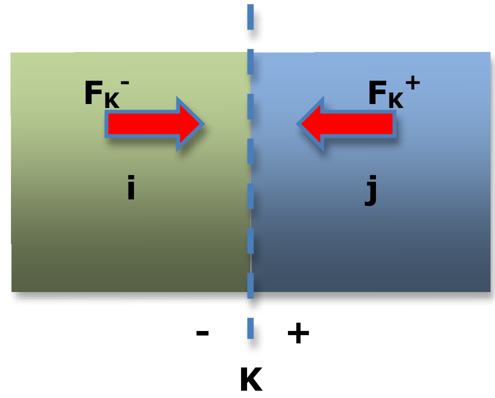

Figure 3-5 Flux contributions from left (-) and right (+) faces to a cell edge

$$F_K^- = F_i + \frac{\partial F}{\partial \vec{x}} d\vec{x} = F_i + \frac{\partial F}{\partial U}\frac{\partial U}{\partial \vec{x}} d\vec{x} = F_i + \left.\frac{\partial F}{\partial U}\right|_K dU = F_i + \left.\frac{\partial F}{\partial U}\right|_K \left(U_i - U_j\right)$$
$$F_K^+ = F_j - \frac{\partial F}{\partial \vec{x}} d\vec{x} = F_j - \frac{\partial F}{\partial U}\frac{\partial U}{\partial \vec{x}} d\vec{x} = F_j - \left.\frac{\partial F}{\partial U}\right|_K dU = F_j - \left.\frac{\partial F}{\partial U}\right|_K \left(U_i - U_j\right)$$

Eq. 3-28

The Roe-averaged flux is defined as follows

$$\Phi_{ROE} = \frac{1}{2}\left(F_i + F_j\right)\bullet\vec{n} - \frac{1}{2}\left[\left|A_{ij}\right|\bullet\vec{n}\right]\left(U_j - U_i\right)$$ **Eq. 3-29**

Where the matrix A_{ij} is the flux Jacobian matrix

$$A_{ij}\bullet\vec{n} = \begin{bmatrix} \dfrac{\partial F_1}{dU_1} & \dfrac{\partial F_1}{dU_2} \\ \dfrac{\partial F_2}{dU_1} & \dfrac{\partial F_2}{dU_2} \end{bmatrix} = \frac{\vec{\tau}_{wall}\bullet\vec{n}}{2\mu_f}\begin{bmatrix} 2\phi_1 & 0 \\ \phi_2 & \phi_1 \end{bmatrix}$$ **Eq. 3-30**

By considering the arithmetic average of quantities between nodes 'i' and 'j' the following simplification for the terms inside the matrix can be made

$$A_{ij}\bullet\vec{n} = \frac{\vec{\tau}_{wall}\bullet\vec{n}}{2\mu_f}\begin{bmatrix} 2\phi_1 & 0 \\ \phi_2 & \phi_1 \end{bmatrix} = \frac{1}{2}\left(\frac{\vec{\tau}_{wall}\bullet\vec{n}}{2\mu_f}\right)_{ij}\begin{bmatrix} \phi_{1,i} + \phi_{1,j} & 0 \\ \frac{1}{4}(\phi_{2,i} + \phi_{2,j}) & \frac{1}{4}(\phi_{1,i} + \phi_{1,j}) \end{bmatrix}$$ **Eq. 3-31**

The Roe flux can now be expressed by substitution of F and U in Eq. 3-25 into Eq. 3-29 to yield

$$\phi_{ROE,1,ij} = \frac{1}{2}\left(\frac{\vec{\tau}_{wall}\bullet\vec{n}}{2\mu_f}\right)_{ij}\left[\left(\phi_{1,i}^2+\phi_{1,j}^2\right)-\left(\phi_{1,i}+\phi_{1,j}\right)\left(\phi_{1,j}-\phi_{1,i}\right)\right]$$

$$\phi_{ROE,2,ij} = \frac{1}{2}\left(\frac{\vec{\tau}_{wall}\bullet\vec{n}}{2\mu_f}\right)_{ij}\left[\left(\phi_{1,i}\phi_{2,i}+\phi_{1,j}\phi_{2,j}\right)-\frac{1}{4}(\phi_{2,i}+\phi_{2,j})\left(\phi_{1,j}-\phi_{1,i}\right)\right.$$
$$\left.-\frac{1}{4}(\phi_{1,i}+\phi_{1,j})\left(\phi_{2,j}-\phi_{2,i}\right)\right] \qquad \textbf{Eq. 3-32}$$

The equations formed from Eq. 3-27 can be simplified to the following in mass and energy for a given set of neighbour edges 'j' surrounding node 'i'

$$\left(\rho_w\frac{\partial\phi_{1,i}}{\partial t}+m''_{ice}-\tilde{S}_{m,i}\right)V_i+\sum_j^{NE}\oint\rho_w\phi_{ROE,1,ij}\,dS=0$$
$$\left(\rho_w c_{p,w}\frac{\partial\phi_{2,i}}{\partial t}-m''_{ice}\left(L_{fus}-c_{p,ice}\tilde{T}\right)-\tilde{S}_{E,i}\right)V_i+\sum_j^{NE}\oint\rho_w c_{p,w}\phi_{ROE,2,ij}\,dS=0 \qquad \textbf{Eq. 3-33}$$

$\tilde{S}_{m,i},\tilde{S}_{E,i}$ are the source terms minus the terms containing the ice accretion rate per unit area, m''_{ice}, which is an additional unknown that must be computed, along with the film height h_f, and equilibrium surface temperature $\tilde{T}$.

3.3.1 ***Explicit Discretization in Time***

The time dependant terms in Eq. 3-33 are discretized explicitly in time such that the solution at the next time step 'n+1' is calculated using that of the previous time step, 'n'

$$\left(\rho_w\frac{\phi_{1,i}^{n+1}-\phi_{1,i}^{n}}{\Delta t}-m''^{\,n+1}_{ice}-\tilde{S}_{m,i}^{n}\right)V_i+\sum_j^{NE}\oint\rho_w\phi_{ROE,1,ij}^{n}\,dS=0$$
$$\left(\rho_w c_{p,w}\frac{\phi_{2,i}^{n+1}-\phi_{2,i}^{n}}{\Delta t}-m''^{\,n+1}_{ice}\left(L_{fus}-c_{p,ice}\tilde{T}^{n+1}\right)-\tilde{S}_{E,i}^{n}\right)V_i+\sum_j^{NE}\oint\rho_w c_{p,w}\phi_{ROE,2,ij}^{n}\,dS=0 \qquad \textbf{Eq. 3-34}$$

Please refer to Appendix 2 for details on how to compute the solution in each region.

3.3.2 ***Icing Regions and Compatibility Relations***

The icing region can be defined in terms of three regions that govern the variables h_f, $\tilde{T}$, and m''_{ice} shown in Figure 3-6.

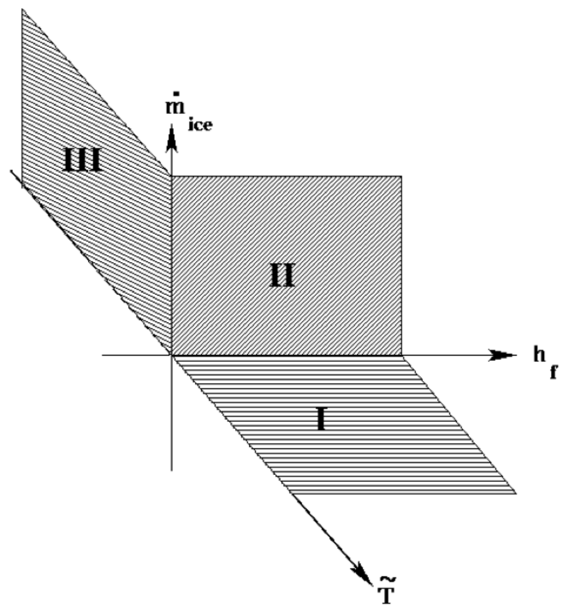

Figure 3-6 Icing planes generated by compatibility relations: I – film only, II-film and ice, III-ice only

There can be no ice above the freezing point (Region 1), and correspondingly no water-film below the freezing point (Region 3). At the freezing point, both ice and water may co-exist (Region 2). It can be seen that only two degrees of freedom are required to define a point on a plane. Given that the third variable of interest is guessed, the conservation equations can be formulated accordingly within each region to yield the required solution.

Physical solutions are ensured by the use of compatibility relations for each region. If these are not met, the procedure moves on to the next region until the relations are satisfied. The glaze ice module in ICE3D, which establishes an icing solution for each node on the surface, based on the three regions described above, is summarized in Figure 3-7.

Region 1: Liquid Film Only

This region corresponds to that containing only a liquid water-film on the surface but no ice growth. The mass of ice, m''_{ice}, is assumed to be zero and the following compatibility relations have to be satisfied to yield physically meaningful values for h_f, $\tilde{T}$

$$h_f \geq 0 \quad h_f\tilde{T} > 0$$

Region 2: Glaze Ice

This region corresponds to one in which both water-film and ice are present. The temperature $\tilde{T}$ is assumed to be zero (°C) and the following compatibility relations need to be satisfied to yield physically meaningful values for h_f, m''_{ice}

$$m''_{ice} \geq 0 \quad h_f \geq 0$$

Region 3: Rime Ice

This region corresponds to that in which only ice is present. The film height h_f is assumed to be zero and the following compatibility relations have to be satisfied in order to yield physically meaningful values for m''_{ice}, $\tilde{T}$

$$m''_{ice} \geq 0 \quad m''_{ice}\tilde{T} < 0$$

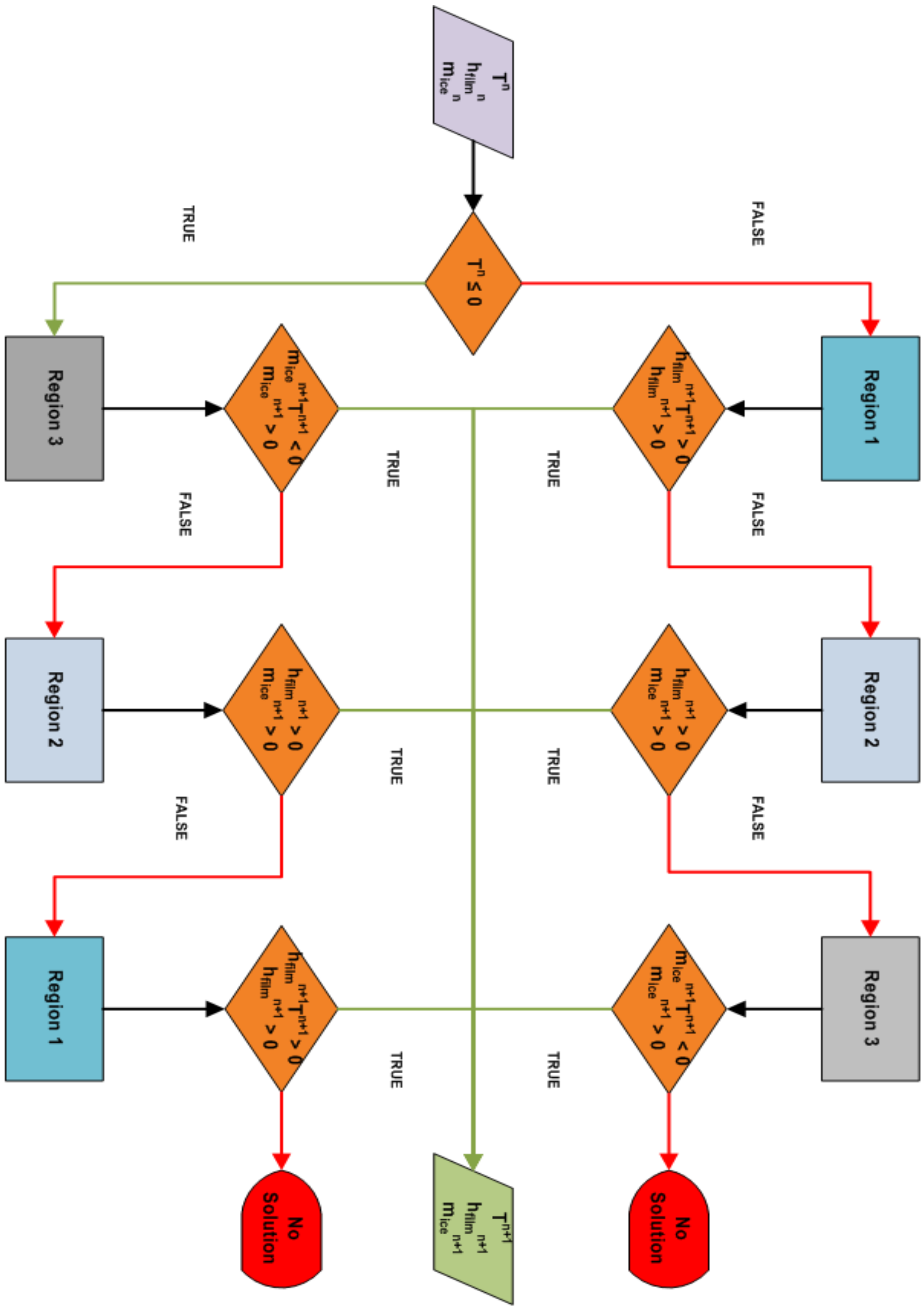

Figure 3-7 Flowchart representing solution sequence for icing model in ICE3D

4. Verification of the Code and 2D Validation

The previous chapters outlined a numerical methodology to calculate droplet and ice crystal impingement, as well as the associated impact of ice crystals on the ice accretion. The present chapter aims to verify the implementation of the ice crystal model in FENSAP-ICE, and validates it with respect to experimental data from the Cox icing tunnel tests on a NACA0012 airfoil [30], and NRC tests on an unheated non-rotating cylinder [19]. The two-dimensional ice profiles of these geometries will also be compared visually against the numerical approach of Trebor systems [22] and Lozowski mentioned in section 1.3. The differences seen in these two numerical models with respect to the experimental data will not be discussed since they are explained in the references.

4.1 Verification of DROP3D

The formulation of DROP3D has been modified to handle two particle types, namely, ice crystals and droplets, in an uncoupled manner, with no interactions between the two dispersed phases. For each iteration level, each particle type is solved sequentially in an inner loop that spans the number of active particles types in the current simulation. The libraries in DROP3D that previously contained droplet-specific routines have been modified and generalized to apply to both droplets and ice crystals. A flag inside the code establishes which particle type is being solved for, and assigns the correct properties (such as particle density, size, etc) in order to correctly define the solution space being solved for.

In order to verify this implementation and ensure that the code is working correctly, the following tests have been performed with the extended version of DROP3D, using an inviscid flow solution on a cylinder of length L=0.1014m with free-stream velocity U_∞=40m/s.

4.1.1 Uncoupled Dispersed Phase Flow

The solution of two particle types (ice crystals and droplets) at each iteration level requires the proper definition of particle related properties before solving for that particle type. But what if both particle types were identical with respect to their input properties? A sound implementation of the generalized set of routines would then yield an identical set of solutions for “ice crystals” and “droplets”, when run simultaneously. The following parameters for “droplet” and “ice crystals” were specified

Particle Type	Droplets	Ice Crystals
$LWC_{\infty} / ICC_{\infty} (g/m^3)$	1.0	1.0
$d_p (\mu m)$	20.0	20.0
E	-	1.0
$\rho_p (kg/m^3)$	1000.0	1000.0
$\left\|\vec{v}_p\right\|_{\infty} (m/s)$	40.0	40.0

Table 4-1 DROP3D parameters to verify ice crystal implementation for uncoupled multiphase flow

For the case of crystals, when E becomes unity, the major and minor axis lengths of the oblate spheroid (Figure 2-1) become equal. This results in a shape that is spherical and thus identical to that assumed for droplets. The inertia parameter K_{ic} in Eq. 2-28, then becomes equivalent to that of K_d in Eq. 3-27, and the resulting drag term for both ice crystals and droplets become equivalent, with the exception of the drag coefficient C_d. Since the crystal drag coefficient is only valid for $0.05 < E < 0.5$, the drag routine for ice crystals establishes C_d, based on that of droplets/spheres when $E = 1$.

The regions of interest when comparing the accuracy of these dispersed phase solutions are the length of the shadow zone (a region containing no particles), and the distribution of collection efficiency. The solution representing the input parameters stated above for the associated collection efficiency, and shadow zones in the wake region of the cylinder for each particle type are shown in Figure 4-1 and Figure 4-2 respectively. Identical results when comparing each of these particles ensure that the routines have been well implemented.

4.1.2 *Effect of Ice Crystal Size and Aspect Ratio*

An analysis involving geometric terms that affect the crystal inertia parameter, K_{ic}, was done to study the effect of crystal size d_{eq} and aspect ratio E on the ice crystal drag. By examining Eq. 2-28 it is expected that an increase in d_{eq} or E results in a reduction in the total drag, since K_{ic} increases. The response of the model to decreasing drag is an increase in the collection efficiency calculated on the wall surface. The higher particle Stokes number St_p associated with an increase in d_{eq} or E implies that larger particles are less sensitive to changes in the flow, and consequently take on more ballistic trajectories as they approach the wall surface.

To simulate this effect a set of ice crystal solutions was run. For runs involving variations of d_{eq}, E was kept constant at 0.5. For runs involving variations of E, d_{eq} was maintained at 100μm. The ICC_∞ was maintained at 9g/m^3. The following range of values was used

d_{eq}	40	80	120
E	0.05	0.2	0.5

Table 4-2 A range of equivalent diameters and aspect ratios used to analyze the ice crystal drag term in DROP3D

The resulting collection efficiency, β_{ic}, shown as a function of d_{eq} in Figure 4-3 and as a function of E in Figure 4-4 confirms the expectations.

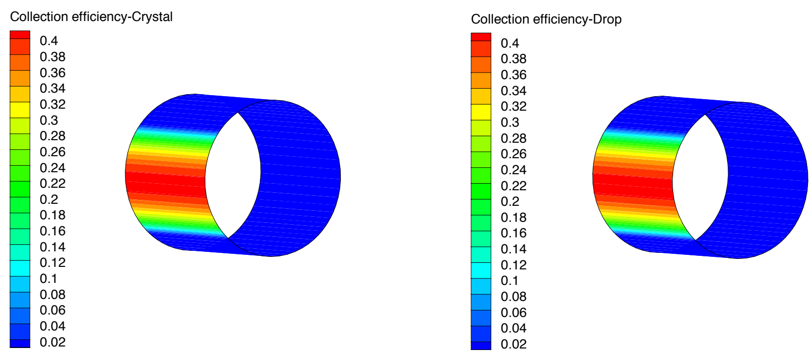

Figure 4-1 Comparison of collection efficiencies for particle types with identical properties

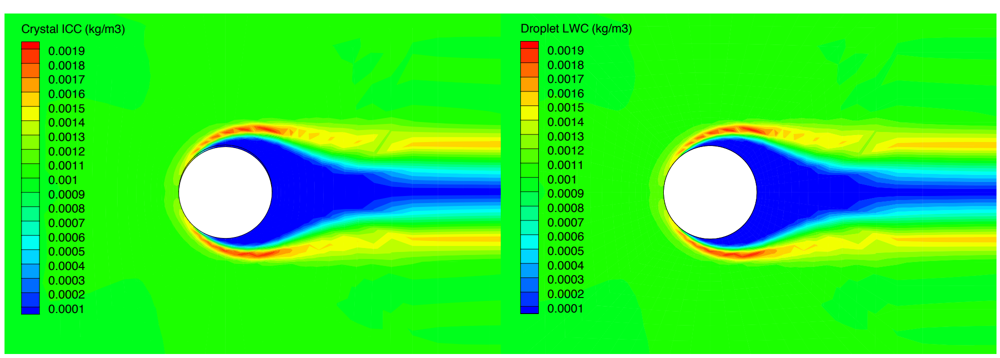

Figure 4-2 Comparison of shadow zones for particle types with identical properties

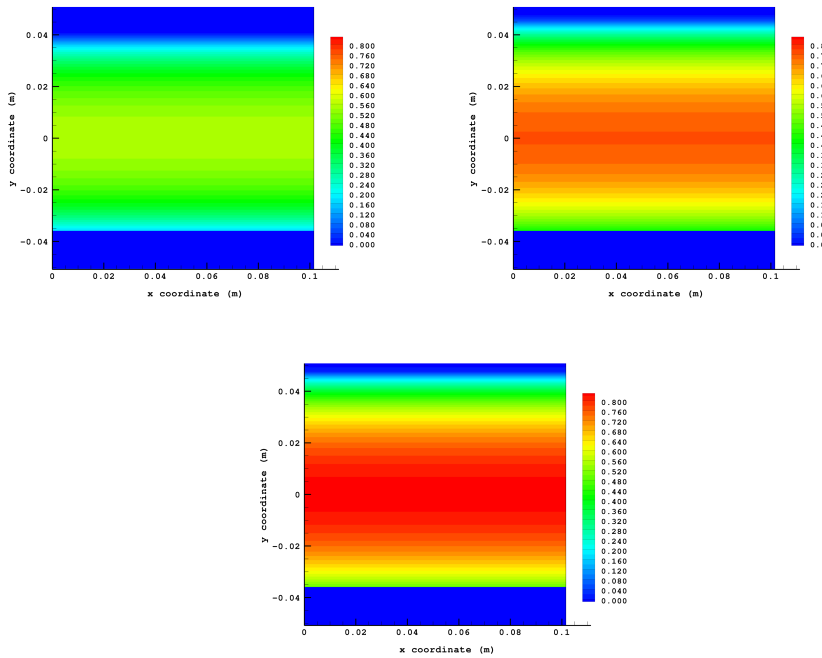

Figure 4-3 Collection efficiency comparison between ice crystal diameters of 40 (top left), 80 (top right) and 120 (bottom) microns

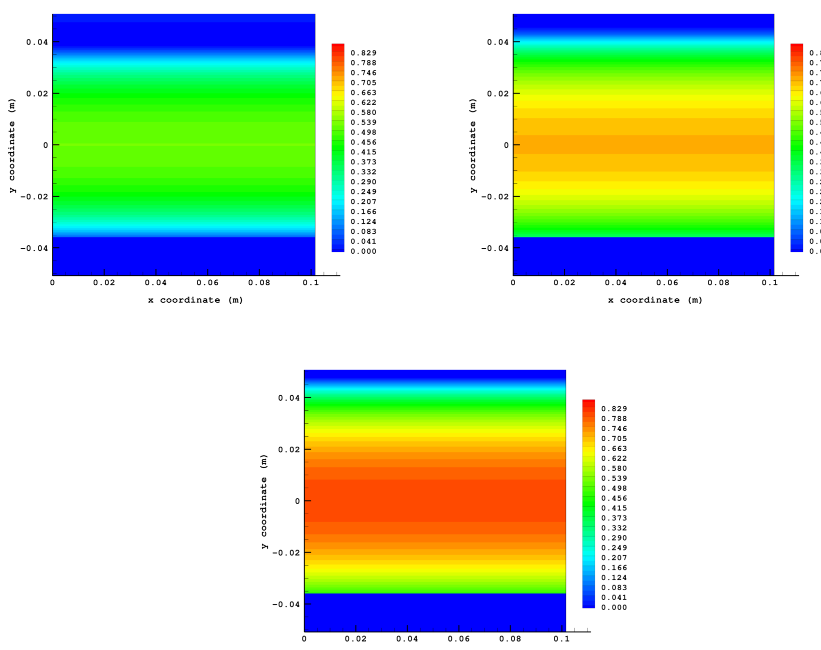

Figure 4-4 Collection efficiency comparison between ice crystal aspect ratios of 0.05 (top left), 0.2 (top right) and 0.5 (bottom)

4.2 Verification of ICE3D

Existing routines that read, write and calculate solutions for each region on the wall (as shown in Appendix 2) were generalized to allow for ice crystal variables from DROP3D to be transferred to the finite volume dual mesh in ICE3D. Additionally, introducing a source term in the mass and energy equations in ICE3D accounts for the ice crystal impingement flux on the wall. A new routine that computes the sticking fraction of ice crystals in glaze regions of the iced surface (based on the film height, ice crystal size, and their impacting velocity) was developed. The following verification procedures were carried out to ensure accurate implementation.

4.2.1 Accounting for the Ice Crystal Source Term

To ensure that the impingement flux from ice crystals has been accounted for, the present mass balance check inside ICE3D was extended to include ice crystals that contribute to ice accretion. An example taken from one of the test cases is shown in Table 4-3. The results are in accordance with the conservation of mass described in Eq. 3-1 and yield a satisfactory level of numerical accuracy.

Mass Flux Term	Value (kg)
Mass of water droplets impinging	0.352474E+00
Mass of ice crystals that stick and melt	0.126722E+00
Mass of water-film	0.908103E-04
Mass of water evaporated	0.151181E-01
Mass of ice	0.463988E+00
Mass balance	**-0.535127E-13**

Table 4-3 Mass conservation in ICE3D

4.2.2 Effect of Ice Crystal Size on the Accreted Mass of Ice

The critical velocity v_c establishes an upper threshold beyond which no ice crystals stick to the glaze region. As described by Eq. 3-20, v_c is inversely proportional to the ice crystal size. The relationship that determines the sticking fraction, α_{st}, according to the normal impact velocity v_n is shown in Figure 4-5 for different crystal sizes. The dots indicate values of v_c for a given ice crystal size. A standard test case was run to simulate the effect of the normal velocity component on the sticking fraction for different crystal sizes. For all cases, the collection efficiency was assumed constant to ensure that the resulting ice profiles were only an artifact of the mass of sticking crystals. Figure 4-6 shows the expected reduction of the ice profile as a result of increasing the ice crystal size. The effect is more pronounced at the stagnation point for any given crystal size because v_n is highest in this region.

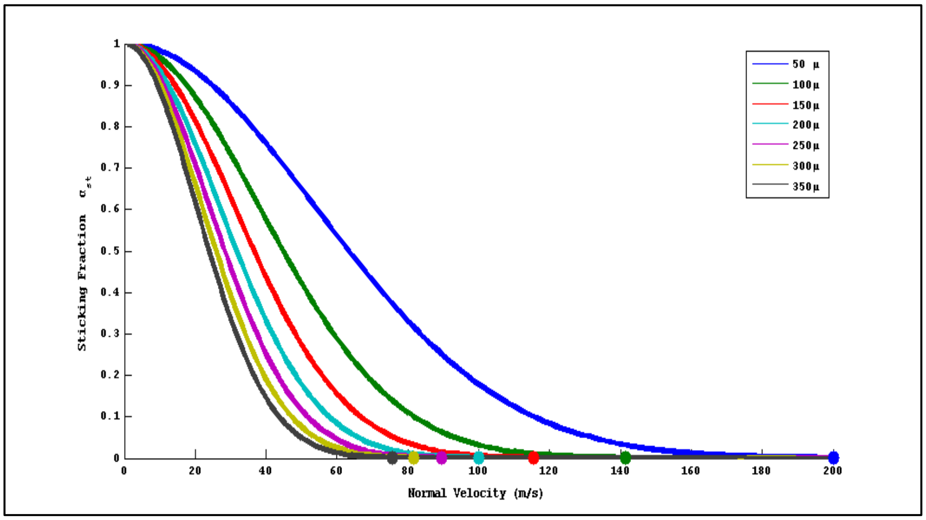

Figure 4-5 Variation of sticking fraction with ice crystal size

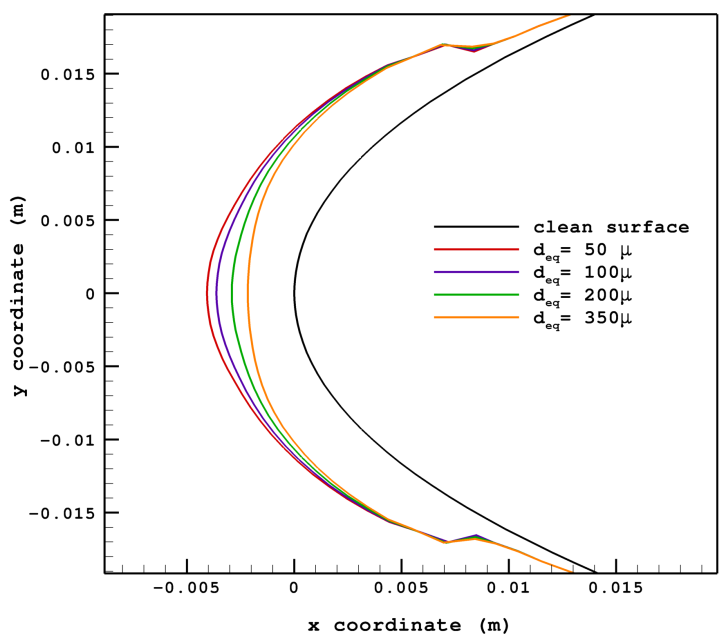

Figure 4-6 Effect of increasing crystal sizes causes more crystals to bounce and leads to a reduction in the amount of ice accreted

4.3 Cox and NRC Icing Tunnel Tests

The Cox tunnel tests were performed to analyze the capabilities of thermal anti-icing systems in mixed phase flows and were conducted on a 0.9144m chord, NACA0012 airfoil, mounted at a 0^0 angle of attack. Droplets of 20μm were produced in the tunnel using a spray bar, while ice crystals were generated either using a snow gun (i.e. involves the atomization of water droplets that freeze in the airstream) or an ice shaver (mechanically shaven ice blocks, in which particles are dispersed using a fan blower) resulting in mean ice crystals sizes of 150 and 200μm respectively. The duration of each icing test, described in Table 4-4, was 10 minutes.

NRC icing experiments carried out on an unheated non-rotating cylinder were aimed towards conducting preliminary studies towards characterizing the effects of mixed phase conditions (containing ice crystals) on helicopter blades. In this study, a Bakelite cylinder with a diameter of 0.0254m was mounted horizontally across the middle of the tunnel test section. The ice crystal environment was simulated using freshly fallen snow, to try and closely mimic the natural environment. Photographic images showed ice crystal sizes that varied from 100 to 1000μm. Droplets of 20μm were used in all experiments. The reported icing time for ice accretion was 5 minutes. Some of the experimental conditions that will be simulated are summarized in Table 4-5. Note that the cases in [] have been assigned tags for the purpose of description in this thesis, but haven't been given a unique identifier in [19]. The cases to be noted are 45CM and 47CM since they have been compared to other numerical models presented in section 1.3.

CASE	**RUN No.**	$T_\infty\ [°C]$	$U_\infty\ [m/s]$	$ICC_\infty\ [g/m^3]$	$LWC_\infty\ [g/m^3]$
3	19	-11 (Rime)	54	0.7 (snow gun)	0.3
4	20	-11 (Rime)	54	0.3 (snow gun)	0.7
15	10	-5.5 (Glaze)	54	0.7 (ice shaver)	0.7

Table 4-4 Test Conditions for Mixed Phase Ice Accretion at Cox Icing Tunnel

CASE	T_∞ [°C]	U_∞ [m/s]	ICC_∞ [g/m^3]	LWC_∞ [g/m^3]
[46CM-a]	-15	61	0.4	0.4
[46CM-b]	-15	61	0.6	1.2
47CM	-15	122	1	0.4
45CM	-5	30.5	1.2	1.2

Table 4-5 Test conditions for mixed phase ice accretion at NRC icing tunnel

4.3.1 Description of Grids for NACA0012 and Cylinder

The grid resolution is of importance, since fluctuations in heat flux and shear stress result in inaccuracies that present themselves as perturbations when generating the shape of ice through a displaced grid. A sufficiently fine grid near the wall surface also helps in order to resolve turbulence quantities, in order to ensure that these variables are sufficiently smooth on the wall surface.

A structured C-grid, shown in Figure 4-7, was generated around a NACA0012 airfoil with a mean chord length L of 0.9144 m, using 46,946 hexahedral elements. A grid resolution of 552 nodes on the wall surface ensured sufficiently smooth solutions close to the wall. The far-field boundaries were placed at 15 chord-lengths away. A structured O-grid, shown in Figure 4-8, was used to discretize the cylinder domain for the NRC test cases. The grid contains 20,800 elements concentrically distributed around the cylinder, with 280 nodes placed on the wall surface. The far-field boundaries were placed 15 chord lengths away from the centre of the cylinder. In both cases, periodicity was imposed in the span-wise direction, with one element thickness between symmetry planes.

4.3.2 Airflow Solutions using FENSAP

The airflow solution is a necessary pre-cursor that is required in order to establish particle impingement trajectories, as well as provide important parameters for ice accretion. A Reynolds Averaged Navier Stokes solution (RANS) using FENSAP is used to obtain flow variables such as the velocity flow field, $\vec{v}_a$ which is required as an input for computing particle drag in DROP3D, and the wall shear stress, $\vec{\tau}_{wall}$, and heat flux, $q''_{a,conv}$, which are required for calculating the water-film velocity, $\vec{v}_f$, and heat transfer coefficient, c_h, respectively in ICE3D.

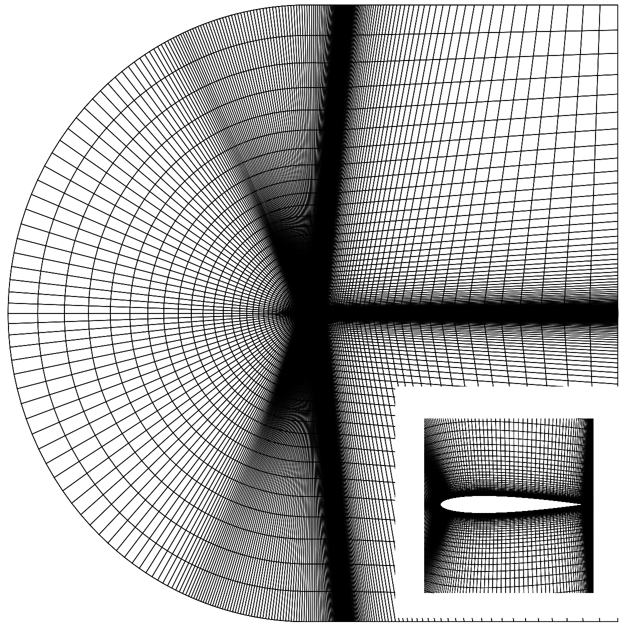

Figure 4-7 NACA0012 C-grid (main) with 552 nodes placed on the wall (bottom right inset)

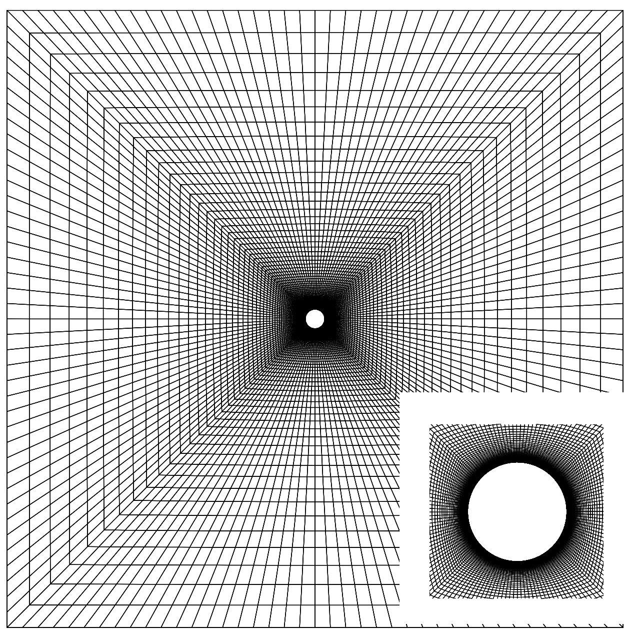

Figure 4-8 Cylinder 0-grid (main) with 280 nodes placed on the wall (bottom right inset)

4.3.2.a Turbulence Model

A one-equation Spalart Allmaras (S-A) turbulence model [61] was used in all numerical airflow simulations. The implementation of this model has been extended to handle rough walls [62], which are important in icing analysis since they influence the growth, shape and type of ice.

An 'equivalent sand grain' roughness height of 0.5 to 2mm is used as an additional input for the S-A model, that mimics the roughness in the case of an iced surface, based on popular values expressed in the literature.

Roughness on the surface is imposed by applying a non-zero turbulent eddy viscosity μ_T on the wall boundary. The effect of this is to enhance the development of a turbulent boundary layer, encourage mixing, and consequently increase the heat flux and shear stress distributions on the wall [50].

4.3.2.b Velocity Magnitudes and Streamline profiles

The velocity magnitude contours are shown in Figure 4-9, Figure 4-10, Figure 4-12, Figure 4-13, and Figure 4-14 for Cox and NRC cases respectively. The solutions for each case are symmetric, owing to the symmetric nature of the airfoil and cylinder on either side of the stagnation point.

All Cox tests were conducted at U_∞ of 54m/s. A small difference in temperatures between the cases at -11$°C$ and -5.5$°C$ does not cause any significant variation in the free-stream Reynolds number (since air viscosity does not change much), and hence the solutions in Figure 4-9 and Figure 4-10 are very similar.

The results of velocity magnitudes that were achieved by increasing Reynolds numbers (as a result of increasing free-stream velocities) for NRC 45CM, 46CM(a, b) and NRC47CM are shown in Figure 4-12, Figure 4-13 and Figure 4-14 respectively. An important aspect that needs to be noted is the presence of a symmetric set of vortices on either side of the centre-line in the cylinder-wake region, shown in Figure 4-15. The presence of these secondary flows presents a challenge when trying to establish a converged steady-state solution for dispersed phase flows involving small particle diameters (as is the case for droplets). This will be addressed in section 4.3.3.b

4.3.2.c Shear Stress and Heat Flux Distributions Over the Wall Surface

The increase in $q''_{a,conv}$ and $\vec{\tau}_{wall}$ magnitudes, as shown in Figure 4-18 and Figure 4-19, for Cox case 15 when compared to cases 3 and 4, can be explained by reviewing the input parameters for equivalent roughness height. Case 15 was run using 2mm while the other cases were run using 0.5mm. The justification for using this value in case 15 was based on an initial calibration of the icing model in the absence of ice crystals, using the following conditions

CASE	**RUN No.**	T_∞ $[°C]$	U_∞ $[m/s]$	ICC_∞ $[g/m^3]$	LWC_∞ $[g/m^3]$
14	9	-5.5 (Glaze)	54	-	0.7

Table 4-6 Test Conditions for Mixed Phase Ice Accretion at Cox Icing Tunnel

Figure 4-16 shows the model's predictions obtained using airflow solutions with roughness heights of 0.5, 1, and 2mm. Increasing the roughness height causes an increase in $q''_{a,conv}$, which translates to more energy lost through convection per unit length over the surface. This increases the icing rate and consequently moves the transition point from glaze to rime closer to the stagnation point of the airfoil. By comparisons made with experimental results, a value of 0.5mm caused too much runback ice, and resulted in a discontinuous jump from a glaze ice region to no ice formation at the impingement limits. A value of 2mm showed a much smoother transition between rime and glaze regions, and seemed to be comparable with experimental observations, such as horn-growths on either side of the stagnation point, as seen in Figure 4-17. It should be acknowledged however, that this is a crude method for calibrating roughness in the absence of experimental data, since roughness is inherently a function of time, and changes as the ice shape develops. Another important factor that has to be considered but is not accounted for, is the impact of ice crystals and their shape on the roughness height. Ice crystals have been observed to cause erosion on the ice surface, and may produce non-negligible surface variations. Experimental evidence to support such variations of roughness, however, have not yet been established and requires further investigation.

NRC test cases were run using 0.5mm for cases 45, 46 CM and 0.25mm for 47CM. The increase in $q''_{a,conv}$ and $\vec{\tau}_{wall}$ seen in Figure 4-20 and Figure 4-21, corresponds to the increase in free-stream velocity, and consequently more energy being dissipated to the wall surface boundary.

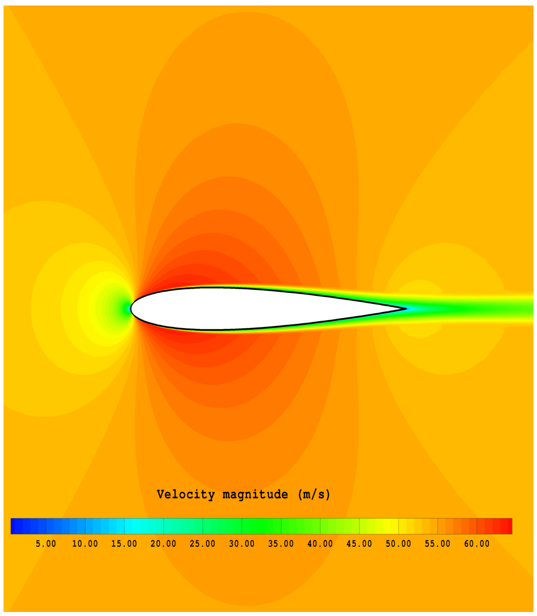

Figure 4-9 Velocity magnitude contours for Cox case 3 and 4 at Re =4.00x10^6

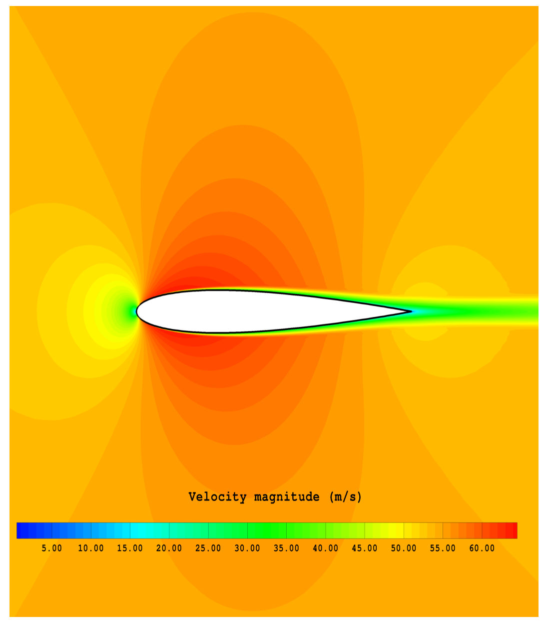

Figure 4-10 Velocity magnitude contours for Cox case 15 at Re =3.85x10^6

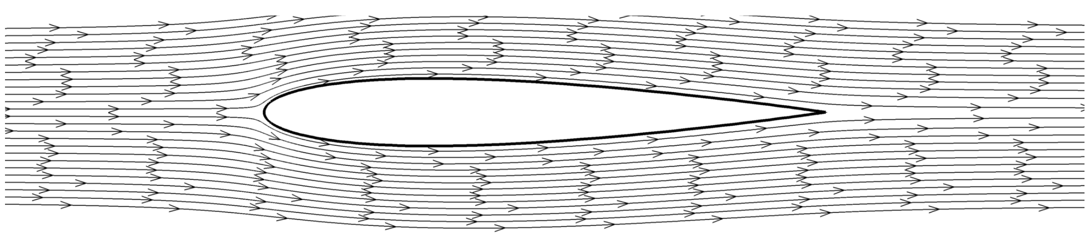

Figure 4-11 Characteristic streamline profile for NACA0012 airfoil

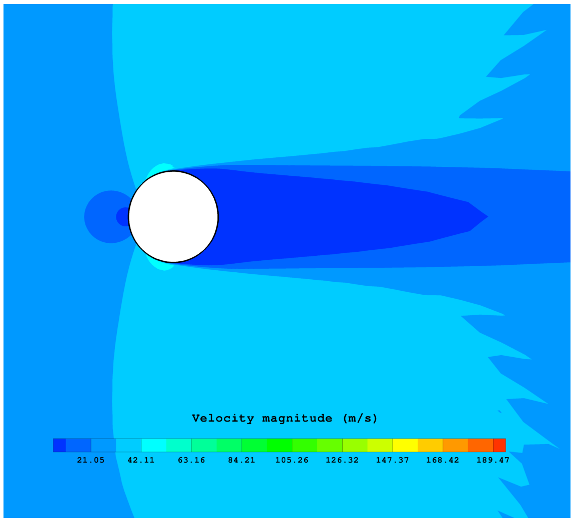

Figure 4-12 Velocity magnitude contours for NRC 45CM at Re =6.03x10^4

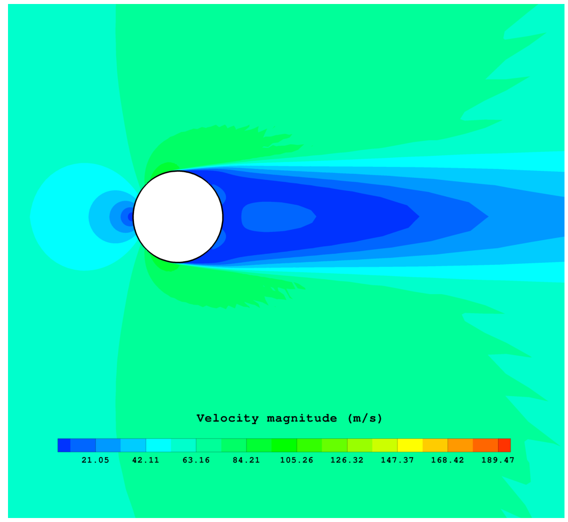

Figure 4-13 Velocity magnitude contours for NRC 46CM (a and b) at Re =1.20x10^5

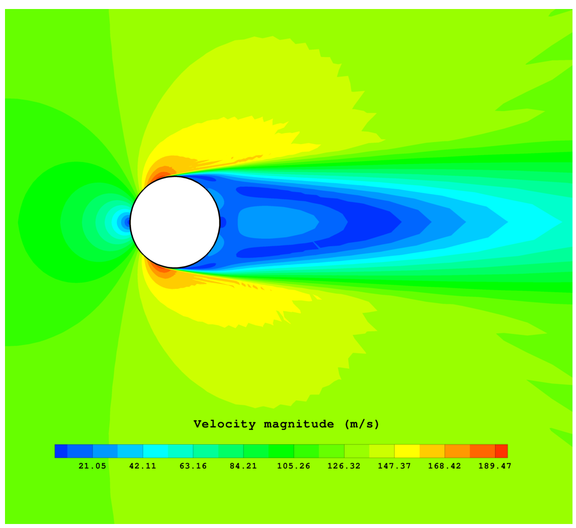

Figure 4-14 Velocity magnitude contours for NRC 47CM at Re = 2.58x10^5

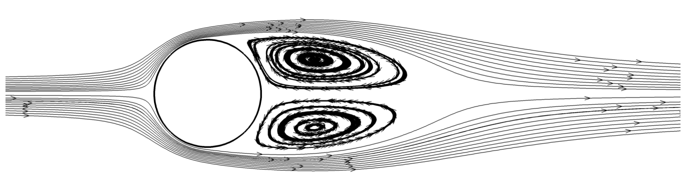

Figure 4-15 Streamline profile for cylinder with symmetric vortices in the wake region

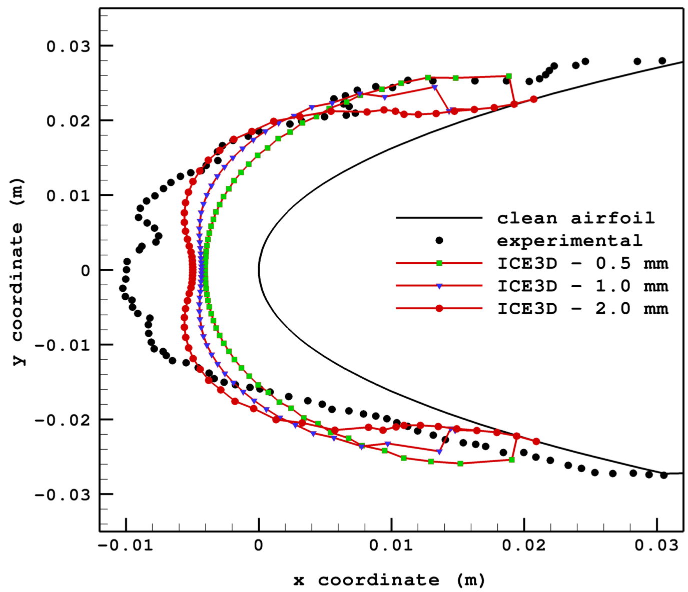

Figure 4-16 Comparison of ice shapes produced with airflow solutions of roughness heights of 0.5,1 and 2 mm against Cox case 14 experiment

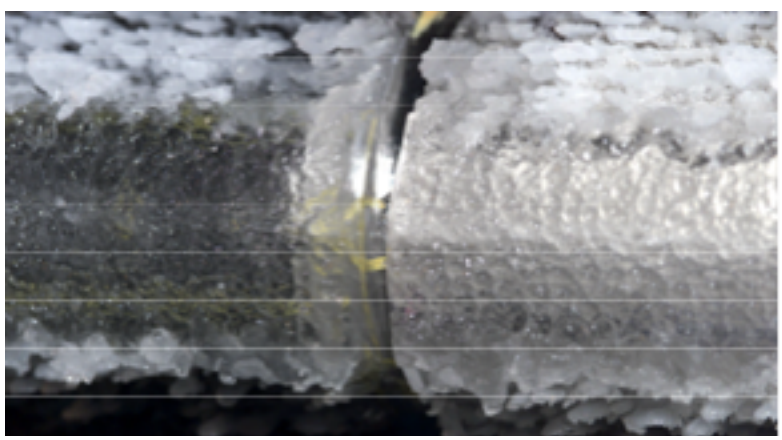

Figure 4-17 Characteristic horn-growths seen in photographs taken for Cox case 14 [30]

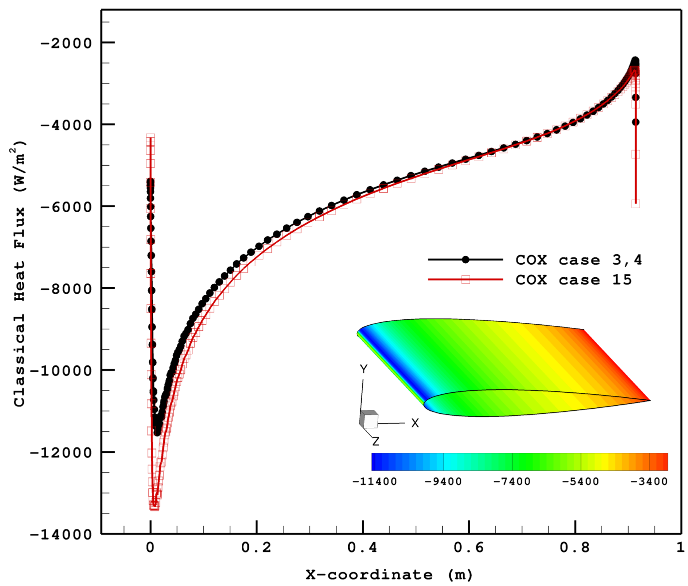

Figure 4-18 Heat flux comparison for Cox case 3,4 and 15 with distribution over airfoil for case 3,4 (lower right inset)

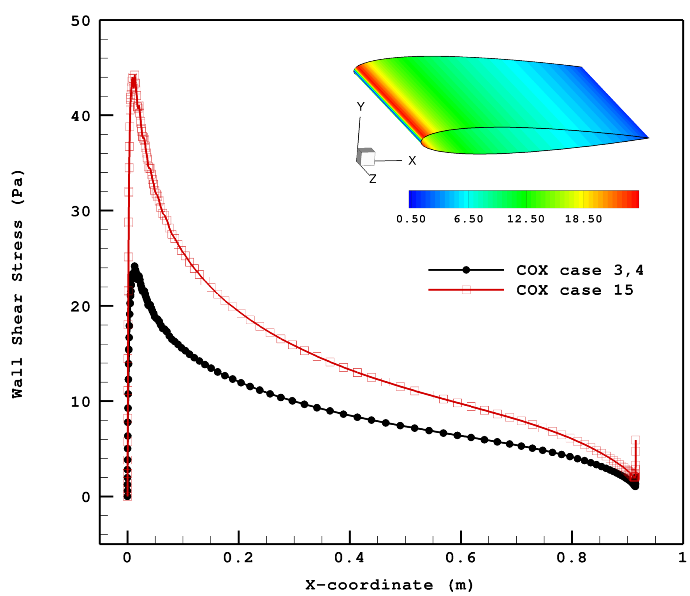

Figure 4-19 Shear stress comparison for Cox case 3,4 and 15 with distribution over airfoil for case 3,4 (upper right inset)

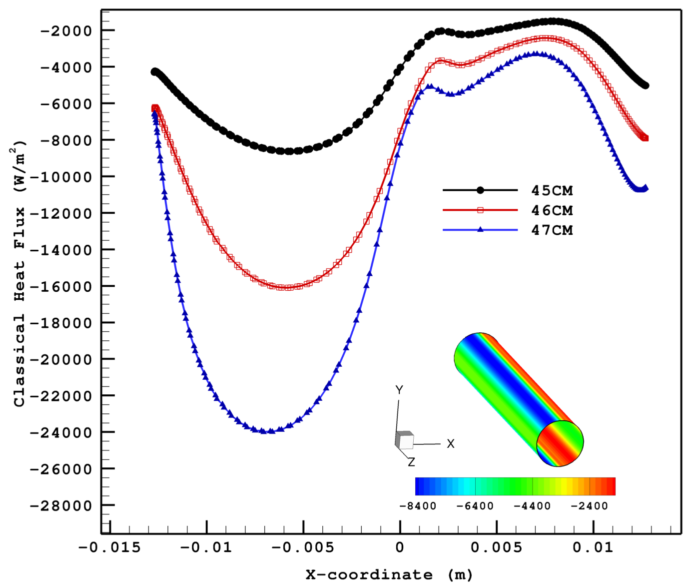

Figure 4-20 Heat flux comparison between NRC cases 45CM, 46CM and 47CM with distribution over cylinder for 45CM (lower right inset)

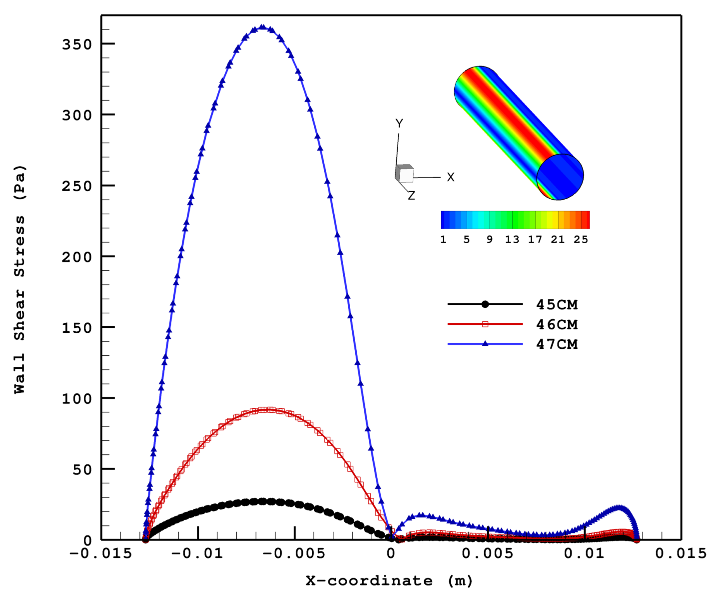

Figure 4-21 Shear stress comparison between NRC cases 45CM, 46CM and 47CM with distribution over cylinder for 45CM (upper right inset)

4.3.3 Particle Impingement Calculations

The collection efficiency is an important parameter that establishes the mass flux from droplets and ice crystals impingement, and contributes to accreting ice. The lack of experimental data (to the authors knowledge) to quantify collection efficiencies for ice crystals makes only a qualitative comparison against those of droplets possible. Observations made through high-speed cameras of ice crystals impinging on the NRC test cylinder have led to the following statement by Lozowski [19]: *"If crystals are sufficiently large, then their inertia will cause them to move in essentially straight line trajectories prior to impact."*

4.3.3.a Collection efficiency calculations for Cox and NRC experiments

While simulating the experiments to establish ice crystal and droplet impingement, an average droplet size of 20µm for both NRC and Cox test cases was used. Cox cases 3,4 were run using an ice crystal equivalent diameter of 150µm to simulate those produced by the snow gun, while case 15 was run using 200µm to simulate the ice shaver. Collection efficiency comparisons are shown in Figure 4-22. The increase in crystal size causes an increase in β_{ic}. This is due to the increase the inertia parameter K_{ic} that results in an overall reduction in drag, as explained in section 4.1.2. The collection efficiency curves for droplets overlap and remain smaller than that of ice crystals for each case, since the simulated conditions (such as droplet size and free-stream velocity) are the same.

The collection efficiency comparison for ice crystals and droplets are shown in Figure 4-23 for the NRC cases. Ice crystal sizes of 100µm were used as an input to satisfy the dilute gas particle flow condition, and continuum hypothesis for the given characteristic length (see sections 2.1.1 and 2.1.2). An increase in the collection efficiency for droplets for higher velocities is more distinct than that experienced by ice crystals for a given flow condition. Only small differences in the collection efficiency for crystals are noticed around the stagnation point since the higher St_p associated with ice crystals for any given flow condition makes them less susceptible to fluctuations in air velocities, and therefore reduces the sensitivity of the calculated collection efficiency, even when the free-stream velocity conditions have increased.

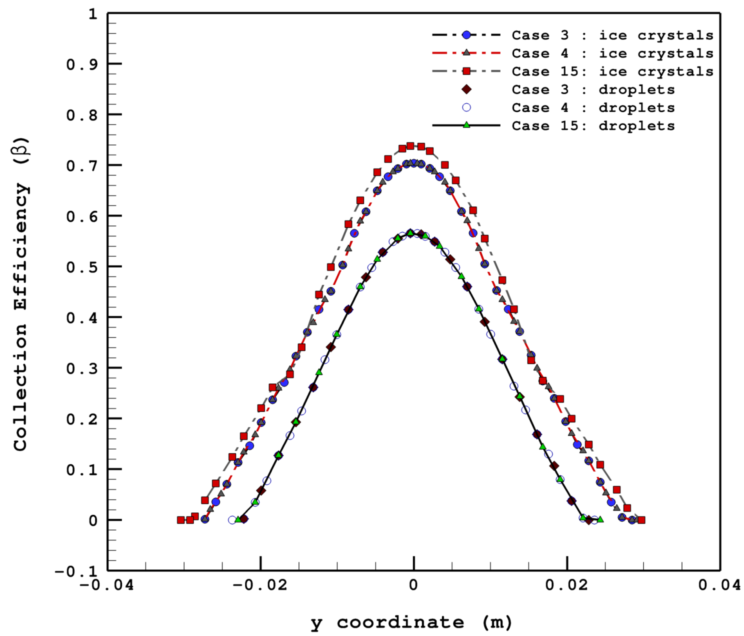

Figure 4-22 Collection efficiency comparison for Cox icing tests between droplets and ice crystals

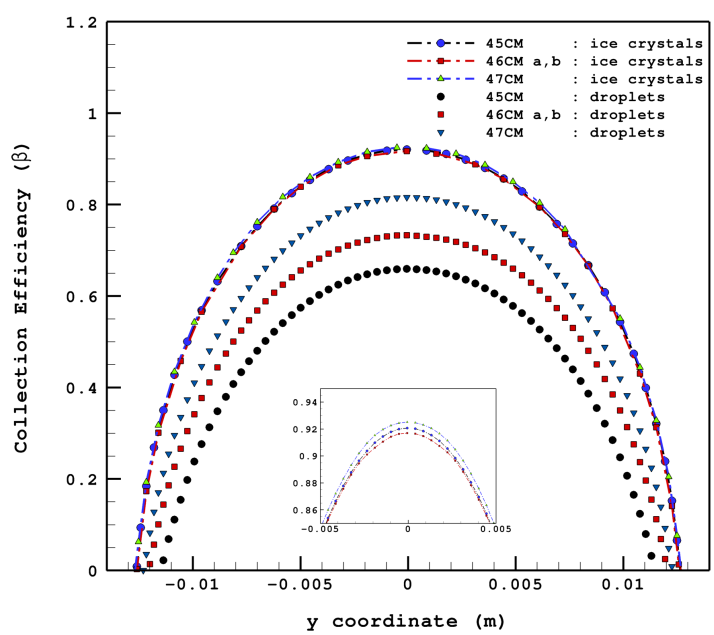

Figure 4-23 Collection efficiency comparison (main) for NRC icing tests between droplets and ice crystals, with close-up of ice crystals values near the stagnation point (inset)

4.3.3.b Stabilization of droplet solutions for NRC tests

The absence of diffusive terms in the convection-type particle equations creates convergence issues for the calculation of impingement locations for droplets, due to the presence of shedding vortices shown in Figure 4-15.

A suitable initial guess for most problems is to apply LWC_∞ and U_∞ over the entire solution domain. In the case of the cylinder however, such a guess can lead to instabilities, since the vortex caused by the airflow results in an unphysical high concentration bubble in the cylinder wake, where the solution should otherwise represent a shadow zone (i.e. no LWC).

Since air velocities drive the flow direction of the droplets, this concentration bubble starts to move towards the trailing edge of the cylinder, while a shadow zone starts to form after the wake region. The lack of any diffusion terms in the particle equations means that the concentration gradient established by the unphysical concentration bubble, and the shadow zone, is not accounted for, and causes the solution to finally diverge as iterations progress as shown in Figure 4-24.

To counteract this phenomenon, an artificial (numerical) diffusion parameter (which adds Streamlined Upwind (SU) terms to the stiffness matrix formed in Appendix 1) was initially increased from a default value of 1 to 15, to establish partial convergence and obtain a general profile of the boundaries of the shadow zone region. The solution was then stopped and restarted, using the previous solution as a new initial guess for subsequent iterations, and a smaller value of artificial diffusion. This process was repeated with lower artificial diffusion until a fully converged solution with artificial diffusion set to one was obtained.

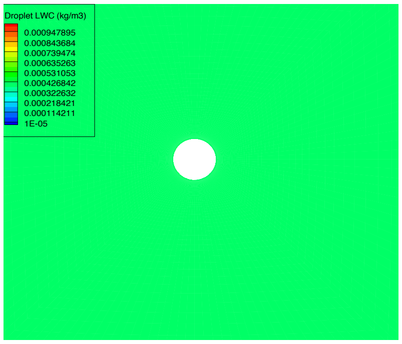

Iteration 0 (Initial solution)

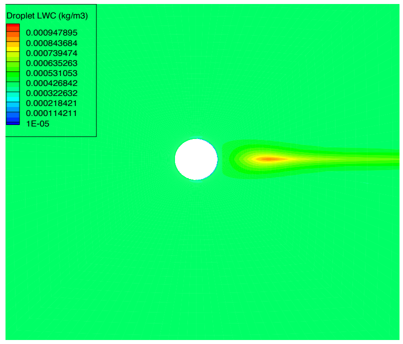

Iteration 45

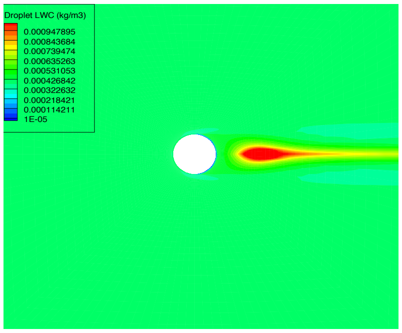

Iteration 60

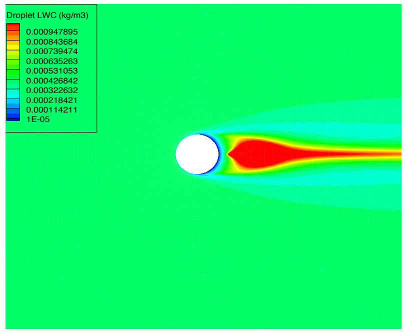

Iteration 120

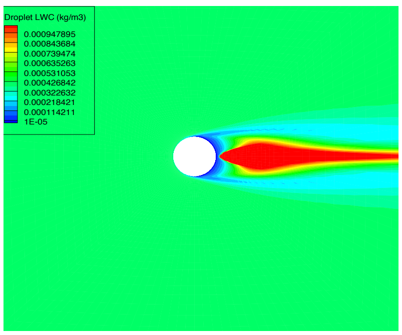

Iteration 170

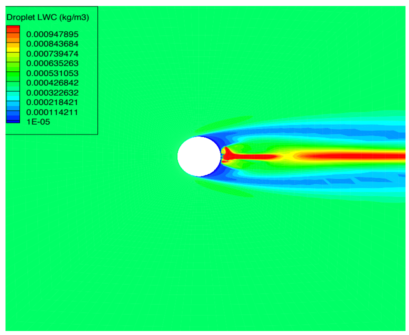

Iteration 220

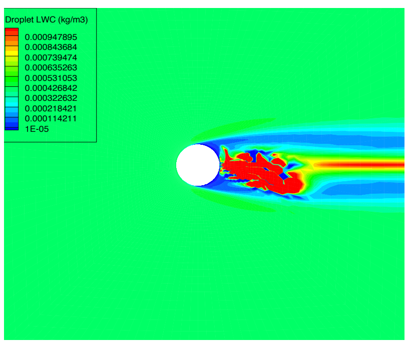

Iteraton 240 (solution diverges)

Figure 4-24 LWC around the cylinder when artificial dissipation is set to 1 initially

4.3.4 ICE3D calculations

The present section will compare experimental observations of the Cox and NRC icing tunnel tests with respect to numerical predictions made by the extended icing model in ICE3D. The shear stresses, heat fluxes and particle collection efficiencies described in 4.3.2.c and 4.3.3.a respectively are used as required input parameters for the ice accretion calculation. ICE3D is then run to obtain an ice profile, as well as a solution containing parameters such as surface temperatures, impingement mass flux, water-film height and mass of ice. The mass of ice, in particular, is an important variable with reference to analyzing icing inside turbomachines, since it is related to characterizing shedding characteristics on rotating components.

4.3.4.a Comparison with Cox experiments

The experimental ice profiles for Cox cases 3 and 4, shown in Figure 4-25 and Figure 4-27, are quite similar with respect to the shape and appearance of ice accreted. The addition of ice crystals at -11$^{\circ}C$ did not seem to greatly affect the rime-like profile, which characterizes such ice growth at this temperature. The higher concentration of ice crystals in the free-stream for case 3 did cause rime feathers seen in case 4 to disappear, and is thought to be due to erosive effects that result from high tangential impact velocities on either side of the stagnation point. The higher proportion of ice crystals in the free-stream with respect to droplets in case 3 also caused less ice to accrete (Figure 4-26).

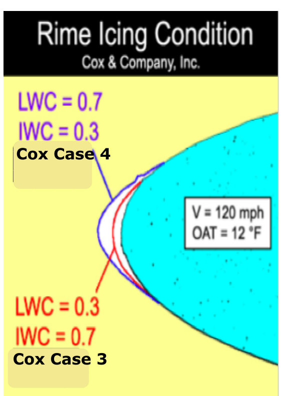

Figure 4-26 Comparison of profiles between Cox case 3 and 4

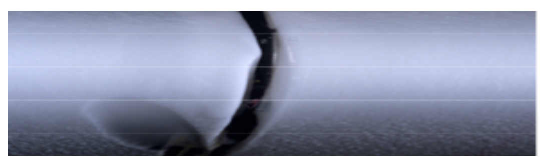

Figure 4-25 Experimental ice profile for Cox case 3

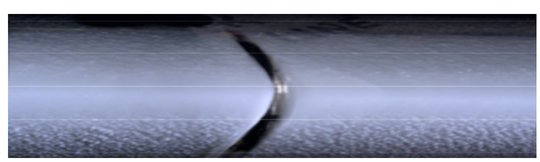

Figure 4-27 Experimental ice profile for Cox case 4

The calculated surface temperature profile on the airfoil reveals temperatures below $0\,^{\circ}C$ (Figure 4-29) indicating a rime region of icing, free of any water-film presence (Figure 4-31). In such regions, the ice crystal model is setup to assume that all crystals bounce and do not contribute to ice accretion. The resulting accretion is therefore strictly governed by water-droplet impingement (Figure 4-33). The effect of increasing LWC_{∞} in case 4, results in a glaze temperature region near the stagnation point, which evolves into a rime region close to the impingement limit (Figure 4-30). The presence of a film (Figure 4-32) in the glaze region allows crystals to stick, and therefore helps contribute to the ice growth (Figure 4-34).

At higher free-stream temperature of $-5\,^{\circ}C$ in case 15, the effects of ice crystals in a mixed phase flow are more visible as compared to the previous cases (Figure 4-28). The addition of ice crystals to the free-stream conditions caused horn-like growths that existed in case 14 (Figure 4-17) to disappear. The existence of a water-film may initially allow for ice crystal sticking, and then subsequently lead to rime ice growth, since the crystals that stick may provide sufficient energy to offset the energy required for freezing, and the impact velocities of crystals can cause film to splash reducing the amount of film that gets converted to ice. Further ice crystal impingement causes pitting and abrasion of the iced surface, which gives a dimple-like appearance. Overall, in comparison with case 14, the amount of ice accreted is less, the appearance more opaque, and the shape more streamlined. The conservative over-prediction of the ice mass (Figure 4-37) is a result of not taking these secondary effects (such as splashing of the water-film, or erosion caused by crystal impingement) into account.

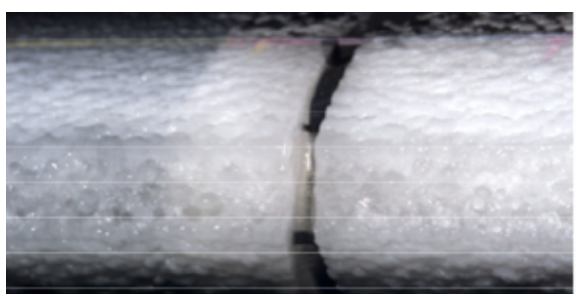

Figure 4-28 Experimental ice profile for Cox case 15

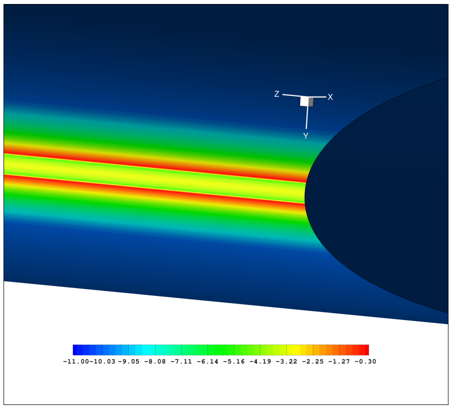

Figure 4-29 Temperature (Celsius) profile for Cox case 3

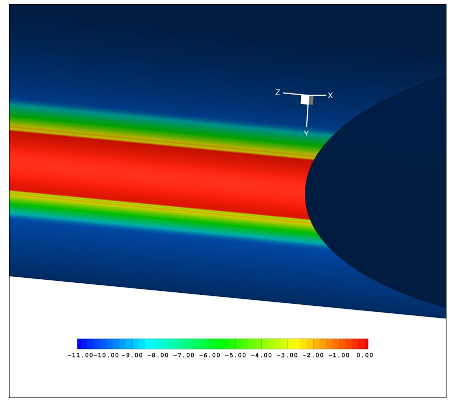

Figure 4-30 Temperature (Celsius) profile for Cox case 4

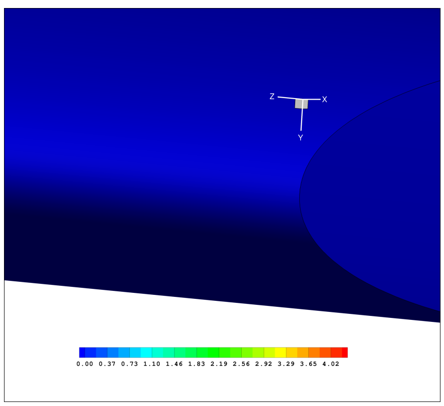

Figure 4-31 Water-film thickness (microns) for Cox case 3

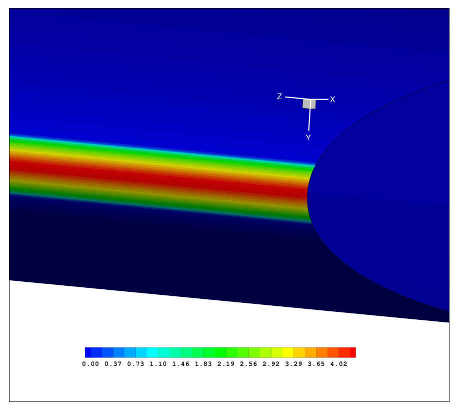

Figure 4-32 Water-film thickness (microns) for Cox case 4

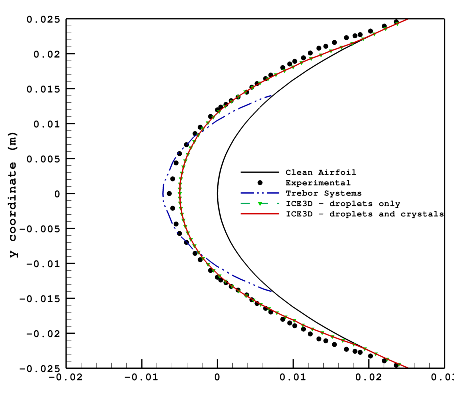

Figure 4-33 Ice profile comparison for Cox case 3

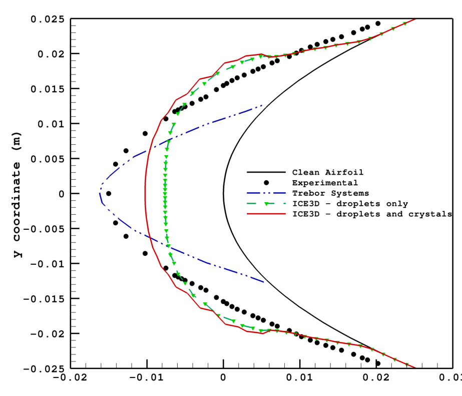

Figure 4-34 Ice profile comparison for Cox case 4

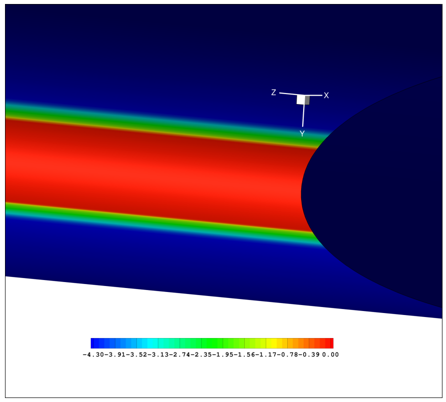

Figure 4-35 Temperature (Celsius) profile for Cox case 15

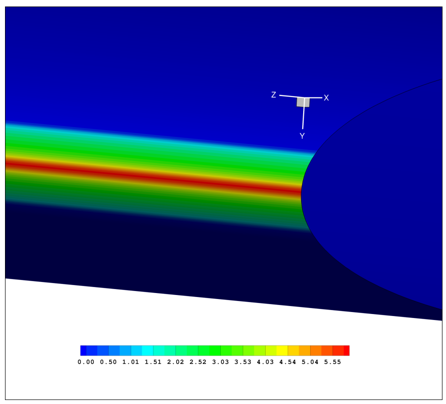

Figure 4-36 Water-film thickness (microns) for Cox Case 15

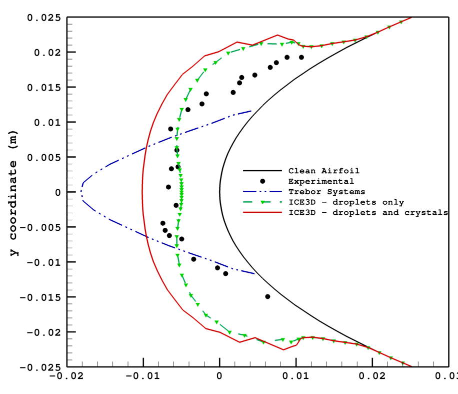

Figure 4-37 Ice profile comparison for Cox case 15

4.3.4.b Comparison with NRC experiments

The experimental icing profiles obtained on the unheated cylinder were shown as two -dimensional cross-sections, and also had corresponding profiles in the absence of ice crystals, in order to observe differences caused by the addition of ice crystals. The numerical simulations conducted in ICE3D will accompany these experimental profiles for the purpose of discussion.

Case 46CM-a and 46CM-b were chosen to evaluate the model predictions with respect to a relative increase in LWC_{∞}, to only a slight increase in ICC_{∞}. The experimental profile comparisons for case 46CM-a in the presence (Figure 4-44), and absence of ice crystals (Figure 4-42), are quite similar and indicate that ice crystals do not greatly affect the ice shape or mass of ice accreted. The numerical comparison also confirms this observation (Figure 4-43), since the temperature profile below $0°C$ (Figure 4-38) indicates no water-film presence (Figure 4-39), and hence no impact of crystals on the resulting numerical ice profile (Figure 4-43). An increase in LWC_{∞} at the same free-stream conditions, results in the formation of horn-like growths on either side of the stagnation point (Figure 4-45). The addition of crystals in this case seems to have removed such horns in case 45M-b (Figure 4-47). The temperature (Figure 4-40) and non-zero film (Figure 4-45) profiles confirm that crystals affect the ice growth. The discrepancy between numerical and experimental results (Figure 4-46) maybe attributed to neglecting secondary splashing or erosive effects due to ice crystal impacts.

The experimental ice shape profiles for case 47CM with ice crystals (Figure 4-50) are quite different from those with only droplets (Figure 4-48). The apparent streamlining of the ice profile suggests that ice crystal erosion at such velocities is more prominent and tends to smoothen feather-like growth that leads to horn formation. The cavity in the vicinity of the stagnation region has been hypothesized to be attributed to the high velocity impacts of ice crystals, although this has not been confirmed in the literature. The consequence of neglecting film splashing or erosive effects at high impact velocities is seen through the over-estimation of the ice growth profile (Figure 4-49).

The effect of ice crystals in case 45CM, results in less runback ice growth (Figure 4-53) as compared to the experimental result containing only droplets (Figure 4-51). The numerical comparison of this profile (Figure 4-52) is in better agreement with the experimental profile than the 47CM case.

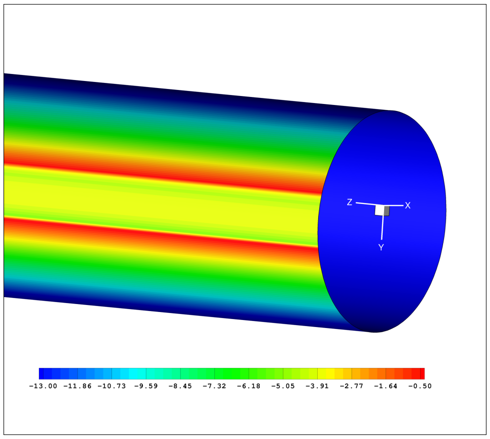

Figure 4-38 Temperature (Celsius) profile for NRC case 46CM-a

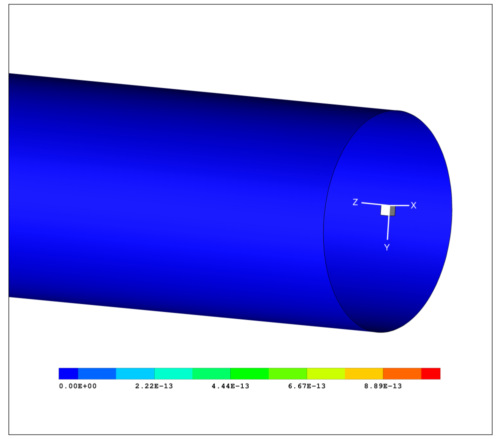

Figure 4-39 Water-film height (microns) for NRC case 46CM-a

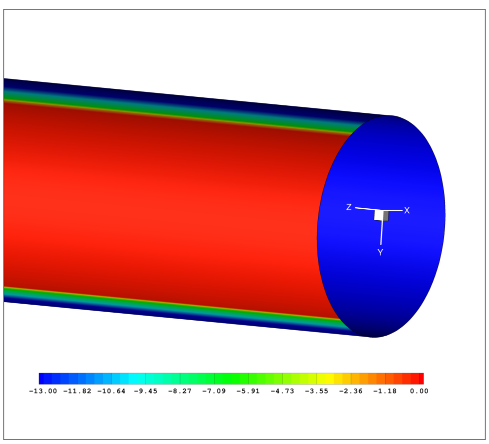

Figure 4-40 Temperature (Celsius) profile for NRC case 46CM-b

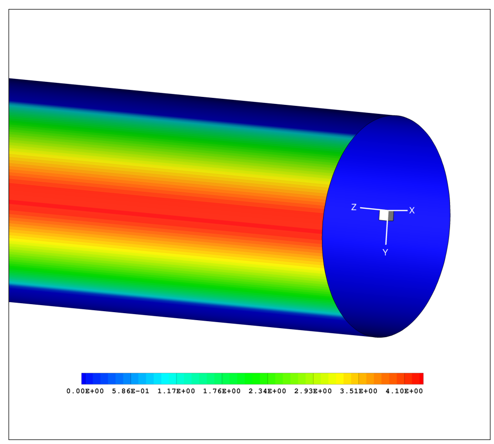

Figure 4-41 Water-film height (microns) for NRC case 46CM-b

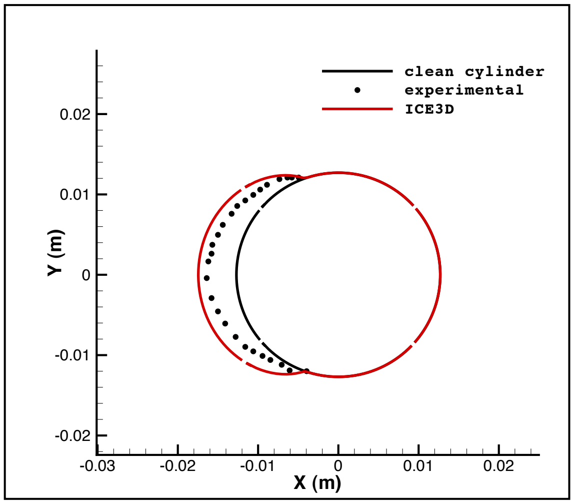

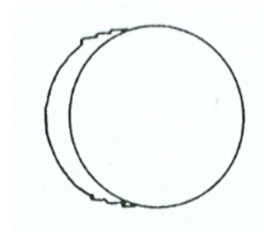

Figure 4-42 Experimental ice profile for NRC case 46CM-a with LWC only

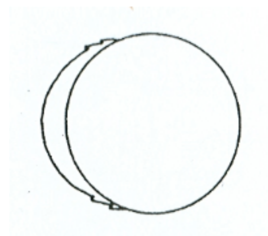

Figure 4-43 Ice profile for comparison for NRC case 46CM-a

Figure 4-44 Experimental ice profile for NRC case 46CM-a with ICC and LWC

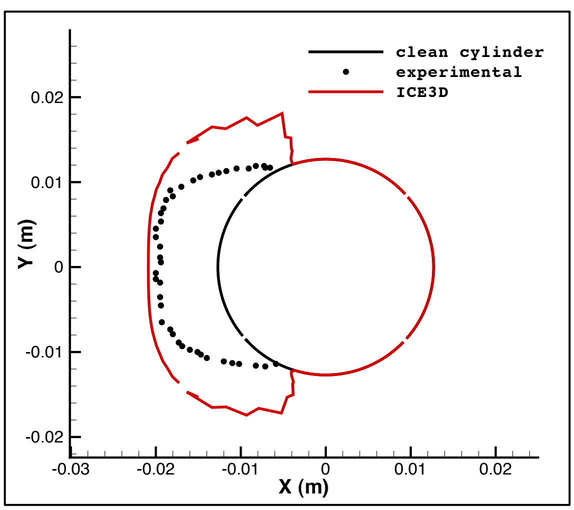

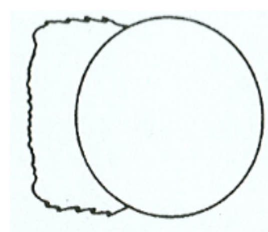

Figure 4-45 Experimental ice profile for NRC case 46CM-b with LWC only

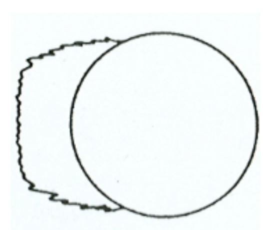

Figure 4-46 Ice profile comparison for NRC case 46CM-b

Figure 4-47 Experimental ice profile for NRC case 46CM-b with ICC and LWC

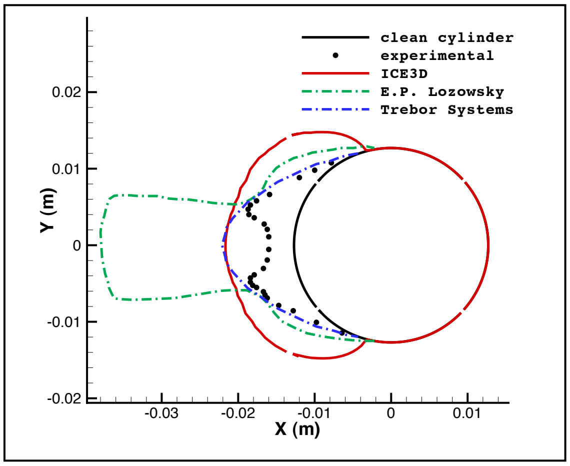

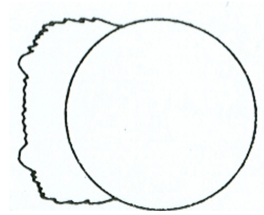

Figure 4-48 Experimental ice profile for NRC case 47CM with LWC only

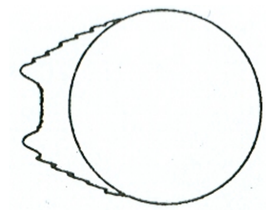

Figure 4-49 Ice profile comparison for NRC case 47CM

Figure 4-50 Experimental ice profile for NRC case 47CM with ICC and LWC

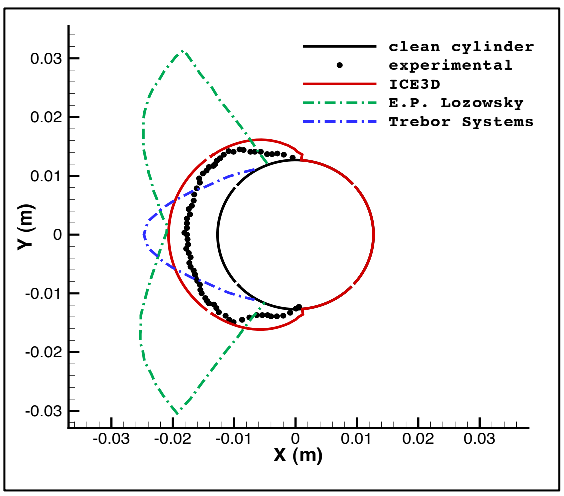

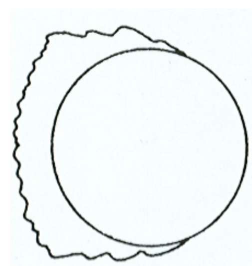

Figure 4-51 Experimental ice profile for NRC case 45CM with LWC only

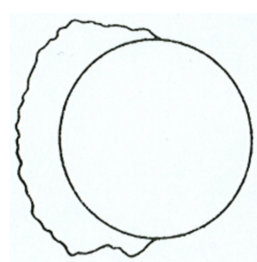

Figure 4-52 Ice profile comparison for NRC case 45CM

Figure 4-53 Experimental ice profile for NRC case 45CM with ICC and LWC

4.4 Summary of Results

The solutions obtained using the extended crystal impingement and ice accretion model in DROP3D and ICE3D have shown a relatively good agreement in determining the ice profiles for Cox and NRC icing tests. The numerical model is an improvement over the other numerical methodologies it has been compared against. The predicted ice shapes involving ice crystals tend to be conservative in general, and tend to over-approximate the ice profile, but are acceptable considering that the model implemented for evaluating the bouncing criterion is proof-of-concept and is not based on any experimental data, and that the secondary effects of erosion, splashing of the film due to crystal impact, or the apparent change in density (by comparing Figure 4-17 and Figure 4-28) are not taken into account.

Another factor that may contribute to discrepancies in the results, particularly when calculating the ice on either side of the stagnation point, is the effect of surface roughness. In the numerical simulation, an equivalent roughness was assumed since it was not provided in the literature. The abrasive nature of crystals in this respect can change the roughness height and its distribution on the iced surface. The problem is inherently unsteady; since the change in roughness, coupled with the change in the surface profile can change the heat flux and shear stress distributions, as well as the collection efficiency on the surface. In this respect, perhaps a fully unsteady approach may lead to a better ice shape prediction.

In view of turbomachines however, the steady-state approximation may suffice, since the analyses of shedding characteristics in rotating components requires only the order of the correct mass of ice, more than its exact shape, assuming the general characteristics of the predicted profile is relatively well represented. The experiments, although providing useful information regarding what aspects of the model need to be enhanced, may not be an adequate baseline for comparison when compared with the environment inside turbomachines. The assumption of instantaneous melting used for ice crystals that stick is based on the fact that rotor and stator surfaces are usually heated, or at a higher than freezing temperature in the core, while the experiments were run using unheated surfaces.

In general, the present numerical model needs to be further enriched with new experimental techniques that mimic turbomachinery environments to provide insights into the crystal interactions on heated surfaces, associated splashing effects existing films, and erosive effects on iced surfaces.

5. Conclusion

Recent aircraft in-flight incidents that point towards ice crystals as a potential cause for sudden engine power-loss conditions has mobilized the icing research community in better characterizing the problem. Traditionally, aircraft surfaces were considered to be safe from any icing involving ice crystals in fully glaciated conditions, since they were understood to bounce off cold, dry surfaces. The proposed hypothesis that has been investigated by researchers is that ice crystals having higher inertia tend to get ingested into the primary core-flow, and do not get centrifuged out towards the engines bypass, where they would be removed. Ice crystals may then melt at higher temperatures experienced downstream, or alternatively, if they hit a heated surface. The water-film that forms on the surface acts as an adhesive-like interface that promotes further impingement of ice crystals, which through energy exchanges may locally lower the temperature at the interface and result in the initiation of ice formation. In addition to potential compressor surge that may be caused by core-flow blockage from the accreting ice, larger pieces of shed-ice off rotating or non-rotating components can either damage components downstream, or lead to a decrease in the burner efficiency and an eventual flameout if ingested into the combustor, to cause a sudden powerloss.

To the author's best knowledge, there currently exists no commercial CFD code that simulates the physics of ice crystals in airflow in the context of analyzing the impact of crystals on the overall ice accretion. The methodologies of Lozowski and Trebor Systems, however, provide useful insights into what aspects of the ice crystal physics need to be focused on and improved for the implementation of an ice crystal model into FENSAP-ICE; a fully 3-D CFD code that incorporates well integrated modules that calculate airflow, droplet and ice accretion.

Chapter 2 discusses a generalized set of particle governing equations that are used to establish concentration fractions, velocities, and impinging mass fluxes of the given particle types (i.e. droplets and ice crystals). Verifying underlying assumptions for ice crystals (such as continuum, dilute gas particle flow) with respect to the finite element Eulerian framework in DROP3D allowed for a seamless extension to model both ice crystals and droplets in an uncoupled multiphase flow, where all phases (continuous and dispersed) are considered to be in thermodynamic equilibrium and inter-phase transfers of mass, momentum and energy are ignored. Some limitations exist if the model is going to be used in the context of turbomachinery flows, such as the requirement of small ice crystal size (100 to 200 microns for characteristic length scales of 6-10 cm for turbomachinery blades), to be consistent with the assumptions of the existing framework. Ice crystals have been modeled as oblate spheroids in this work, since hydrodynamic properties of these shapes have been found to be in good agreement with those of naturally occurring crystals. The crystals geometrical properties (such as size and aspect ratio) have been taken into account through the inertia parameter in the drag term and the coefficient of drag is modeled through experimental correlations that agree well for aspect ratios between 0.05 and 0.5.

Chapter 3 extends the current Messinger Model for ice accretion to incorporate the effect of ice crystals impingement. Ice crystals that stick to a wetted surface are treated as a source terms in the mass and energy equations. The fraction of ice crystals that stick to the wetted surface is determined by a proof-of concept inverse exponential function that depends on the crystal size, the normal velocity of impact, and ratio of film height to maximum film height on the surface. The equations are solved using an explicit control volume formulation that uses the notion of a dual mesh, transferring values from finite element grid points to the finite volume centroids in a one-to-one correspondence. Three icing regions are possible: rime, glaze, or water-film. A set of compatibility relations for each region allows for a physically meaningful solution for the mass of ice, film height, and temperature at the surface.

Chapter 4 verifies the model with respect to the preliminary assumptions made, and validates it against experimental data from the Cox and Co. and NRC icing tunnel experiments. The Cox and NRC validation cases showed a generally good agreement when compared against the experimental profiles, although over-predicted. A number of conclusions however can be drawn with respect to possible improvements that can be made. The simulated accretion profiles for Cox cases 3 and 4 showed an under-estimation of the stagnation line growth. The cause of this could be attributed to neglecting the effect of the evolving ice shape on the wall shear stresses, heat flux and collection efficiency. In glaze conditions, such as those experienced in Cox case 15, the over-prediction of the ice profile is due to splashing effects associated with ice crystal impacts that are not presently accounted for. A similar over-approximation is seen when simulating NRC case 47CM, and is attributed to abrasive effects caused by high velocity impacts of crystals, leading to a more streamlined ice profile than predicted.

In view of the comparisons made between the extended model and the experiments, a few recommendations can be made in order to make it more relevant to icing inside turbomachinery. The particle impingement solver has to be extended to include centrifugal and Coriolis forces on the particle to model the interactions due to rotating components. The current boundary condition on the wall does not allow for re-impingement of particles back into the flow. This however is an important parameter if ice crystal bouncing has to be accounted for, but is difficult in the Eulerian framework, since particles do not interact. Even if bounced trajectories were imposed on the wall, the spatial averaging between the bounced particles concentration cloud and the incoming impingement cloud would result in an average value for variables such as velocity that may not be physically meaningful. One way of handling this is to simulate a bounced impact by calculating an impulse force that would have occurred on the surface, and then apply it to the incoming ice crystals in a way that decreases the impingement mass flux of crystals on the surface. Some work in this area has been done for droplets [15] that splash or bounce, but needs to be calibrated for ice crystals. The icing model itself needs to be improved to allow for splashing and erosional effects associated with ice crystal impact. Unsteady-state effects such as the time delay associated with crystal melting, as well as the inclusion of conduction terms in the icing model (to simulate heat transfer from a heated metallic surface) needs to be considered. In this respect, perhaps a transition from a steady-state analysis such as the current work, to a more comprehensive unsteady implementation maybe useful in the context of turbomachinery flows.

List of References

[1] F.S.F., "Accident description : Antonov 24B, Flight 166", http://aviation-safety.net/database/record.php?id=19951213-0, 1995

[2] Wall, R., "A330 Pitot Tube Icing Concerns Persist", http://www.aviationweek.com/aw/generic/story_generic.jsp?channel=awst&id=news/awst/2010/01/04/AW_01_04_2010_p28-193411.xml&headline=A330%20Pitot%20Tube%20Icing%20Concerns%20Persist, 2010

[3] Pasztor, A., "Airline Regulators Grapple with Engine-Shutdown Peril: Investigators Find New Icing Threat", *Wall Street Journal,* http://online.wsj.com/article/SB120753185285993925.html, 2008

[4] Schultz, P. and Politovich, M., "Toward the improvement of aircraft-icing forecasts for the continental United States," *Weather and Forcasting,* Vol. 7, 1992, p. 491-500.

[5] Macklin, W. C., "The Density and Structure of Ice Formed by Accretion," *Quarterly Journal of the Royal Meteorological Society,* Vol. 88, No. 375, 1962, p. 30-50.

[6] Landsberg, B., "Aircraft Icing", http://www.aopa.org/asf/publications/sa11.pdf, 2008

[7] Linke-Diesinger, A., *Systems of Commercial Turbofan Engines : An Introduction to Systems Functions*, Springer Berlin Heidelberg, 2008, p. 179-183.

[8] Mason, J., "Current Perspectives on Jet Engine Power Loss in Ice Crystal Conditions: Engine Icing", *7th AIRA Research Implementation Forum,* http://icingalliance.org/meetings/RIF_2009/documents/AIAA%20June%202009_Mason_version_nss.pdf, 2009

[9] F.A.A., “Performance and handling characteristics in the icing conditions specified in part 25, appendix C”, U.S. Department of Transportation, 2007.

[10] Bond, T., “F.A.A. Icing Operational Guidance : Proposed Expanded Icing Envelope”, National Transportation and Safety Board, 2009.

[11] Luxford, G., "Experimental and Modelling Investigation of the Deformation, Drag and Breakup of Drizzle Droplets Subjected to Strong Aerodynamic Forces in Relation to SLD Aircraft Icing," School of Engineering, Cranfield University, 2005.

[12] Tan, S. C. and Papadakis, M.,"General Effects of Large Droplet Dynamics on Ice Accretion Modeling," *41st Aerospace Sciences Meeting and Exhibit*, AIAA 2003-392, Reno, Nevada, 2003.

[13] Bragg, M. B. and Loth, E., "Effects of Large Droplet Ice Accretion on Airfoil and Wing Aerodynamics and Control", NASA, 2000.

[14] Mazzawy, R. S. and Strapp, W.,"Appendix D - An interim Icing Envelope," SAE, 2007-01-3311, 2007.

[15] Honsek, R. and Habashi, W. G.,"FENSAP-ICE: Eulerian Modeling of Droplet Impingement in the SLD regime of Aircraft Icing," *44th AIAA Aerospace Sciences Meeting and Exhibit*, AIAA 2006-465, Reno, Nevada, 2006.

[16] Wright, W. B., "Validation Results for LEWICE", QSS Group Inc., 2005.

[17] Mason, J., Strapp, W. and Chow, P.,"The Ice Particle Threat to Engines in Flight," *44th AIAA Aerospace Sciences Meeting and Exhibit*, AIAA 2006-206, Reno, 2006.

[18] 332, A. A. R. N., "Recommended practices for the assessment of the effects of atmospheric water ingestion on the performance and operability of gas turbine engines", *Liquid water, snow and hail : Effects on components and engine*, 1995.

[19] Lozowski, E. W., Stallabrass, J. R. and Hearty, P. P., "The icing of an Unheated Non-Rotating Cylinder in Liquid Water Droplet - Ice Crystal Clouds", National Research Council 1979.

[20] Cansdale, J. T. and McNaughtan, I. I., "Calculation of Surface Temperature and Ice Accretion Rate in a Mixed Water Droplet/Ice Crystal Cloud", 1977.

[21] Langmuir, I. and Blodgett, K. B., "Mathematical investigation of water-droplet trajectories", U.S.A.A.F. Technical Report 5418, 1946.

[22] Mazzawy, R. S.,"Modeling of Accretion and Shedding in Turbofan Engines with Mixed Phase/Glaciated (Ice Crystal) Conditions," *Aircraft and Engine Icing International Conference*, SAE 2007-01-3288, Seville, Spain, 2007.

[23] Reich, A. D., Scavusso, R. J. and Chu, M. L.,"Survey of mechanical properties of impact ice," *32nd Aerospace Sciences Meeting and Exhibit*, AIAA 94-0712, Reno, NV, 1994.

[24] Beaugendre, H., Morency, F. and Habashi, W. G., "ICE3D, FENSAP-ICE's 3D In-Flight Ice Accretion Module," *AIAA Journal of Aircraft,* Vol. 40, No. 2, 2003, p. 239-247.

[25] Habashi, W. G., Aube, M., Baruzzi, G., Morency, F. and Tran, P.,"FENSAP-ICE : A fully 3D Inflight Icing Simulation System for Aircraft, Rotorcraft and UAV's," *24th International Congress for the Aeronautical Sciences*, 2004.

[26] Veillard, X., Aliaga, C. and Habashi, W. G.,"FENSAP-ICE: Modeling of the Ice Crystal Threat to Engine Icing," *Aircraft and Engine Icing International Conference*, SAE 2007-01-3323, Seville, Spain, 2007.

[27] Veillard, X., Habashi, W. G. and Baruzzi, G.,"FENSAP-ICE:Ice Accretion in Multistage Jet Engines," *1st Atmospheric and Space Environments Conference*, AIAA AIAA-2009-4158, 2009.

[28] Dawes, W. N., "Toward Improved Through-flow Capability: The use of Three-Dimensional Viscous Flow Solvers in a Multistage Environment," *Journal of Turbomachinery,* Vol. 114, No. 1, 1992, p. 8.

[29] Messinger, B. L., "Equilibrium temperature of an unheated icing surface as a function of air speed," *Journal of the Aeronautical Sciences,* Vol. 20, No. 1, 1953, p. 28-42.

[30] Khalil, K. A., “Assessment of Effects of Mixed Phase Icing Conditions on Thermal Ice Protection Systems” *DOT/FAA/AR-03/48*, Cox & Company, 2003.

[31] Schwer, D. A. and Kailasanath, K., "Direct comparison of particle-tracking and sectional approaches for shock driven flows," *International Journal of Spray and Combustion Dynamics,* Vol. 1, No. 1, 2008, p. 1-38.

[32] Bourgault, Y., Habashi, W. G., Dompierre, J. and Baruzzi, G., "A Finite Element Method Study of Eulerian Droplets Impingement Models," *Int. J. for Numerical Methods in Fluids,* Vol. 29, No. 4, 1999, p. 429 - 449.

[33] Clift, R., Grace, J. R. and Weber, M. E., *Bubbles, Drops and Particles*, Academic Press, New York, 1978.

[34] Temam, R., *Navier Stokes equations : theory and numerical analysis*, American Mathematical Society, New York, 1979.

[35] Pitter, R. L., Pruppacher, H. R. and Hamielec, A. E., "A Numerical Study of Viscous Flow Past a Thin Oblate Spheroid at Low and Intermediate Reynolds Numbers," *Journal of Atmospheric Sciences,* Vol. 30, 1973, p. 125-134.

[36] Pitter, R. L. and Pruppacher, H. R., "A Numerical Investigation of Simple Ice Plates Colliding with Supercooled Water Drops," *Journal of Atmospheric Sciences,* Vol. 31, 1974, p. 551-559.

[37] Giacinto, M. D., Piva, R. and Sabetta, F., "Two way coupling effects in dilute gas particle flows," *ASME Journal of Fluids Engineering,* Vol. 104, 1982, p. 304-311.

[38] Da Silveira, R. A. and Maliska, C. R.,"Numerical Simulation of Ice Accretion on the Leading Edge of Aerodynamic Profiles," *2nd International Conference on Computational Heat and Mass Transfer*, Rio de Janeiro, 2001.

[39] Farrall, M., Simmons, K. and Hibberd, S., "A Numerical Model for Oil Film Flow in an Aeroengine Bearing Chamber and Comparison to Experimental Data," *J. Eng. Gas Turbines Power,* Vol. 128, No. 1, 2006, p. 111.

[40] Morency, F. and Habashi, W. G.,"Low-Water Concentration Zone Prediction with a 3D Eulerian Droplet Impingement Icing Code," *European Congress on Computational Methods in Applied Sciences and Engineering (ECCOMAS)*, 2004.

[41] Magono, C. and Lee, W., "Meteorological Classification of Natural Snow Crystals," *Journal of the Faculty of Science*, 1966, p. pp321,335.

[42] Jayaweera, K. O. L. F. and Cottis, R. E., "Fall velocities of plate-like and columnar ice crystals," *The Quarterly Journal of the Royal Meteorological Society,* Vol. 95, No. 406, 1969, p. 703-709.

[43] List, R. and Schemenauer, R. S., "Free Fall Behaviour of Planar Snow Crystals, Conical Graupel and Small Hail," *Journal of Atmospheric Sciences,* Vol. 28, 1971, p. 110-115.

[44] Happel, J. and Brenner, H., *Low - Reynolds Number Hydrodynamics*, Prentice Hall, 1965, p. 553.

[45] Iuliano, E., Brandi, V., Mingione, G., de Nicola, C. and Tognaccini, R.,"Water Impingement Prediction on Multi-Element Airfoils by Means of Eulerian and Lagrangian Approach with Viscous and Inviscid Air Flow," *44th Aerospace Sciences Meeting and Exhibit*, AIAA 2006-1270, Reno, NV, 2006.

[46] Saad, Y. and Schultz, M. H., "GMRES: A Generalized Minimal Residual Algorithm for Solving Nonsymmetric Linear Systems," *J. of Scientific and Statistical Computing,* Vol. 7, No. 3, 1986, p. 856-869.

[47] Da Silveira, R. A., Maliska, C. R. and Estivam, D. A.,"Evaluation of collection efficiency methods for icing analysis," *17th International Congress of Mechanical Engineering*, ABCM, Sao Paulo, 2003.

[48] Yarin, A. L., "Drop Impact Dynamics: Splashing, Spreading, Receding, Bouncing..." *Annual Review of Fluid Mechanics,* Vol. 38, 2006, p. 159-192.

[49] Do-Quang, M. and Amberg, G., "The splash of a solid sphere impacting on a liquid surface: Numerical simulation of the influence of wetting," *Physics of Fluids,* Vol. 21, 2009.

[50] Beaugendre, H., "A PDE-Based 3D Approach to In-Flight Ice Accretion," Mechanical Engineering, McGill Univesity, Montreal, 2003.

[51] Hedde, T., "Modélisation tridimensionnelle des dépôts de givre sur les voilures d'aéronefs," Université Blaise-Pascal, 1992.

[52] MacArthur, C. D., Keller, J. L. and Leurs, J. K.,"Mathematical Modeling of Ice Accretion on airfoils," *20th Aerospace Sciences Meeting*, AIAA, Orlando, 1982.

[53] Gent, R. W., Dart, N. P. and Cansdale, J. T., "Aircraft Icing," *Philos. Trans. R. Soc. London,* Vol. A 358, 2000, p. 2873.

[54] Hertz, H. J., " ber die berhrung fester elasticher krper," *J. Reine und Angewandte Mathematik,* Vol. 92, 1882, p. 156-171.

[55] Gondret, P., Hallouin, E. a. L., M. and Petit, L., "Experiments on the motion of a solid sphere toward a wall : From viscous dissipation to elastohydrodynamic bouncing," *Physics of Fluids,* Vol. 11, No. 9, 1999, p. 2803 - 2805.

[56] Davis, R. H., Serayssol, J. M. and Hinch, E. J., "The elastohydrodynamic collision of two spheres," *Journal of Fluid Mechanics,* Vol. 163, 1986, p. 479-497.

[57] Kantak, A., A. and Davis, R. H., "Oblique collisions and rebound of spheres from a wetted surface," *Journal of Fluid Mechanics,* Vol. 509, 2004, p. 63-81.

[58] Barnocky, G. and Davis, R. H., "Elastohydrodynamic collision and rebound of spheres : experimental verification," *Physics of Fluids,* Vol. 31, 1988, p. 1324-1329.

[59] Roe, P. L., "Approximate Riemann Solvers, Parameter Vectors, and Difference Schemes," *Journal of Computational Physics,* Vol. 43, 1981, p. 357-372.

[60] Toro, E. F., *Riemann Solvers and Numerical Methods for Fluid Dynamics, A Practical Introduction*, Springer, 1999.

[61] Spalart, P. R. and Allmaras, S. R.,"A One-Equation Turbulence Model for Aerodynamic Flows," *30th AIAA Aerospace Sciences Meeting*, AIAA 92-0439, Reno, 1992.

[62] Aupoix, B. and Spalart, P. R., "Extensions of the Spalart-Allmaras turbulence model to account for wall roughness," *International Journal of Heat and Fluid Flow,* Vol. 24, 2003, p. 454-462.

[63] Hughes, T. J. R. and Brooks, A., "A Theoretical Framework for Petrov-Galerkin Methods with Discontinuous Weighting Functions: Application to the Streamline-Upwind Procedure," in *Finite Elements in Fluids*, vol. 4, John Wiley, 1982, ch. 3.

[64] Brooks, A. and Hughes, T. J. R., "Streamline upwind/Petrov-Galerkin formulations for convection dominated flows with particular emphasis on the incompressible Navier-Stokes equations," *Computer Methods in Applied Mechanics and Engineering,* Vol. 32, No. 1-3, 1982, p. 199-259.

I. Finite Element Formulation of Particle Equations in DROP3D

The strong form of the equations governing particle motion can be written as

Mass Conservation

$$\frac{\partial(\alpha)}{\partial t}+\frac{\partial\left(\alpha v_j\right)}{\partial x_j}=0 \qquad \textbf{Eq. I-1}$$

Momentum Conservation

$$\frac{\partial\left(\alpha v_i\right)}{\partial t}+\frac{\partial\left(\alpha v_j v_i\right)}{\partial x_j}=\alpha\left[\frac{1}{Fr^2}\left(1-\frac{\rho_a}{\rho_p}\right)g_i+\frac{C_d \operatorname{Re}_p}{4K_p}\left(v_{a,i}-v_i\right)\right] \qquad \textbf{Eq. I-2}$$

Boundary Conditions

$$\rho\big|_{\Omega}=\rho_{\Omega}$$
$$v_i\big|_{\Omega}=v_{i\Omega}$$
$$\rho v_i \bullet n_i\big|=\Gamma_{\Omega}$$

Where α refers to the particle volume fraction, $v_{i/j}$ and $v_{a,i}$ the particle velocity component and air velocity component for a given coordinate direction, Fr is the particle Froude number, g_i is the component of acceleration due to gravity, C_d is the particle drag coefficient, Re_p is the particle Reynolds number, K_p is the particle inertia parameter. ρ_p is the particle density and ρ_a is the density of air. The boundary conditions indicate Dirichlet conditions for ρ and v_i that are applied to the inlet of the domain and a Neumann boundary condition that is used for wall boundaries. The spatial continuum bounded by the boundary Ω is split into a set of discrete smaller elements of volume V. Each node on an element represents 4 degrees of freedom corresponding to unknown quantities α, v_1, v_2, v_3 representing local volume fraction and three velocity components in a given coordinate system.

The solution to the governing equations applied to a single element yields a continuous representation of the field variables over the entire element. The equations applied to all elements in the domain results in a series of algebraic equations that need to be solved. The Galerkin Finite element method is used to represent the equations in its 'weak form', details of which are shown in the subsequent section.

I.A Spatial Discretization

Any continuous quantity inside a given element containing '*ndperl*' nodes can be approximated in terms of interpolation shape functions used to describe the element

$$\phi_e(x_1,x_2,x_3) \simeq \phi(x_1,x_2,x_3) = \sum_{k=1}^{ndperl} N_k(x_1,x_2,x_3)\phi_k \qquad \textbf{Eq. I-3}$$

where ϕ_e represents the exact quantity and ϕ is an approximation to the quantity at spatial coordinates x_1,x_2,x_3. N_k is the kth shape function and ϕ_k is the scalar value of ϕ defined at node k.

I.B Time Discretization

The time dependent conservative equations Eq. I-1 and Eq. I-2 have to be solved discretely in time for all time levels. The current time level will be denoted by a superscript 'm' and a backward Euler scheme will be used to represent the discretization for any function f in time t

$$\frac{\partial f}{\partial t} = \frac{f^m - f^{m-1}}{\Delta t} \qquad \textbf{Eq. I-4}$$
$$\Delta t = t^m - t^{m-1}$$

Note that this form of the time discretized term is not representative of what is actually coded inside DROP3D and only serves to complete the presentation of the discretization procedure.

I.C Newton Linearization

In order to improve convergence characteristics, each term in the equation is linearized to obtain a modified linear system. For a given spatial iteration level, subscript '*n*', at the present time level '*m*', any variable of interest ϕ can be written in terms of its value at the previous iteration level '*n-1*' and a perturbation at the present iteration level $\Delta\phi$

$$\phi_n^m = \phi_{n-1}^m + \Delta\phi_n^m \qquad \textbf{Eq. I-5}$$

I.D Continuity Equation

The weighted integral form of the continuity equation for a given elemental sub-space V in a domain enclosed by an internal boundary ζ is

$$\int_V W_1 \left(\frac{\partial(\alpha)}{\partial t} + \frac{\partial(\alpha v_j)}{\partial x_j} \right) dV = 0 \qquad \textbf{Eq. I-6}$$

Where W_1 represents the weighting function for mass conservation, and the j subscript implies summation over the spatial coordinates. Integrating the convection term by parts yields

$$\int_V \left(W_1 \frac{\partial(\alpha)}{\partial t} - \alpha v_j \frac{\partial(W_1)}{\partial x_j} \right) dV + \oint_\zeta W_1 \alpha v_j n_j dS = 0 \qquad \textbf{Eq. I-7}$$

The so-called weak form in Eq. I-7 allows for natural specification of boundary conditions at the boundary through the surface integral term. Applying Eq. I-4 to the time derivative term, assuming all other spatial terms are at time level ‘m’ and linearizing terms at this time level using Eq. I-5 yields

$$\begin{aligned} &\int_V W_1 \frac{\alpha_{n-1}^m + \Delta\alpha_n^m - \alpha^{m-1}}{\Delta t} dV - \int_V \left(\alpha_{n-1}^m + \Delta\alpha_n^m\right)\left(v_{j,n-1}^m + \Delta v_{j,n}^m\right) \frac{\partial(W_1)}{\partial x_j} dV \\ &+ \oint_\zeta W_1 \left(\alpha_{n-1}^m + \Delta\alpha_n^m\right)\left(v_{j,n-1}^m + \Delta v_{j,n}^m\right) n_j dS = 0 \end{aligned} \qquad \textbf{Eq. I-8}$$

Expanding Eq. I-8 and simplifying by neglecting terms involving Δ^2 gives:

$$\begin{aligned} &\int_V W_1 \frac{\Delta\alpha_n^m}{\Delta t} dV - \int_V v_{j,n-1}^m \Delta\alpha_n^m \frac{\partial(W_1)}{\partial x_j} dV - \int_V \alpha_{n-1}^m \Delta v_{j,n}^m \frac{\partial(W_1)}{\partial x_j} dV \\ &+ \oint_\zeta W_1 \Delta\alpha_n^m v_{j,n-1}^m n_j dS + \oint_\zeta W_1 \alpha_{n-1}^m \Delta v_{jn}^m n_j dS \\ &= \int_V W_1 \frac{\alpha^{m-1}}{\Delta t} dV - \left[\int_V W_1 \frac{\alpha_{n-1}^m}{\Delta t} dV - \int_V v_{j,n-1}^m \alpha_{n-1}^m \frac{\partial(W_1)}{\partial x_j} dV + \oint_\zeta W_1 \alpha_{n-1}^m v_{j,n-1}^m n_j dS \right] \end{aligned} \qquad \textbf{Eq. I-9}$$

Where the incremental quantities at time level ‘m’ are grouped on the left-hand-side, and known quantities at time level ‘m-1’ or iteration level ‘n-1’ are on the right-hand-side. The inertial term at time level ‘m-1’ is frozen at the previous time level and remains unchanged for all Newton iteration levels at the given time iteration level ‘m’. The other terms on the right-hand-side contribute to the calculation of the residual at each iteration level ‘n-1’ for time level ‘m’. To simplify indices, all superscripts at time level ‘m’ will be omitted and values will be assumed at this time level unless otherwise specified. As mentioned earlier, interpolation shape functions are used to approximate the functional space for each unknown variable. Here, N_k will be used to represent α and $\Delta\alpha$, while N_l will represent the velocity components v_i

$$(\Delta)\alpha(x_1,x_2,x_3) = \sum_{k=1}^{ndperl} N_k(x_1,x_2,x_3)(\Delta)\alpha_k$$
$$(\Delta)v_i(x_1,x_2,x_3) = \sum_{l=1}^{ndperl} N_l(x_1,x_2,x_3)(\Delta)v_{il} \qquad \textbf{Eq. I-10}$$

The summation sign will be excluded from now on, and the following simplification will be applied to terms at the previous Newton iteration level 'n-1':

$$\left(N_k\alpha_k\right)_{n-1}^{m} = \widehat{\alpha}$$
$$\left(N_l v_{il}\right)_{n-1}^{m} = \hat{v}_i \qquad \textbf{Eq. I-11}$$

Applying Eq. I-10 and Eq. I-11 to Eq. I-9 yields the final discretized form of the continuity equation:

$$\int_V W_1 N_k \frac{\Delta\alpha_{nk}}{\Delta t} dV - \int_V \hat{v}_j N_k \Delta\alpha_{nk} \frac{\partial(W_1)}{\partial x_j} dV - \int_V \widehat{\alpha} N_l \Delta v_{jnl} \frac{\partial(W_1)}{\partial x_j} dV$$
$$+\oint_\zeta W_1 N_k \Delta\alpha_{nk} \hat{v}_j n_j dS + \oint_\zeta W_1 \widehat{\alpha} N_l \Delta v_{jnl} n_j dS = \int_V W_1 \frac{\alpha^{m-1}}{\Delta t} dV \qquad \textbf{Eq. I-12}$$
$$-\left[\int_V W_1 \frac{\widehat{\alpha}}{\Delta t} dV - \int_V \hat{v}_j \widehat{\alpha} \frac{\partial(W_1)}{\partial x_j} dV + \oint_\zeta W_1 \widehat{\alpha} \hat{v}_j n_j dS\right]$$

I.E Momentum Equation

The weighted integral form of a component of momentum equations is:

$$\int_V W_{2i} \left(\frac{\partial\left(\alpha v_i\right)}{\partial t} + \frac{\partial\left(\alpha v_j v_i\right)}{\partial x_j} \right) dV = \int_V W_{2i} rhs^* dV \qquad \textbf{Eq. I-13}$$

Where W_{2i} represents the weight function corresponding to a given momentum direction and will not imply summation in the case of repeated indices containing 'i' subscripts. The right-hand-side containing rhs^* is

$$\int_V W_{2i} rhs^* dV = \int_V W_{2i} \alpha \left[\lambda_i + \psi \left(v_{a,i} - v_i \right) \right] dV$$

$$\psi = \frac{C_d \operatorname{Re}_p}{4K} \qquad \lambda_i = \frac{1}{Fr^2} \left(1 - \frac{\rho_a}{\rho_p} \right) g_i \qquad \textbf{Eq. I-14}$$

Integrating the spatial derivative term in Eq. I-13 yields

$$\int_V W_{2i} \frac{\partial(\alpha v_i)}{\partial t} - \alpha v_j v_i \frac{\partial(W_{2i})}{\partial x_j} dV + \oint_\zeta W_{2i} \alpha v_j v_i n_j dS = \int_V W_{2i} rhs^* dV \qquad \textbf{Eq. I-15}$$

Applying Eq. I-4 to the time derivative and linearizing all terms at time level 'm' using Eq. I-5 on the left hand side gives:

$$\begin{aligned}
&\int_V \frac{W_{2i}}{\Delta t} (\alpha v_i)_{n-1}^m dV + \int_V \frac{W_{2i}}{\Delta t} v_{i,n-1}^m \Delta\alpha_n^m dV + \int_V \frac{W_{2i}}{\Delta t} \alpha_{n-1}^m \Delta v_{in}^m dV - \int_V \frac{W_{2i}}{\Delta t} (\alpha v_i)^{m-1} dV \\
&- \int_V \left(\alpha v_j v_i\right)_{n-1}^m \frac{\partial(W_{2i})}{\partial x_j} dV - \int_V \Delta\alpha_n^m \left(v_j v_i\right)_{n-1}^m \frac{\partial(W_{2i})}{\partial x_j} dV - \int_V \Delta v_{in}^m \left(\alpha v_j\right)_{n-1}^m \frac{\partial(W_{2i})}{\partial x_j} dV \\
&- \int_V \Delta v_{jn}^m \left(\alpha v_i\right)_{n-1}^m \frac{\partial(W_{2i})}{\partial x_j} dV + \oint_\zeta W_{2i} \left(\alpha v_j v_i\right)_{n-1}^m n_j dS + \oint_\zeta W_{2i} \Delta\alpha_n^m \left(v_j v_i\right)_{n-1}^m n_j dS \\
&\oint_\zeta W_{2i} \Delta v_{in}^m \left(\alpha v_j\right)_{n-1}^m n_j dS + \oint_\zeta W_{2i} \Delta v_{jn}^m \left(\alpha v_i\right)_{n-1}^m n_j dS = \int_V W_{2i} rhs^* dV
\end{aligned} \qquad \textbf{Eq. I-16}$$

Linearizing terms on the right hand side gives:

$$\begin{aligned}
&\int_V W_{2i} \alpha \left[\lambda_i + \psi \left(v_{a,i} - v_i \right) \right] dV = \int_V W_{2i} \alpha_{n-1}^m \left[\lambda_i + \psi \left(v_{a,i} - v_{i,n-1}^m \right) \right] dV \\
&+ \int_V W_{2i} \alpha_{n-1}^m \psi \Delta v_{in}^m dV + \int_V W_{2i} \Delta\alpha_n^m \left[\lambda_i + \psi \left(v_{a,i} - v_{i,n-1}^m \right) \right] dV
\end{aligned} \qquad \textbf{Eq. I-17}$$

By moving all terms involving Δ in Eq. I-17 to the left, replacing unknowns by their interpolation function approximations as in Eq. I-10, and using simplifications presented in Eq. I-11, the discretized form of the momentum equation can be determined, where the superscript 'm' is omitted for simplicity and all terms are at time level 'm' unless otherwise specified:

$$\int_V \frac{W_{2i}}{\Delta t}\hat{v}_i N_k \Delta\alpha_{nk}\, dV + \int_V \frac{W_{2i}}{\Delta t}\hat{\alpha} N_l \Delta v_{inl}\, dV - \int_V \hat{v}_j \hat{v}_i N_k \Delta\alpha_{nk} \frac{\partial(W_{2i})}{\partial x_j} dV$$
$$-\int_V \hat{\alpha}\hat{v}_j N_l \Delta v_{inl} \frac{\partial(W_{2i})}{\partial x_j} dV - \int_V \hat{\alpha}\hat{v}_i N_l \Delta v_{jnl} \frac{\partial(W_{2i})}{\partial x_j} dV + \oint_\zeta W_{2i} N_k \Delta\alpha_{nk} \hat{v}_j \hat{v}_i n_j dS$$
$$+\oint_\zeta W_{2i} N_l \Delta v_{in} \hat{\alpha}\hat{v}_j n_j dS + \oint_\zeta W_{2i} N_l \Delta v_{jnl} \hat{\alpha}\hat{v}_i n_j dS - \int_V W_{2i} \hat{\alpha}\psi N_l \Delta v_{inl} dV \quad \textbf{Eq. I-18}$$
$$-\int_V W_{2i} N_k \Delta\alpha_{nk}\left[\lambda_i + \psi\left(v_{a,i} - \hat{v}_i\right)\right] dV = \int_V \frac{W_{2i}}{\Delta t}\left(\alpha v_i\right)^{m-1} dV - \left[\int_V \frac{W_{2i}}{\Delta t}\hat{\alpha}\hat{v}_i\, dV\right.$$
$$\left. -\int_V \hat{\alpha}\hat{v}_j \hat{v}_i \frac{\partial(W_{2i})}{\partial x_j} dV + \oint_\zeta W_{2i}\hat{\alpha}\hat{v}_j \hat{v}_i n_j dS\right] + \int_V W_{2i}\hat{\alpha}\left[\lambda_i + \psi\left(v_{a,i} - \hat{v}_i\right)\right] dV$$

I.F Element Stiffness Matrix

The discretization of the particle equations by the Galerkin finite element method results in a linear system of equations that can be represented by a 16 entry local stiffness matrix A, a set of unknowns $\Delta\phi$ and a residual R for each element in the spatial domain

$$A\Delta x = R$$

$$A = \begin{bmatrix} A_{1,1} & A_{1,2} & A_{1,3} & A_{1,4} \\ A_{2,1} & A_{2,2} & A_{2,3} & A_{2,4} \\ A_{3,1} & A_{3,2} & A_{3,3} & A_{3,4} \\ A_{4,1} & A_{4,2} & A_{4,3} & A_{4,4} \end{bmatrix} \quad \Delta\phi = \begin{bmatrix} \Delta\alpha \\ \Delta v_1 \\ \Delta v_2 \\ \Delta v_3 \end{bmatrix} \quad R = \begin{bmatrix} R_1 \\ R_2 \\ R_3 \\ R_4 \end{bmatrix}$$

Each entry in A is in-turn a sub-matrix [*ndperl by ndperl*], which is a function of the number of nodes 'ndperl' present in each element. The entries on the first row can be deduced from the continuity equation expressed in Eq. I-12:

$$A_{1,1} = \int_V \frac{W_1 N_k}{\Delta t} dV - \int_V \hat{v}_j N_k \frac{\partial(W_1)}{\partial x_j} dV + \oint_\zeta W_1 N_k \hat{v}_j n_j dS$$

$$A_{1,2} = -\int_V \hat{\alpha} N_l \frac{\partial(W_1)}{\partial x_1} dV - \oint_\zeta W_1 \hat{\alpha} N_l n_1 dS$$

$$A_{1,3} = -\int_V \hat{\alpha} N_l \frac{\partial(W_1)}{\partial x_2} dV - \oint_\zeta W_1 \hat{\alpha} N_l n_2 dS$$

$$A_{1,4} = -\int_V \hat{\alpha} N_l \frac{\partial(W_1)}{\partial x_3} dV - \oint_\zeta W_1 \hat{\alpha} N_l n_3 dS$$

Subsequent row entries for the momentum equation in Eq. I-18 are expressed as:

$$A_{2,1} = \int_V \frac{W_{21}}{\Delta t} \hat{v}_1 N_k \, dV - \int_V \hat{v}_j \hat{v}_1 N_k \frac{\partial\left(W_{21}\right)}{\partial x_j} dV - \int_V W_{21} N_k \left[\lambda_1 + \psi\left(v_{a,1} - \hat{v}_1 \right) \right] dV + \oint_\zeta W_{21} N_k \hat{v}_j \hat{v}_1 n_j dS$$

$$A_{2,2} = \int_V \frac{W_{21}}{\Delta t} \hat{\alpha} N_l \, dV - \int_V \hat{\alpha} \hat{v}_j N_l \frac{\partial\left(W_{21}\right)}{\partial x_j} dV - \int_V \hat{\alpha} \hat{v}_1 N_l \frac{\partial\left(W_{21}\right)}{\partial x_1} dV - \int_V W_{21} \hat{\alpha} \psi N_l dV + \oint_\zeta W_{21} N_l \hat{\alpha} \hat{v}_j n_j dS$$
$$+\oint_\zeta W_{21} N_l \hat{\alpha} \hat{v}_1 n_1 dS$$

$$A_{2,3} = -\int_V \hat{\alpha} \hat{v}_1 N_l \frac{\partial\left(W_{21}\right)}{\partial x_2} dV + \oint_\zeta W_{21} N_l \hat{\alpha} \hat{v}_1 n_2 dS$$

$$A_{2,4} = -\int_V \hat{\alpha} \hat{v}_1 N_l \frac{\partial\left(W_{21}\right)}{\partial x_3} dV + \oint_\zeta W_{21} N_l \hat{\alpha} \hat{v}_1 n_3 dS$$

$$A_{3,1} = \int_V \frac{W_{22}}{\Delta t} \hat{v}_2 N_k \, dV - \int_V \hat{v}_j \hat{v}_2 N_k \frac{\partial\left(W_{22}\right)}{\partial x_j} dV - \int_V W_{22} N_k \left[\lambda_2 + \psi\left(v_{a,2} - \hat{v}_2 \right) \right] dV + \oint_\zeta W_{22} N_k \hat{v}_j \hat{v}_2 n_j dS$$

$$A_{3,2} = -\int_V \hat{\alpha} \hat{v}_2 N_l \frac{\partial\left(W_{22}\right)}{\partial x_1} dV + \oint_\zeta W_{22} N_l \hat{\alpha} \hat{v}_2 n_1 dS$$

$$A_{3,3} = \int_V \frac{W_{22}}{\Delta t} \hat{\alpha} N_l \, dV - \int_V \hat{\alpha} \hat{v}_j N_l \frac{\partial\left(W_{22}\right)}{\partial x_j} dV - \int_V \hat{\alpha} \hat{v}_2 N_l \frac{\partial\left(W_{22}\right)}{\partial x_2} dV - \int_V W_{22} \hat{\alpha} \psi N_l dV + \oint_\zeta W_{22} N_l \hat{\alpha} \hat{v}_j n_j dS$$
$$+\oint_\zeta W_{22} N_l \hat{\alpha} \hat{v}_2 n_2 dS$$

$$A_{3,4} = -\int_V \hat{\alpha} \hat{v}_2 N_l \frac{\partial\left(W_{22}\right)}{\partial x_3} dV + \oint_\zeta W_{22} N_l \hat{\alpha} \hat{v}_2 n_3 dS$$

$$A_{4,1} = \int_V \frac{W_{23}}{\Delta t}\hat{v}_3 N_k\,dV - \int_V \hat{v}_j \hat{v}_3 N_k \frac{\partial(W_{23})}{\partial x_j}dV - \int_V W_{23} N_k\left[\lambda_3 + \psi\left(v_{a,3} - \hat{v}_3\right)\right]dV + \oint_\zeta W_{23} N_k \hat{v}_j \hat{v}_3 n_j dS$$

$$A_{4,2} = -\int_V \hat{\alpha}\hat{v}_3 N_l \frac{\partial(W_{23})}{\partial x_1}dV + \oint_\zeta W_{23} N_l \hat{\alpha}\hat{v}_3 n_1 dS$$

$$A_{2,3} = -\int_V \hat{\alpha}\hat{v}_3 N_l \frac{\partial(W_{23})}{\partial x_2}dV + \oint_\zeta W_{23} N_l \hat{\alpha}\hat{v}_3 n_2 dS$$

$$A_{2,4} = \int_V \frac{W_{23}}{\Delta t}\hat{\alpha} N_l\,dV - \int_V \hat{\alpha}\hat{v}_j N_l \frac{\partial(W_{23})}{\partial x_j}dV - \int_V \hat{\alpha}\hat{v}_3 N_l \frac{\partial(W_{23})}{\partial x_3}dV - \int_V W_{23}\hat{\alpha}\psi N_l dV + \oint_\zeta W_{23} N_l \hat{\alpha}\hat{v}_j n_j dS$$
$$+\oint_\zeta W_{23} N_l \hat{\alpha}\hat{v}_3 n_3 dS$$

The residuals on the right-hand-side are calculated for iteration level ‘n-1’ for time level ‘m’. The first term for each residual is a term that is calculated using time level ‘m-1’ and is frozen between time levels for all Newton iteration levels:

$$R_1 = \int_V \frac{W_1}{\Delta t}\alpha^{m-1}\,dV - \left[\int_V W_1 \frac{\hat{\alpha}}{\Delta t}dV - \int_V \hat{v}_j \hat{\alpha}\frac{\partial(W_1)}{\partial x_j}dV + \oint_\zeta W_1 \hat{\alpha}\hat{v}_j n_j dS\right]$$

$$R_2 = \int_V \frac{W_{21}}{\Delta t}(\alpha v_1)^{m-1}\,dV - \left[\int_V \frac{W_{21}}{\Delta t}\hat{\alpha}\hat{v}_1\,dV - \int_V \hat{\alpha}\hat{v}_j \hat{v}_1 \frac{\partial(W_{21})}{\partial x_j}dV + \oint_\zeta W_{21}\hat{\alpha}\hat{v}_j \hat{v}_1 n_j dS\right] + \int_V W_{21}\hat{\alpha}\left[\lambda_1 + \psi\left(v_{a,1} - \hat{v}_1\right)\right]dV$$

$$R_3 = \int_V \frac{W_{22}}{\Delta t}(\alpha v_2)^{m-1}\,dV - \left[\int_V \frac{W_{22}}{\Delta t}\hat{\alpha}\hat{v}_2\,dV - \int_V \hat{\alpha}\hat{v}_j \hat{v}_2 \frac{\partial(W_{22})}{\partial x_j}dV + \oint_\zeta W_{22}\hat{\alpha}\hat{v}_j \hat{v}_2 n_j dS\right] + \int_V W_{22}\hat{\alpha}\left[\lambda_2 + \psi\left(v_{a,2} - \hat{v}_2\right)\right]dV$$

$$R_4 = \int_V \frac{W_{23}}{\Delta t}(\alpha v_3)^{m-1}\,dV - \left[\int_V \frac{W_{23}}{\Delta t}\hat{\alpha}\hat{v}_3\,dV - \int_V \hat{\alpha}\hat{v}_j \hat{v}_3 \frac{\partial(W_{23})}{\partial x_j}dV + \oint_\zeta W_{23}\hat{\alpha}\hat{v}_j \hat{v}_3 n_j dS\right] + \int_V W_{23}\hat{\alpha}\left[\lambda_3 + \psi\left(v_{a,3} - \hat{v}_3\right)\right]dV$$

A complete solution to the problem requires that a system of equations be constructed for each element in the domain Ω, where the assembly into a global matrix results in a system of algebraic equations to be solved. The summation of contour integrals dS in the global matrix formulation reduces to zero for interior elements. Therefore such integrals only need to be considered when evaluating boundary elements. The weight functions W are represented by the standard shape functions N used in the Galerkin formulation. In addition to this, the formulation is complemented by Streamlined Upwind (SU) terms to help alleviate artificial diffusion associated with many classical upwind methods [63, 64].

II. ICE3D Numerical Solution for Different Icing Zones

The governing equations for mass and energy applied to a thin water-film are

$$\rho_w \left[\frac{\partial h_f}{\partial t} + \vec{\nabla} \cdot \left(\frac{h_f^2}{2\mu_f} \vec{\tau}_{wall}(\vec{x}) \right) \right] = S_M$$

$$\rho_w c_{p,w} \left[\frac{\partial h_f \tilde{T}}{\partial t} + \vec{\nabla} \cdot \left(\frac{h_f}{2\mu_f} \vec{\tau}_{wall}(\vec{x}) \left\{ h_f \tilde{T} \right\} \right) \right] = S_E \qquad \textbf{Eq. II-1}$$

Where h_f is the film height, $\tilde{T}$ is the surface temperature, $\vec{\tau}_{wall}$ is the wall shear stress taken from the airflow solution from FENSAP, μ_f is the film viscosity, ρ_w and $c_{p,w}$ are the density and specific heat capacity of water respectively. The source terms for mass S_M and energy S_E are given as

$$S_M = U_\infty LWC_\infty \beta_1(\vec{x},t) + \alpha_{st}\alpha_m U_\infty ICC_\infty \beta_2(\vec{x},t) - m''_{evap}(\vec{x},t) - m''_{ice}(\vec{x},t)$$

$$S_E = U_\infty LWC_\infty \beta_1 \left[c_{p,w}\left(T_{\infty,d} - \tilde{T}\right) + \frac{\left\|\vec{v}_d\right\|^2}{2} \right] - 0.5 m''_{evap}\left(L_{evap} + L_{sub}\right) + \sigma\varepsilon\left(T_\infty^4 - T^4\right) +$$

$$\alpha_{st}\alpha_m U_\infty ICC_\infty \beta_2 \left[c_{p,w} T_{\infty,ic} + \frac{\left\|\vec{v}_{ic}\right\|^2}{2} - L_{fus} \right] + m''_{ice}\left(L_{fus} - c_{p,ice}\tilde{T}\right) - c_h(\tilde{T} - \tilde{T}_{adiabatic}) + q''_{los} \qquad \textbf{Eq. II-2}$$

Where U_∞ is the free-stream particle velocity, LWC_∞ and ICC_∞ are the free-stream liquid water content and ice crystal content, β_1 and β_2 are the collection efficiency for droplets and crystals respectively. Other terms are specified in *List of Symbols* preface. Explicit discretization in time and spatial discretization using a control volume analysis based on Roe's scheme yields the following form

$$\left(\rho_w \frac{\phi_{1,i}^{n+1} - \phi_{1,i}^n}{\Delta t} + m''^{n+1}_{ice} - \tilde{S}_{m,i}^n \right) V_i + \sum_j^{NE} \oint \rho_w \phi_{ROE,1,ij}^n \, dS = 0$$

$$\left(\rho_w c_{p,w} \frac{\phi_{2,i}^{n+1} - \phi_{2,i}^n}{\Delta t} - m''^{n+1}_{ice}\left(L_{fus} - c_{p,ice}\tilde{T}^{n+1}\right) - \tilde{S}_{E,i}^n \right) V_i + \sum_j^{NE} \oint \rho_w c_{p,w} \phi_{ROE,2,ij}^n \, dS = 0 \qquad \textbf{Eq. II-3}$$

Where ϕ_1 is the film height h_f, and ϕ_2 is the product of film height and surface temperature $h_f\tilde{T}$. $\tilde{S}_{m,i}, \tilde{S}_{E,i}$ are the source terms in Eq. II-2 minus the terms containing the ice accretion rate m''_{ice}, which is an additional unknown that must be solved for along with the film height h_f and equilibrium surface temperature $\tilde{T}$. The roe fluxes for each edge 'j' connected to control volume node 'i' can be computed as

$$\phi_{ROE,1,ij} = \frac{1}{2}\left(\frac{\vec{\tau}_{wall} \bullet \vec{n}}{2\mu_f}\right)_{ij} \left[\left(\phi_{1,i}^2 + \phi_{1,j}^2\right) - \left(\phi_{1,i} + \phi_{1,j}\right)\left(\phi_{1,j} - \phi_{1,i}\right)\right]$$

$$\phi_{ROE,2,ij} = \frac{1}{2}\left(\frac{\vec{\tau}_{wall} \bullet \vec{n}}{2\mu_f}\right)_{ij} \left[\left(\phi_{1,i}\phi_{2,i} + \phi_{1,j}\phi_{2,j}\right) - \frac{1}{4}(\phi_{2,i} + \phi_{2,j})\left(\phi_{1,j} - \phi_{1,i}\right) - \frac{1}{4}(\phi_{1,i} + \phi_{1,j})\left(\phi_{2,j} - \phi_{2,i}\right)\right] \quad \textbf{Eq. II-4}$$

A unique solution at any given point in time and space depends on satisfying the compatibility relations to a solution defined in one of three icing zones – rime, glaze or water-film.

II.A Region 1: Liquid Film Only

This region corresponds to one containing only a film and no ice growth. The mass of ice m''_{ice}, is assumed zero at the current time level and the mass and energy equations are re-cast to yield the film height and equilibrium surface temperature as follows

$$h_{fi}^{n+1} = \phi_{1,i}^{n+1} = \phi_{1,i}^{n} + \Delta t \left[\frac{\tilde{S}_{m,i}}{\rho_w} - \frac{\sum_j^{NE} \oint \phi_{ROE,1,ij}^{n}\, dS}{V_i}\right]$$

$$\tilde{T}_i^{n+1} = \frac{\phi_{2,i}^{n+1}}{\phi_{1,i}^{n+1}} = \frac{1}{\phi_{1,i}^{n+1}} \left[\phi_{2,i}^{n} + \Delta t \left[\frac{\tilde{S}_{E,i}}{\rho_w c_{p,w}} - \frac{\sum_j^{NE} \oint \phi_{ROE,2,ij}^{n}\, dS}{V_i}\right]\right] \quad \textbf{Eq. II-5}$$

$h_f \geq 0$ and $h_f\tilde{T} \geq 0$ yield a physically meaningful solution in this region.

II.B Region 2: Glaze/Clear Ice

This region corresponds to one containing both water-film and ice. The temperature $\tilde{T}$ is assumed to be zero Celsius at the current time level and the mass of ice and film height can be obtained as follows

$$m_{ice}''^{n+1} = -\frac{1}{L_{fus}}\left(\rho_w c_{p,w}\frac{\phi_{2,i}^n}{\Delta t} + \tilde{S}_{E,i}^n - \frac{\sum_j^{NE}\oint \rho_w c_{p,w}\phi_{ROE,2,ij}^n\, dS}{V_i}\right)$$

$$h_{fi}^{n+1} = \phi_{1,i}^{n+1} = \phi_{1,i}^n + \Delta t\left(\frac{\tilde{S}_{E,i}^n - m_{ice}''^{n+1}}{\rho_w} - \frac{\sum_j^{NE}\oint \rho_w \phi_{ROE,1,ij}^n\, dS}{V_i}\right) \quad \text{Eq. II-6}$$

$m_{ice}'' \geq 0$ and $h_f \geq 0$ yield a physically meaningful solution in this region.

II.C Region 3: Rime Ice

This region corresponds to one containing only ice. The film height h_f is assumed zero at the current time level and the mass of ice and surface equilibrium temperature are obtained as follows

$$m_{ice}''^{n+1} = \tilde{S}_{m,i} + \rho_w \frac{\phi_{1,i}^n}{\Delta t} - \frac{\sum_j^{NE}\oint \rho_w \phi_{ROE,1,ij}^n\, dS}{V_i}$$

$$\tilde{T}_i^{n+1} = \frac{\left(\rho_w c_{p,w}\frac{\phi_{2,i}^n}{\Delta t} + \widehat{S}_{E,i} - \frac{\sum_j^{NE}\oint \rho_w c_{p,w}\phi_{ROE,2,ij}^n\, dS}{V_i}\right)}{U_\infty LWC_\infty \beta_1 c_{p,w} + c_h + m_{ice}''^{n+1} c_{p,ice}} \quad \text{Eq. II-7}$$

$$\widehat{S}_{E,i} = U_\infty LWC_\infty \beta_1\left[c_{p,w}\left(T_{\infty,d}\right) + \frac{\left\|\vec{v}_d\right\|^2}{2}\right] - 0.5 m_{evap}''\left(L_{evap} + L_{sub}\right) + \sigma\varepsilon\left(T_\infty^4 - T^4\right) +$$

$$\alpha_{st}\alpha_m U_\infty ICC_\infty \beta_2\left[c_{p,i}T_{\infty,ic} + \frac{\left\|\vec{v}_{ic}\right\|^2}{2} - L_{fus}\right] + m_{ice}''\left(L_{fus}\right) + c_h(\tilde{T}_{adiabatic}) + q_{loss}''$$

$m_{ice}'' \geq 0$ and $m_{ice}''\tilde{T} < 0$ ensure a physically meaningful solution in this region.